HAPTIC FEEDBACK SYSTEM DESIGN
FOR MR-GUIDED NEEDLE INTERVENTION

A DISSERTATION
SUBMITTED TO THE DEPARTMENT OF MECHANICAL ENGINEERING
AND THE COMMITTEE ON GRADUATE STUDIES
OF STANFORD UNIVERSITY
IN PARTIAL FULFILLMENT OF THE REQUIREMENTS
FOR THE DEGREE OF
DOCTOR OF PHILOSOPHY

Jung Hwa Bae
June 2018

Abstract

Advances in imaging are leading to new opportunities for medical diagnosis and treatment, including the possibility to perform procedures such as biopsies while a patient is undergoing imaging. Along with these new opportunities come new challenges. In particular, for patients undergoing magnetic resonance (MR) imaging, the geometry of the MR machine makes it difficult to perform procedures. One solution is to provide robotic or teleoperated equipment that can fit in the remaining space between a patient and the inner walls of the MR bore and manipulate tools such as biopsy needles. A physician stands near the MR machine, viewing live images and controlling the robotic equipment within. However, in this scenario the physician lacks the tactile sensitivity that she would have if manipulating a needle with her own hands.

This thesis presents technology to provide haptic feedback to a physician operating a master device that controls a robotic system for MR-guided procedures. The first part of the solution is a new biopsy needle instrumented with optical fibers with Bragg gratings. The needle is equipped with features to enhance its sensitivity to forces applied at the tip of the needle. The optical fibers are unaffected by the intense MR field, and the needle produces no imaging artifacts beyond those of a standard biopsy needle.

The second part of the thesis introduces two different types of haptic displays that present the radial and axial forces, respectively, from the instrumented needle. The radial forces provide guidance to users attempting to target small, compliantly-supported objects (e.g. tumors) in tissue. The axial forces provide users with the ability to detect when the tip of the needle has contacted bone or punctured a membrane. In both cases, the displays use materials and actuators that are MR-compatible. Controlled experiments confirm that human subjects can use the information provided by the displays to improve targeting accuracy and to detect membrane contact. An additional experiment shows that force information provided by the needle can reveal changes in tissue texture, for example, when passing through healthy or fibrotic liver tissue.

Acknowledgments

On the journey to becoming a Ph.D., I have been lucky to meet, learn, and work with great people, and I want to show my appreciation for them. First, I want to thank Mark and Bruce for their guidance and support. They have encouraged me to explore freely what I am interested in and want to pursue. Also, I learned from them how important it is to understand the overall objective of the project as well as the work details. Besides this, Mark has always coached me on how I could present my work better to my audience/readers. Bruce gave me ideas for the project and also the opportunity to talk, learn, and work with doctors during my graduate career. I also want to express my appreciation to Allison, Paul, and Gary for being on my defense committee. Thanks to Allison's advice, lectures, and talks, I learned many exciting topics about medical robotics and haptics. I appreciate Paul as well, who listened to and answered my questions about my career and graduate life. I enjoyed his demos, lectures, and office hours as a student and a teaching assistant. I also want to thank professor Glover for being my defense committee chair and giving tremendous help on testing the MR-compatibility of the haptic device.

I am grateful to work with kind and smart fellow graduate students. Chris is a paper crew, an English teacher, and a great friend. He has the kindness needed to help others, knowledge, and passion for his work. I enjoyed working with him and am glad to have him as a collaborator and friend. Inrak has been a very supportive and joyful colleague and friend. He was the first person on many of my pilot user studies and always gave very valuable feedback. I also want to thank Daniel for his help on the preliminary test and Michael and Alexa for helping me review the video recordings of the first user study on the lateral force feedback. Xiyang and Dave gave me excellent advice to solve electromechanical problems I encountered in the process of building a haptic feedback system. Santhi mentored me to learn shape-sensing needles and force-sensing needles. I have also been happy to work with all the BDML and my other colleagues: Matt, Sung Jun, Alice, Hannah, Hao, Shiquan,

Amy, Zhan Fan, Natalie, Arul, Sam, Lawrence, and Mathieu.

I want to credit June Lee, who is my best friend and soul sister. She has been very supportive and has taken care of me like her younger sister.

Lastly, I appreciate my family. My mother, Hyang Jin Kim, and my father, Jong Doo Bae, have always believed in, prayed for, and supported me. Despite a time and location difference, they called me on the phone and sent me texts to cheer me. Thanks to my sister, Joo Hyung Bae, who took care of family events, I could study at Stanford with no worries. I thank my husband, Alex Kwon, for being my soulmate, love, and best friend. I am happy that I will be with you for the rest of my life, and I am excited for our next journey.

Contents

List of Tables

List of Figures

xiii

Chapter 1

Introduction

Imaging machines have opened up a new era of patient treatment. They allow doctors to detect disease at an early stage through a screening exam and to locate the abnormal tissue to plan an effective surgery or treatment. Precise location of abnormal tissue can increase the success rate for procedures and shorten the overall procedure time. Ultrasound, computed tomography (CT), X-ray, and magnetic resonance imaging (MRI) are all examples of medical imaging modalities that can be used to obtain a view inside the body. Each of these has certain advantages and limitations, which may determine when and how it is used. For example, doctors use CT and X-ray imaging to examine the skeleton, and for chest or intra-abdominal diseases since these often do not require high soft tissue contrast. Ultrasound imaging and MR-Imaging are better for locating soft tissue diseases, so they are more frequently selected when doctors want to focus on soft tissue abnormalities. Increasingly, these imaging modalities are not only used for diagnosis or pre-planning but also to provide intra-operative guidance during minimally invasive interventions. Compared to a pre-planned surgery or intervention, imaging-guided interventions provide more feedback for precisely locating medical tools with respect to target tissue during the procedure.

Among the least expensive, fastest and most widely used imaging modalities is ultrasound. However, it can be relatively difficult to track the position and orientation of a small tool, such as a biopsy needle, using ultrasound [9,10]. Several methods have been suggested to overcome this difficulty. For example, electromagnetic position sensors [10], fiber-optic hydrophones [9], and tool vibration and doppler techology [11] have been integrated to the ultrasound system for better tool position detection.

Although the aforementioned additions can improve the ability to track a tool with

ultrasound, MR imaging still offers a more complete three dimensional view of tool position and orientation in soft tissue. In addition, various MR imaging sequences are employed to detect the geometry and location of abnormal tissues accurately – for example, when the target is located behind bone, as in case of the liver or lungs. MRI also provides a comparatively accurate and clear image of prostate cancer when CaP values are high [12]. Accurate shape and location recognition of the target is essential in this application because it can prevent insufficient removal of diseased tissue and minimize excessive removal of healthy tissue during the procedure.

The advantages of MR-Imaging have lead to the development of several MR-guided interventions including brachytherapy, cryotherapy, needle biopsy and HIFU (high intensity focused ultrasound). As listed here, most of the MR-guided interventions use a biopsy needle to perform the procedure. However, manipulating the biopsy needle under MR-guidance is challenging due to the long and narrow MR bore where the patient is located for scanning. For a typical machine, the diameter of the bore is 60 cm to 70 cm. Furthermore, the distance from the iso-center to the opening of the bore makes it hard to reach the patient. The small size of the bore can affect not only doctors but patients as well, particularly for patients who are large or prone to claustrophobia.

Open-MRI machines were developed to resolve these issues, but the image qualities (signal to noise, contrast) are comparatively low. The highest magnetic field is just 1.2T for an open MRI machine for clinical usage, as compared to up to 7T for the closed-bore MRI machines. The lower magnetic field strength results in poorer image quality for all imaging sequences [13]. Also, the time-varying gradient magnetic fields used for spatial encoding are much slower and weaker on open-MRI system. Moreover, even open scanners don't enable as much access as desired for many procedures. Thus there remains a motivation to find solutions for image-guided procedures in closed-bore machines.

The geometric constraint imposed by closed MR machines motivates a new approach in which a physician can stand outside of the MR machine while directing procedures within. This scenario requires several new elements of technology: a robotic or teleoperated system to perform the procedure inside the bore, sensing at the tool tip to detect forces (and perhaps other quantities like temperature) at the site of operation, and a visual and haptic display to render the remotely sensed quantities to the physician. In each case, the MR imaging environment imposes constraints due to the intense magnetic field present.
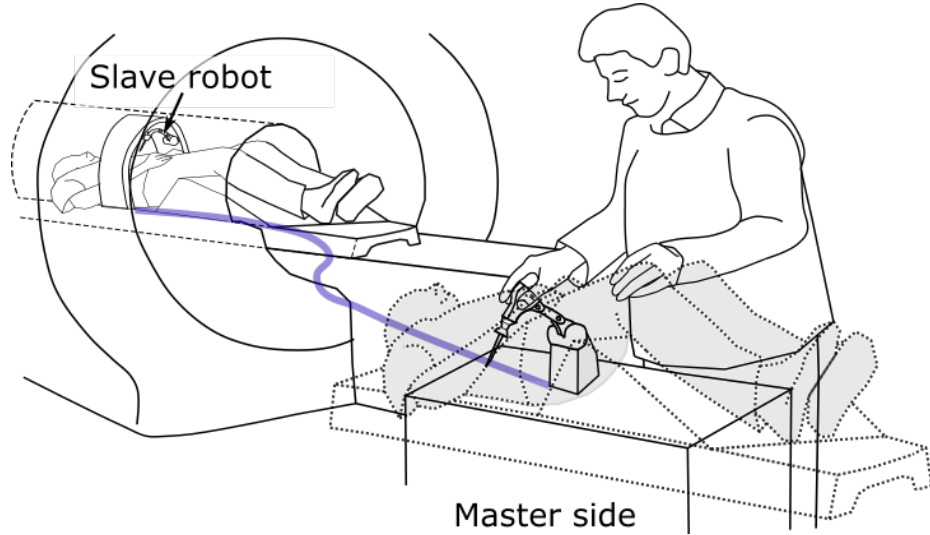
Figure 1.1: Sketch showing an example of a teleoperation system for MR-guided interventions.

An MR-compatible robotic system locates a compact slave robot inside the bore, manipulating the medical tool, while the doctor is remotely controlling the master side nearby. The goal is to offer accessibility, ergonomics and sufficient precision for procedures. However, without a force sensor that can detect tool-tissue interaction events, a robotic system partially isolates the physician from the physical experience of operating on a patient. This thesis introduces an MR-compatible haptic feedback system (a force sensing tool combined with haptic displays). The displays are small and low-power, affecting only the physician's fingertips. Therefore they can be added to an existing robotic or teleoperated system without substantially affecting that system's dynamics or control.

Haptic feedback systems can display radial and axial force measurements from an instrumented biopsy needle. Radial forces produce bending as the needle is manipulated through various tissues. Rapid changes in axial forces occur when pushing the needle into membranes or bone. Display of the radial forces can provide the physician with a sense of how the needle is bending caused by tissue (stiffness or heterogeneity of tissue) and whether the tip of the needle is contacting a small target on- or off-center. The axial force provides an indication of tissue properties (e.g. stiffness, friction, roughness) and indicates when the tip of the needle encounters a discrete change in tissue. The hypothesis behind this work is that informing a physician in real-time about needle-tissue interactions may lead to higher

success rates for procedures that require precise sampling or delivery of a treatment substance. Furthermore, knowledge of some tissue properties, such as texture (roughness), can expedite diagnosis due to the difference between healthy and diseased tissue (e.g. fibrotic liver).

1.1   Contributions

The work in this thesis aims to advance the technology needed for robot-assisted interventions performed under MR imaging:

- Developed a new optical tip-force sensing needle with improved axial sensitivity in comparison to previous designs for teleoperated needle interventions under MR guidance.

- Demonstrated through human subjects experiments that access to sensed forces at the tip of a needle provides more accurate detection of events such as membrane puncture than access to forces at the base of a needle.

- Developed a skin deformation lateral force display for MR-guided needle intervention.

- Demonstrated through human subjects experiments that guidance, based on the display of lateral forces, reduces failures in targeting and reduces confusion concerning the relative location of a needle with respect to a target.

- Developed a MR-compatible cutaneous haptic display using electroactive polymer (EAP) actuators.

- Demonstrated through human subjects experiments that the EAP haptic display is suitable for relaying information about changes in axial force that accompany events such as contacting and puncturing a membrane.

- Demonstrated a texture sensing application for the force sensing needle in liver tissue.

1.2   Dissertation Overview

The remaining chapters of this thesis present the sensing and display technologies developed to support MR-guided procedures. Chapter 2 summarizes the related work on which this thesis builds directly.

Chapter 3, describes the design and calibration of an MR-comaptible force sensing needle with features to enhance axial force sensitivity in comparison to previously developed needles with embedded optical fibers. Material in this chapter draws on :

- ©2013 IEEE. Reprinted with permission, from Elayaperumal, Santhi, et al. "MR-compatible biopsy needle with enhanced tip force sensing." IEEE World Haptics Conference (WHC), 2013, pp. 109-114. 2013. doi:10.1109/WHC.2013.6548393 [14].

- ©2014 IEEE. Reprinted with permission, from Elayaperumal, Santhi et al. "Detection of membrane puncture with haptic feedback using a tip-force sensing needle." IEEE/RSJ International Conference on Intelligent Robots and Systems (IROS), pp. 3975-3981. 2014. doi: 10.1109/IROS.2014.6943121 [15]

Chapter 4 presents an approach for displaying radial force information from the needle of Chapter 3 in a haptic display to improve the performance of subjects in a targeting task. The chapter presents the design of a 2 degree of freedom skin deformation haptic device, including provisions made to accommodate the characteristics of ultrasonic motors (piezomotors) that drive the device. The chapter includes a user study to evaluate the functionality of the haptic device and the effectiveness of haptic feedback during a needle procedure. The contents are based on:

- ©2016 IEEE. Reprinted with permission, from Bae, Jung Hwa, et al. "Display of needle tip contact forces for steering guidance." IEEE Haptics Symposium (HAPTICS), pp. 332-337. 2016. doi: 10.1109/HAPTICS.2016.7463199 [16].

In addition to radial forces, axial forces can provide useful information. Chapter 5 presents the results of experiments first with a conventional voice coil actuator (which is not MR compatible) and then with a new haptic device based on electroactive polymers. User tests confirm that subjects can detect changes in axial force associated with events such as contacting or puncturing a membrane in tissue. The chapter draws upon publications [15, 17, 18]:

- ©2014 IEEE. Reprinted with permission, from Elayaperumal, Santhi et al. "Detection of membrane puncture with haptic feedback using a tip-force sensing needle." IEEE/RSJ International Conference on Intelligent Robots and Systems (IROS), pp. 3975-3981. 2014. doi: 10.1109/IROS.2014.6943121 [15]

- ©2017 IEEE. Reprinted with permission, from Bae, Jung Hwa*, Han, Amy Kyung-won*, et al. "Haptic feedback of membrane puncture with an MR-compatible instrumented needle and electroactive polymer display." IEEE World Haptics Conference (WHC), pp. 54-59. 2017. doi: 10.1109/WHC.2017.7989876 (*equally contributed) [17]

- ©2018 IEEE. Reprinted with permission, from Han, Amy Kyungwon*, Bae, Jung Hwa*, et al. MR-Compatible Haptic Display of Membrane Puncture in Robot-Assisted Needle Procedures, accepted to IEEE Transactions on Haptics. (*equally contributed) [18]

Chapter 6 presents experiments involving tissue texture detection for healthy versus fibrotic liver tissue with the force-sensing needle. More frequent force changes (characterized by spikes in the processed data) were associated with the excessive extracellular matrix in fibrotic liver. The average interval between these force changes was used to estimate the tissue roughness or granularity.

Chapter 7 concludes the thesis by summarizing how the force sensing needle and cutaneous haptic feedback based on radial and axial needle forces can potentially improve the speed and accuracy of MR-guided interventions and suggests future work to extend the contributions of this thesis.

Chapter 2

Background and Related Work

This chapter provides an overview of the main areas of work on which this thesis builds. Additional citations are provided in context as they occur in later chapters.

As discussed in the previous chapter, the geometry of the closed-bore MR machine poses a challenge for performing procedures while a patient is undergoing MR imaging. Several groups of investigators have proposed robotic or teleoperated systems to overcome this challenge, allowing a physician to stand outside the MR machine and conduct procedures within [19–27]. In addition, a number of works specifically recognize the value of haptic feedback for such a system. However many of these lack a haptic feedback system or employ materials or technologies (e.g. electromagnetic motors) that are not MR-compatible at the master side. This forces the physician to stand outside of the immediate MR machine room, which may hinder fast response if the patient's condition changes. Others (e.g. [20, 23, 24]) are MR-compatible, but restricted to a specific procedure such as transperineal biopsy. In the following sections we review work related to the problem of sensing tool/tissue interactions and displaying haptic stimuli, considering particularly those approaches which are at least potentially MR-compatible.

2.1 Instrumented Needle for Force Sensing

Along with the rise of teleoperated or human-guided robotic systems in medical applications, the development of force sensing tools has received increasing attention. For example, several groups have developed force sensing medical tools for teleoperated laparoscopy. In one approach, laparoscopic forceps are instrumented with various types of sensors such as

7

capacitive force sensors [28], piezoelectric sensors [29], or optical sensors [30, 31]. These sensing tools inform user of tissue stiffness, a grip force of the forceps, a suture tyeing force and other valuable tool-tissue interaction forces.

Although instrumented laparoscopic tools provide useful design insights, the majority of MR guided interventions use needles with very small diameters (often 1 mm or less) [32], which imposes additional constraints on the sensing technology. Su et al. built a 3-axis force sensor that can measure the force at the base of a needle based on an optical micrometry technology [1]. A flexure, a spherical mirror, and optical fibers were utilized to detect the light intensity changes arising from the force on the needle. When force deforms the flexure, which is rigidly connected to the base of the needle, the movement of the spherical mirror changes the intensity of reflected light. For example, when an axial force exerted on the needle compresses the flexure, the reflected light intensity increases with the reduction in distance between the mirror and photo-detecting optical fibers. Similarly, a radial force on the needle bends the flexure and changes the reflected light intensity pattern (Figure 2.1A).

Another approach is to instrument the base of a needle with strain gage force sensors in a coaxial force-sensing approach to measure separately the axial forces on a needle and inner stylet force [33]. The corresponding forces can be relayed to a human operator for improved sensitivity during needle insertion.

In an alternative approach, a Fabry-Pérot interferometer was incorporated into an axial force sensor for MR-guided needle interventions [34]. The interferometer has a gap between two segments of fiber. Each segment end has a semi-reflective mirror creating a fringe pattern which is used to measure the strain of the fiber. Depending on the force applied to the fiber, the size of the gap changes, causing a difference in intensity of the fringe. The reported sensitivity of the sensor is 40 mV/µstrain.

Optical fibers with Fiber Bragg Grating (FBG) sensors can also be embedded into tools to measure bending strains. Iordachita et al. [35] and Gijbels et al. [2] designed a very thin force-sensing tool for retinal microsurgery by embedding FBG sensors. The FBG sensor is a type of optical strain gage. It is very sensitive to the mechanical strain (it can detect as little as 1µstrain) and very compact, with optical fibers having a minimum diameter of 80μm. Each of these tools have 3 FBG sensors to read two orthogonal radial forces as the tool is peeling layers of retina or piercing a retinal vein for delivering an anti-coagulant.

Park et al. [3] and Henken et al. [36] designed biopsy needles with FBG sensors. The design by Park et al. has two triplets of FBG sensors to measure bending strains at two

locations while also compensating for variations in temperature. The measured bending strains are proportional to the curvature at the corresponding locations along the needle. From these, one can estimate of the overall needle profile by integrating twice, using the moment curvature equation from beam theory. Estimating the needle profile from a small set of discrete sensor locations invariably introduces some error when integrating from the base to the tip of the needle. Nonetheless, tip accuracies within one or two millimeters are possible. Henken et al. increased the number of FBG sensor locations to five and demonstrated the capability of the needle shape sensing for distributed loads. They also proposed an uni-axial force sensing needle. A FBG sensor is glued to the inner surface of a polyvinyl chloride (PVC) jacket and this jacket is attached to the inner surface of a tube (outer diameter 1.0 mm). There is a PVC ring which allows a small displacement of the needle tip when an axial force is applied. The displacement produces strain on the PVC jacket, which is measured by the optical sensor.

2.2 Haptic Feedback for Teleoperation Systems

Tactile feedback and dexterous tool manipulation are inseparable. Humans are remarkably adept at determining the important properties of an object (e.g. stiffness, texture, weight) for object manipulation from the tactile cues they obtain while manipulating [37, 38]. This observation also applies to medical tool manipulation, and is a driving motivation for displaying tactile information in teleoperated procedures.

There are several options for displaying haptic information to users. As a starting point, we can consider both kinesthetic and cutaneous information. It is also possible to display kinesthetic information through a tactile device and vice versa. Furthermore, there are other possible methods that relay the haptic information through alternative sensory channels such as visual or auditory feedback. For example, the force applied on a suture during knot tying can be displayed as a circle of changing color, or a palpation force can be represented as a bar graph at the side of a stereoscopy screen [39, 40]. Warning sounds can also inform users that a force level is rising [41].

Each of these approaches has advantages and disadvantages. For instance, a visual-force display does not require an additional device as long as if there is a screen for image display; however the visual channel is already occupied by tracking the locations of tools and targets. In addition, subjects respond more slowly to visual cues than they do to direct
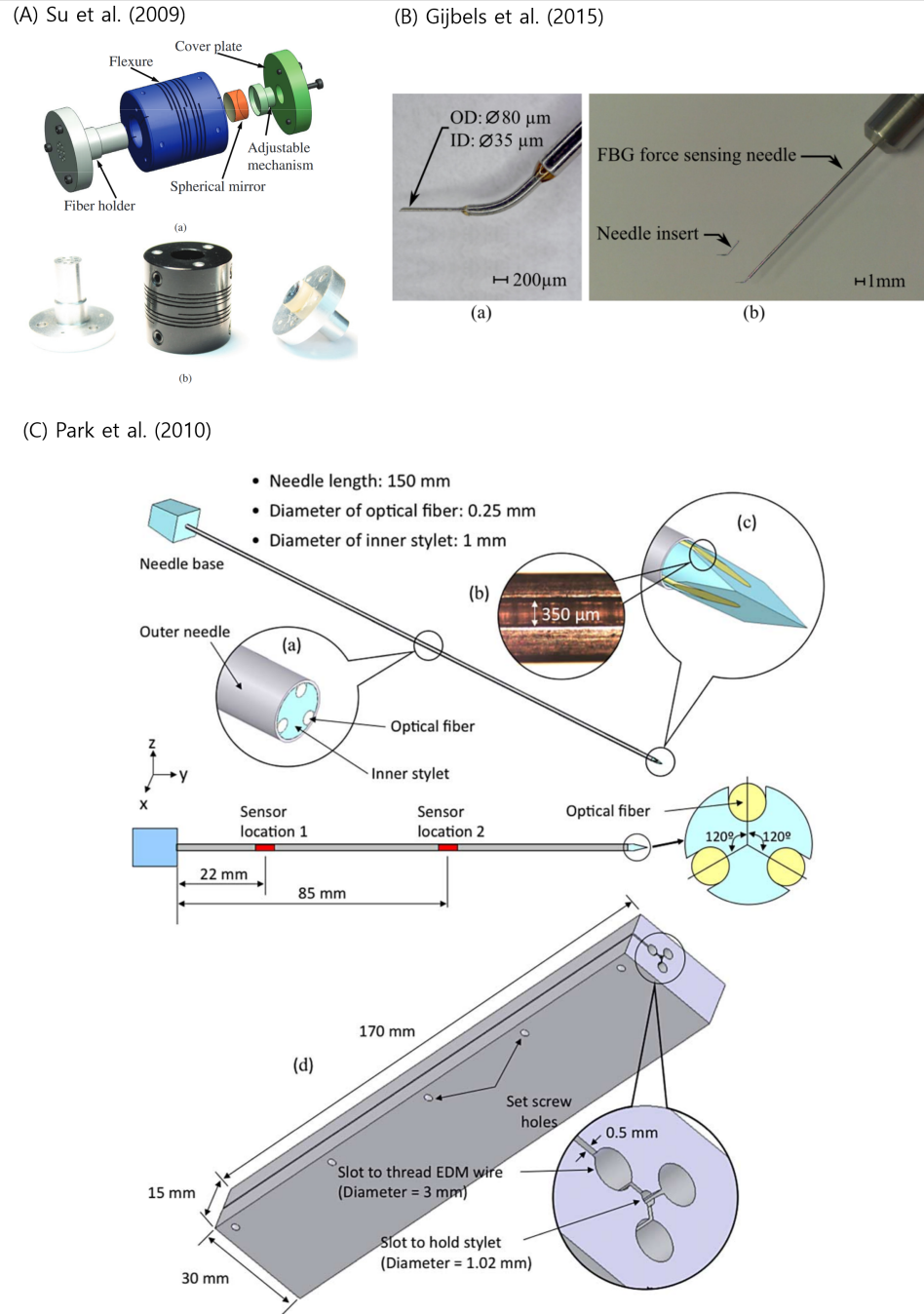
Figure 2.1: Designs of FBG based force sensing tools. Figures are reprinted from (A)©2009 IEEE [1] (B)©2015 IEEE [2] (C)©2010 IEEE [3]

haptic signals relating to the strength of a grasp [42].

Displaying audio cues is also relatively simple but audio cues can be masked by the substantial noise produced by an MR machine. Again, using a haptic display may avoid overloading an already occupied sensory channel.

Haptic display devices can deliver forces or cutaneous signals to users. Of these, the latter typically require less power, with small motions and moderate forces. Hence they have less possibility to disturb the operation of a teleoperated system.

2.3   Skin Deformation Haptic Devices

As noted, haptic feedback includes kinesthetic and tactile information. In human skin, mechanoreceptors respond to various types of tactile stimuli including texture, stiffness, slip, and temperature of objects that we handle. Kinesthetic information is perceived by mechanoreceptors in muscles, tendons, and joints [43] and tells us how the interaction with an object affects motion. For example, pushing or lifting an object provides kinesthetic force information. A very realistic haptic feedback system might combine cutaneous and kinesthetic information. However, for the manipulation of small tools such as needles, cutaneous feedback is particularly important [38, 44] which argues for a focus on cutaneous haptic display.

There are four main types of cutaneous mechanoreceptors. Each of these has different receptive fields (type I and II) and different frequency responses (fast adapting, slow adapting). During tool manipulation, fast adapting receptors (FA I and FA II) detect the first and last moments of contact, and events such as the onset of slip. Contact events often produce vibrations which Pacinian corpuscles, in particular, respond to. However tactile perception is mostly insensitive to the direction of vibration. In other words, only the frequency and magnitude of vibration are perceived. In contrast, slow adapting mechanoreceptors can give magnitude, temporal, and directional information concerning the low frequency forces transmitted through an object during manipulation [45].

Skin deformation type haptic devices activate both slow and fast adapting mechanoreceptors to deliver magnitude, direction and temporal information associated with a changing force. For display, a skin deformation haptic device has a moving part, called a tactor, that produces deformations where it contacts the skin. The deformation pattern can be rotational or linear.

In early work, Bark et al. [46] established that subjects can achieve a linear mapping between the displayed magnitude and direction of skin stretch in response to the controlled motion of a limb or joint, such as bending or rotating a wrist. Subsequent work [4, 47, 48] established that skin stretch can be effective for tracking the magnitude and direction of forces applied to an object and for applications such as navigation.

The perception of skin stretch displacement is affected by the moving speed of the tactor. Gleeson et al. [4] reported that the minimum perceivable displacement reduces as the display speed increases. Figure 2.2 shows how the minimum perceivable displacement changes with display speed.

Since a tactor can move to any displacement position within a designated range, it can display any force magnitude that is mapped to the displacement. A model consisting of a spring, which represents the stiffness of subject's skin, provides an estimate of the displayed force [49]. Successful direction perception of the skin stretch was demonstrated in human subject studies [50].

With the ability to display both magnitude and direction information, skin stretch has been adopted for applications including navigation and virtual reality gaming [48, 51] Focusing on medical applications, Especially for the medical procedure, Schorr et al. [52] demonstrated that the tool-tissue interaction forces associated with tissue stiffness during palpation can be relayed effectively to the user through a skin stretch apparatus.

		Speed (mm/sec)			
		0.5	1	2	4
Displacement (mm)	1	0.98 ±0.024	0.99 ±0.011	1.00 ±0.000	1.00 ±0.009
	0.5	0.95 ±0.024	0.98 ±0.013	0.99 ±0.010	0.99 ±0.009
	0.2	0.85 ±0.067	0.94 ±0.050	0.96 ±0.025	0.95 ±0.027
	0.1	0.69 ±0.083	0.85 ±0.061	0.90 ±0.027	0.89 ±0.027
	0.05	0.54 ±0.086	0.72 ±0.069	0.73 ±0.061	0.79 ±0.046

Figure 2.2: A table showing the displacement of a tactor and the corresponding perception success rate, which depends on the display speed. Reprinted from ©2010 IEEE [4].

2.4   Haptic Feedback for Needle Procedures

When a needle is inserted into tissue, it often bends and deviates from the desired path. For example, the shape of the needle tip, as in the case of a bevel tip, may introduce an asymmetric tip force that produces deflection. In addition, inhomogeneity of tissue or substructures such as membranes can cause unbalanced radial forces, bending the needle. Therefore, the path of needle should be consistently corrected by steering the needle as it is inserted. At the end of an intervention, a poor needle steering performance can increase tissue damage due to multiple insertions [53, 54]. In addition, it lengthens the procedure time, which increases costs. In order to improve the needle steering performance, haptic steering guidance has been suggested.

Basu et al. [5] designed a haptic sleeve that guides a novice user to drive a needle properly to reach a target. The sleeve has multiple vibrotactile motors that stimulate different parts of a user's arm and hand (Figure 2.3). The authors compared different guidance strategies, telling a user to adjust the needle orientation for insertion in terms of a coordinate frame embedded in the tool (tool space), in terms of the tip location in a world reference frame, and in terms of the users' elbow and wrist angles (joint space). The results indicated that the tool space guidance was significantly better in terms of reducing directional errors and in terms of user preference (easiest to understand).

(a) Tool Space Insertion   (b) Cartesian Space Insertion   (c) Joint Space Insertion

(d) Tool Space Rotation and Insertion   (e) Cartesian Space Lateral Motion   (f) Wrist Rotation (Tool/Joint Space)
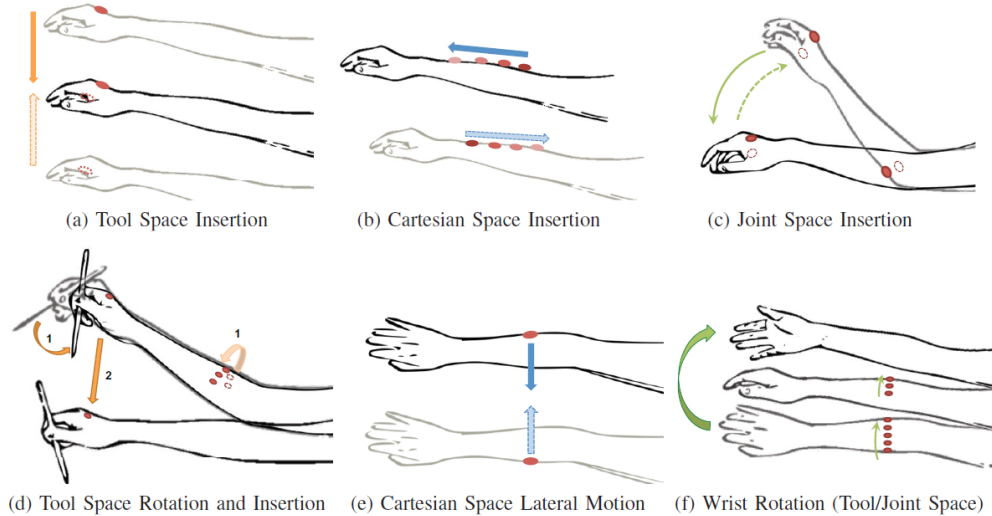
Figure 2.3: Vibrotactile motors were attached to a user's wrist for three different guidance strategies. Reprinted from ©2016 IEEE [5].

Rossa et al. [6] designed a wrist band, shown in Figure 2.4, that gives steering guidance by changing the vibration pattern of motors embedded inside of a wrist band. The authors categorized needle steering maneuvers required to reach a target and made a vibration pattern associated with each maneuver. Four categories of maneuver were: needle insertion velocity, needle rotation, pushing the needle up/down, stopping the needle at the target, and withdrawing. The training and learning effects were observed to determine how well users can perform the corresponding maneuver by recognizing the associated pattern and positioning needle tip as desired. To use these vibration patterns, users had to be trained several times before a needle procedure.
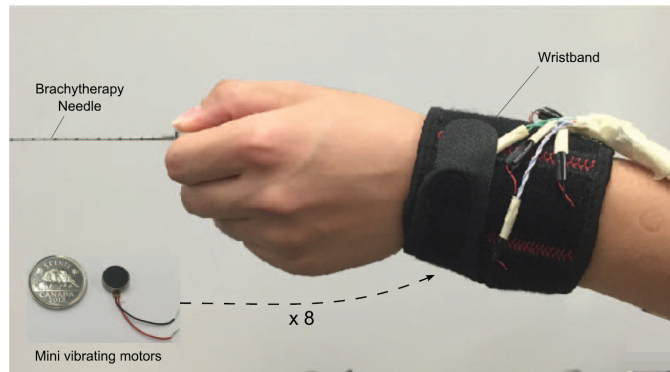
Figure 2.4: A wrist band applies haptic guidance to users attempting to steer a needle. Reprinted from ©2016 IEEE [6].

Furthermore knowing the axial component of the needle insertion force is helpful for performing interventions. For example, knowing when the membrane has been punctured and how many membranes were punctured can help users to stop the needle tip at a desired location. Epidural anesthesia is an example application where stopping the needle at the right location is important. Delicate needle manipulation is also required to prevent damaging the spinal cord. In addition, axial force information informs the user about tissue stiffness or friction from the surrounding tissue. Studies on the axial insertion force reported that the axial insertion force is the sum of friction forces, cutting forces, and the force due to elastic deformation of the tissue [8, 55]. These forces vary as a function of tissue properties, insertion speed, size of the needle and shape of the needle tip. In some cases additional haptic feedback based on forces measured directly at the needle tip may be particularly useful. Lorenzo et al. [33] demonstrated that membrane puncture detection can be more challenging when friction forces along a needle mask the effects of force variations at the

needle tip.

2.5   Texture Sensing

Humans determine the texture of an object based primarily on three types of tactile information: roughness, thickness/softness, and friction [56]. The majority of research on texture sensing and display has focused on two-dimensional surfaces: humans assess texture by lightly dragging their fingertips over a surface, often using [57]. Examples of texture sensing and display include [58,58–64]. For example, Mukaibo et al. built a custom robotic finger with five strain gages [58]. The gages were embedded at different locations of the finger to mimic cutaneous mechanoreceptors. Using these sensors the authors measured softness, friction, and roughness of a test specimen. For roughness sensing, the finger was scraped along the top surface of a material with a constant speed of $20\,\mathrm{mm/s}$, and a spectral analysis of the strain gage data allowed them to differentiate the textures of three different materials: towel, cork, and aluminum plate.

Fishel et al. [59] used the BioTac sensor (SynTouch, LosAngeles, CA, USA), an integrated multi-sensor device that can measure force, vibration and temperature. The contacting force and sliding speed were controlled while acquiring data. Three different aspects of physical interaction (traction, toughness, and tineness) were used to classify the texture. The current consumption of a motor driving a linear stage was used as an estimate of the traction force. The power of the vibration amplitude (in frequency domain) provided a measure of roughness and the spectral centroid was used to estimate the fineness of texture. A Bayesian texture classification scheme with these features showed a 95.4% success rate for 117 different texture samples.

Several other researches have used similar methods for texture sensing and classification [62,63]. When sensing the roughness of an object, they drag a force sensing tool or robot finger along the top of a test specimen to capture the force and acceleration changes due to roughness of the surface. The speed of drag is typically constant during the data collection. Spectral analysis is applied to the measured data in order to analyze it in frequency domain. Distinctive (large amplitude) peaks in spectral analysis plots are captured and used to classify the texture of a surface.

Much less work has focused on three-dimensional texture perception, yet this is the situation that occurs as a needle passes through tissue. One area of three-dimensional

texture sensing that has received attention is monitoring the qualities of fruit with a robotic probe. Taniwaki et al. demonstrated a fruit internal texture sensing system [65]. They designed a test setup with a piezoelectric sensor attached at the base of a sharp probe. As the probe was inserted into fruit, the piezoelectric sensor data were captures and used to differentiate the types and conditions of fruit. The sensor data were analyzed in the frequency domain. To reduce noise, the authors segmented the frequency range into multiple bins and averaged the data for each bin. Pears, persimmons, and apples showed distinctive differences in the frequency domain analysis.

Chapter 3

Force Sensing Needle

As discussed in the previous chapters, the MR-guided interventions involve a combination of technologies so that a physician can stand outside the MR machine bore and operate on a patient within. An important part of this scenario is to sense tool/tissue interaction forces, so that they can be relayed back to the physician. In this approach, force information, sampled and transmitted at up to $1\,\text{kHz}$, can complement the relatively slow refresh rate of MR images. Ideally, the system should allow a physician to feel as if her fingertips are inside the MR machine, manipulating tools directly. There is even the possibility to provide physicians with an unprecedented ability to sense forces right at the tip of a needle. This chapter presents one solution for measuring such forces and relaying them to a physician.

3.1   Needle Design

A force sensing needle has to be located inside the MR bore while images are acquired. Therefore, the sensors incorporated into the needle must be MR-compatible. There are three main criteria for compatibility. First, the components should be safe to use inside or near the MR machine. Due to the intense magnetic field, any ferromagnetic materials will experience large forces and may become projectiles. In addition, any conductive material can be heated by the strong radio frequency (RF) signal from the MR machine. Therefore, an ideal sensor should be composed of non-ferromagnetic and non-conductive materials. Second, the components should not deteriorate the quality of the MR images. In other words, any imaging noise or distortion arising from the sensing system should be minimized. Finally, the functionality of the sensing system should not be adversely affected by the MR

imaging environment. For example, the machine's large and dynamically varying magnetic field should not produce currents that affect the sensor operation, and they should not produce unacceptable noise in sensor readings.

A second design requirement arises from the geometry of the MR machine and the tools and procedures envisioned. In particular, if the goal is to sense forces at the tip of a slender tool, the sensors must be quite small.

The sensors must also be sufficiently sensitive to detect forces of clinical importance, such as the change in force that accompanies puncturing a membrane or passing through different types of tissue. Forces should additionally be sampled at a rate sufficient to take advantage of human sensitivity to dynamic forces. The peak sensitivity for human mechanoreceptors is on the order of 250-300 Hz [43], but humans can sense vibrations up to 1 kHz. This means that the sampling rate for the sensor should be at least several hundred Hz. The tissue surrounding the needle will attenuate high frequency strains, so sensors at the base of the needle may not need a bandwidth or sampling rate above 100 Hz. However, the tip of the needle has the potential to provide textural information at frequencies of a few hundred Hz, so a sampling rate of at least several hundred Hz is desirable.

Most commercially available force sensors are not MR-compatible and are not small enough to incorporate into the tip of a needle. The following sections present an approach using optical fibers that meets the requirements for MR-compatibility, compact packaging and fast sampling rate.

3.1.1 Fiber Bragg Grating(FBG) Sensor
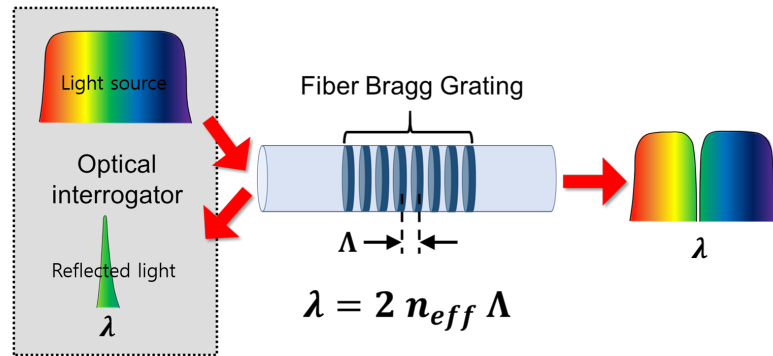
Figure 3.1: Diagram explains how the FBG sensor works.

Fiber Bragg grating (FBG) sensors constitute a type of optical strain gage. They are made by writing patterns into a glass fiber using intense ultraviolet light and a mask, which creates regions with a locally varying index of refraction. Broadband white light is transmitted through the fiber and a particular wavelength, corresponding to the spacing of the pattern, is reflected. As the fiber undergoes longitudinal strain, the pattern spacing increases or decreases, along with the wavelength of reflected light. An optical interrogator (Figure 3.1) tracks shifts in the reflected wavelength, providing an indication of strain, as shown in equation 3.1. Multiple FBGs with different wavelengths can be arrayed along a single fiber and tracked simultaneously.

The equation for the reflected wavelength is

$$\lambda = 2n_{eff}\Lambda \tag{3.1}$$

where n_{eff} is the effective reflective index, Λ is the grating period, λ is wavelength. The change in wavelength associated with strain can be expressed as:

$$\Delta\lambda_B = K_\varepsilon\varepsilon + K_T\Delta T \tag{3.2}$$

where K_ε and K_T are constants representing the sensitivity to mechanical strains and temperature variations, respectively. The temperature sensitivity is substantial and necessitates temperature compensation in most applications.

The typical diameter of an optical fiber is 125µm but fibers as small as 80µm are available. Therefore, the fibers are suitable for embedding in longitudinal grooves on the surface of a needle. When the fibers are firmly bonded to the interior walls of the grooves, they experience strain as the needle bends or undergoes axial extension or compression. Using three parallel fibers, each containing multiple FBGs, it becomes possible to estimate the overall bending profile and loading on the needle by tracking shifts in the reflected wavelengths (Figure 3.2).

3.1.2 Needle Geometry and Mechanical Strain

A starting point for the needle used in this thesis was a previously developed needle with three longitudinal fibers and two sets of FBGs [3]. An additional triplet of FBGs was placed along the shaft to improve the accuracy for bending deflections, and additional FBGs were added at the tip for force sensing (Figure 3.3). The sensors for bending deflection were
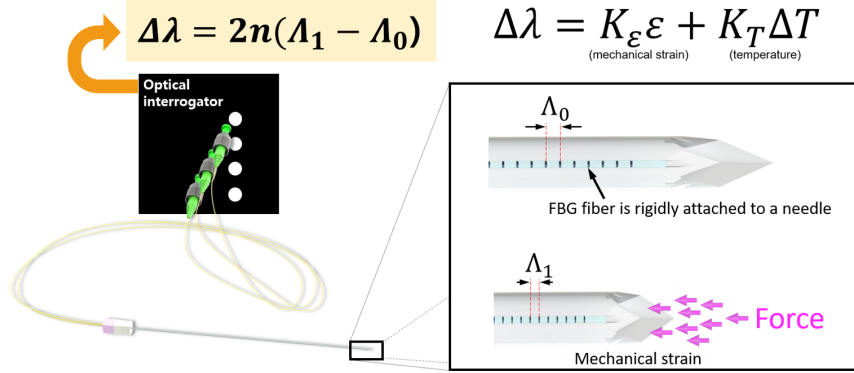
Figure 3.2: Schematic showing how forces in a needle are monitored using optical fibers and an interrogator.

located at z=31 mm, 81 mm and 131 mm. The tip sensors required a modification to the needle geometry as discussed in the following paragraphs.
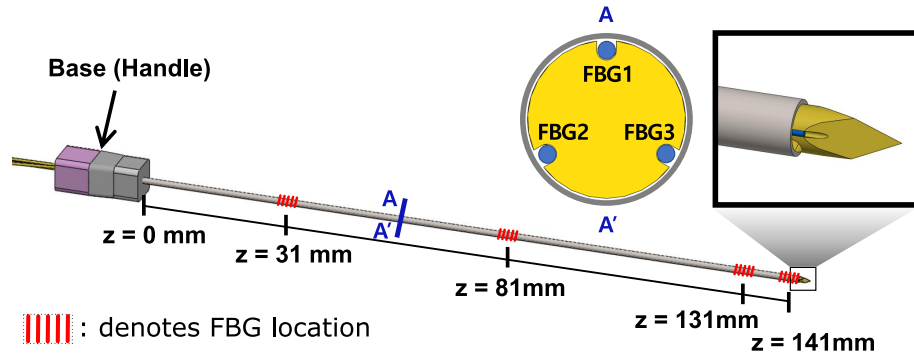
Figure 3.3: Design of a force sensing needle. A total of 4 sets of 3 FBG sensors are located along the needle axis. The set of sensors at the tip has features to improve the axial sensitivity, shown in greater detail in Figure 3.6.

The design goal of the force sensing needle to to measure the three components of forces at the tip. The minimum number of FBGs is therefore three. As with the FBGs along the shaft, the FBGs are in fibers placed 120 degrees apart and embedded in U-shaped grooves (Figure 3.3). When a compressive axial force is applied, all three distal FBGs will experience a compressive strain. Although the gages are near the needle tip, bending strains nonetheless produce the largest effects from radial forces. For example, when a force is applied in the +x direction, the strain in FBG3 will be compressive, the strain in FBG2

will be tensile, and FBG1 will be unaffected (Figure 3.4).
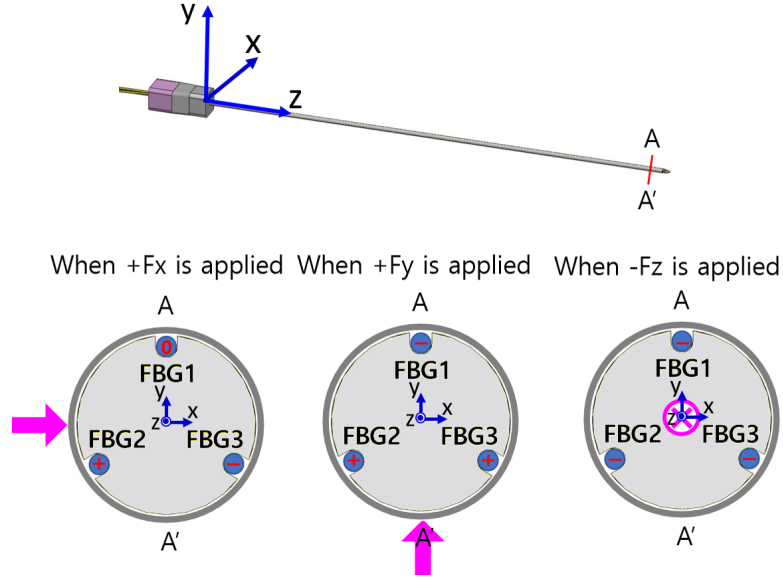
Figure 3.4: Showing how the wavelength changes depending on the Fx, Fy and Fz force applied at the needle.

Unfortunately, the strains from axial loads are much smaller than those from bending. Equations 3.3 and 3.4 show the estimation of the axial and radial force sensitivity for 18-gage (OD 1 mm) needle. For example, if equal forces are applied in the axial and radial directions ($f_r = f_z$), and given that $l = 5$ mm and $r = 0.5$ mm for an 18 gage needle, the strain caused by the axial force is only $1/40$ of the strain due to the radial force:

$$f_z : \epsilon_a = \frac{f_z}{A} = \frac{f_z}{E\pi r^2} \tag{3.3}$$

$$f_r = \sqrt{f_x^2 + f_y^2} : \epsilon_b = \frac{Mc}{EI} \approx \frac{4f_r l}{E\pi r^3} \tag{3.4}$$

where f_z and f_r are respectively the axial and radial forces at the tip of a needle, A is the cross sectional area of the needle, E is the material Young's modulus, $c = r$ is the radius of the needle, and l is the distance from the FBGs to the needle tip. In addition there is the difficulty that the effects of axial forces and temperature changes are indistinguishable, as both produce uniform axial strains in a symmetric column.

3.1.3 Axial Sensitivity

To address the problem of comparative insensitivity to axial forces, the needle tip geometry was modified. In a first iteration, a long oval hole was micro-machined in the needle tip to increase the strains at the FBGs and to make the needle cross section asymmetric so that axial loads and temperature changes would not affect the gages equally. The design is illustrated in Figure 3.5 (B). Because the length of the FBG sensors was 5 mm, the length of the hole was designed to be 8 mm to ensure that it exceeded the FBG length. A finite element analysis tool in SolidWorks (linear elastic isotropic model, solid mesh, static analysis, iterative solver, mechanical properties of MP35N Inconel alloy) was used to estimate the strength and axial sensitivity of the design. The needle was "blunted" to apply axial and radial stresses at the tip (Figure 3.6).

Table 3.1 shows how the strain from the axial force is increased by adding a long hole near the tip. Axial sensitivity improves by a factor of approximately 3.5. However the design also increases the danger of a buckling failure. If the needle is fixed at $z = 130$ mm (from the base of the needle), the design in Figure 3.5 (B) can endure only about 1/3 as large an axial load as the original needle before buckling.

A second iteration on the design, shown in Figure 3.5 (C) improves on the first iteration with a series of small oval holes with with 0.75 mm spacing. These create local stress concentrations in the vicinity of the FBGs. Because bending loads are small at the needle
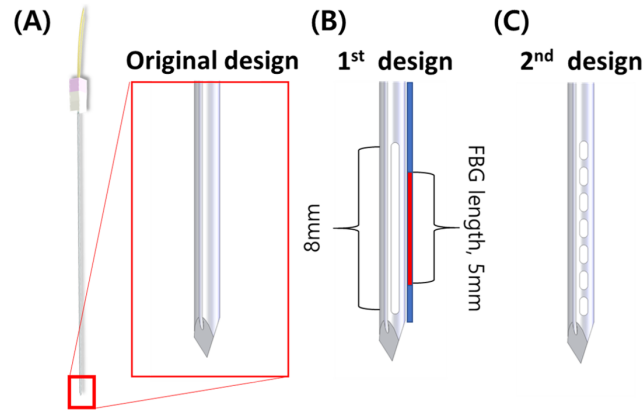
Figure 3.5: Design iteration of the force sensing needle for improving axial force sensitivity. (A) shows the design of a plain needle, (B) is the 1st needle design with a long hole at the tip and (c) is the 2nd design with a series of shorter holes.

Table 3.1: FEA result of each needle design

	Original design	1st design	2nd design
Axial strain	-0.602 με	-2.058 με	-1.837 με
Buckling load	168.84 N	60.28 N	80.15 N

tip, the stress concentrations are not a concern. The result is a design with improved axial force sensitivity over the original needle and a higher buckling resistance as compared to the design in Figure 3.5 (B). When the base of the needle is held fixed, equation 3.5 explains why the second iteration can endure a larger axial load:

$$P = \frac{n^2 \pi^2 EI}{4L^2} \tag{3.5}$$

where P is the buckling force, n is the buckling mode (n=1, 2, 3...), E is the Young's modulus of the needle material, I is the second moment of inertia, and L is the length of a portion of the needle under consideration. Since the second design has more bracing, the average value of I is higher and the effective length of L is lower. FEA result shown in Table 3.1 confirmed the second design has higher buckling load than the first design.

While increasing the width of the holes within manufacturing limits, the spacing between holes was adjusted to improve axial sensitivity. Figure 3.6 shows that the axial force sensitivity increases as hole spacing varies between 1.25 mm to 0.75 mm and continues to increase at a lower pace as the spacing becomes smaller.
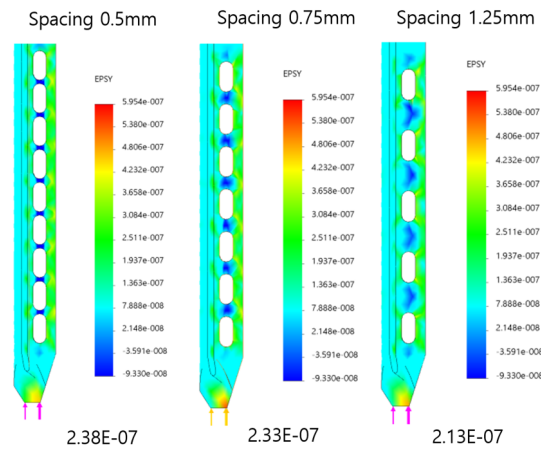
Figure 3.6: FEA results for each spacing distance of the holes

The axial resolution ultimately depends on noise, and if a value that we measure is three times larger than the standard deviation of the baseline noise distribution, we can differentiate the value from the baseline noise with about 94% of statistical confidence. Based on the RMS error of the plain needle and FEA analysis result, we decided that the final design should have seven rounded holes (0.36 mm width and 0.85 mm length) with 0.75 mm spacing.

Load Applied at Tip	ε_{avg}, needle with holes	ε_{avg}, plain needle	ratio (modified:plain)
Fy = 0.1N	3.145 e-5	1.817 e-5	1.73
Fz = 0.1N	-1.837 e-6	-6.02 e-7	3.05
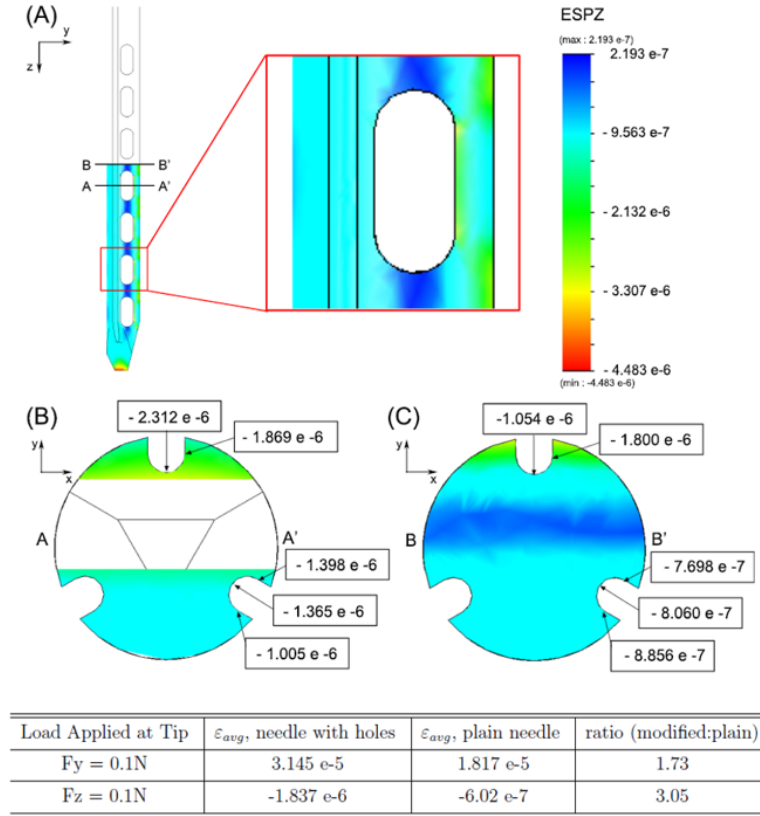
Figure 3.7: FEA result with the final design. (A) Close-up of FEA results of axial strains produced by $F_z = 0.1$ N axial force at (B) a location centered over one of the oval holes near the middle of the modified region and (C) in a solid part of the cross section.

Figure 3.7 shows the FEA result for axial and radial force loading conditions. The ratio between axial and radial force sensitivity is approximately 1:17 and the axial sensitivity is improved by 300% as compared to the original solid needle.

3.2 Needle Fabrication

An off-the shelf 18 gage MR-compatible biopsy needle (Model MR1815, Bracco Diagnostics, Princeton, NJ.) with trocar tip was used to manufacture the force sensing needle. The biopsy needle was consisted of two parts, an inner stylet and an outer cannula. The inner stylet of the needle was made of MP35N (a nickel-cobalt based alloy); the cannula was Inconel 625. The length of the stylet was 15 cm and the diameter was 1 mm. The outer cannula has 1.27 mm outer diameter and 1.1 mm inner diameter.

First, the plastic needle base (handle) was removed from the stylet by heating it with a heat gun. After 1 to 2 minutes, the plastic base became soft enough to be removed from the stylet. After removing the base, the inner stylet was machined.

To embed the FBG fibers, wire electrical discharge machining (EDM) was used to create three U-shaped grooves. Advantages to EDM include the ability to create very small features, negligible contact forces that could bend delicate structures and no possibility of shedding fine particles that could affect the MR images. The array of small holes near the tip was also created by EDM. An 80μm wire was used for both the grooves and the hole features (Figure 3.8).
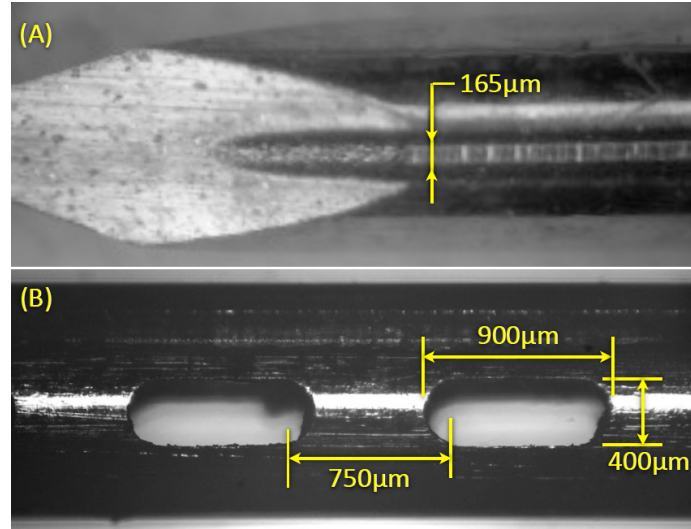
Figure 3.8: Microscopic picture of the machined needle after EDM. (A) shows the grooves for embedding the optical fiber. (B) shows the designed feature near the tip to improve the axial force sensitivity of the needle.

Before embedding the fibers, the FBG sensor location was confirmed by hovering a

soldering iron near the fiber and passing it along the fiber length. The heat from the iron produced a rapid change in the FBG signal as the iron passed, making it possible to record the FBG locations.

Three optical fibers were glued inside of each of three grooves using a medical grade epoxy (Loctite EA M-31CL) and a cyanoacrylate glue (Loctite 401). The cyanoacrylate glue was used in the initial positioning of the fiber. It was applied at the tip of the fiber and 150 mm from the tip to hold the fiber in place while the epoxy cured. The cure duration of the epoxy was over 3 hours so fibers were glued one by one with 6 to 8 hours between each gluing process. Two types of optical fiber were used to make two needles. The first needle used 125μm diameter optical fibers and the second used 80μm optical fibers. A digital microscope was used to display the real time image of the magnified needle and fibers during the alignment and gluing process. The plastic needle base was reattached after the fibers were glued to the needle. An additional boot was mounted around the fibers where they exit the base to prevent the fibers from bending damage.

The fibers were connected to the interrogator using either FPC/APC or E2000 connectors, depending on the version of the needle. An initial version of the needle used the E2000 connector and an optical splitter to multiplex three fibers into a single channel of the interrogator. A newer version of the needle had FC/APC connectors allowing direct connection between each fiber to one channel of the interrogator. This revision was made to prevent the wavelength peaks from overlapping when the needle was subjected to large bending loads.

3.3 Needle Characterization

Data were collected under several different conditions to evaluate and calibrate the needle.

First, data were collected with varying loads from 0.005 N to 0.05 N in the x, y, and z directions. Figure 3.9 shows a typical wavelength variation, $\Delta\lambda$, versus force plot for one FBG sensor (FBG12, at the tip of the needle). Each point represents the difference between the minimum and maximum force over one period of the force variation. The forces are applied by a muscle lever (Model 305B, Aurora Scientific Inc., Ontario, Canada). FBG 12 is counter-clockwise from the top gauge (FBG 10) when viewed from the xy-plane. Due to its placement, it is more sensitive to loads in the x-direction than in the y-direction, as expected.
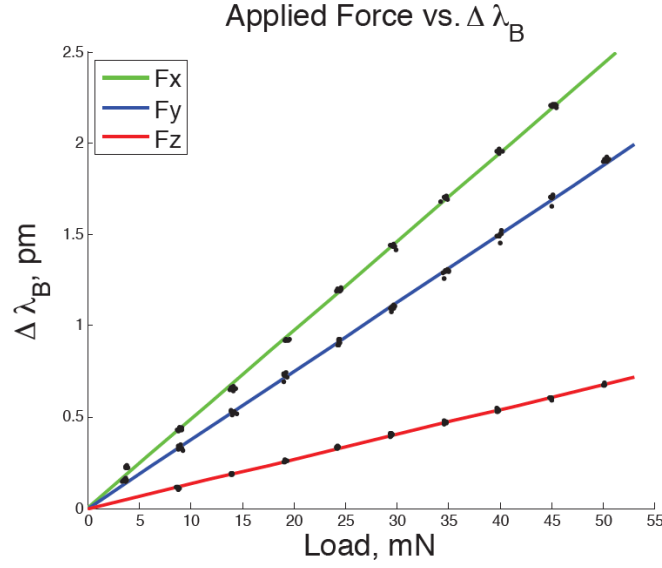
Figure 3.9: Plot of wavelength shift to applied force for one FBG sensor at the needle tip (gauge number 12).

To test the frequency response of the needle and sensors, the needle was connected to a subwoofer, acting as a linear voice coil actuator, with a load cell at the center of its suspension pressing axially against the tip of the needle. The needle was attached to the load cell through a small amount of hot-melt-adhesive polymer to prevent damage to the needle tip. A 5-500 Hz chirp signal was applied to the speaker through a function generator and amplifier, and data from the load cell and FBG sensors were collected. The transfer function between the load cell and the average response over the tip 3 FBGs was obtained using the ETFE (empirical transfer function estimation) method. The frequency range was split into 45 equally spaced bins and the transfer function was averaged across the bins and multiple samples to minimize the noise. As seen in Figure 3.10 the frequency response of the needle is nearly flat over the range tested, with some increase in amplitude above 200 Hz, likely due to a small amount of bending that occurred at these higher frequencies.
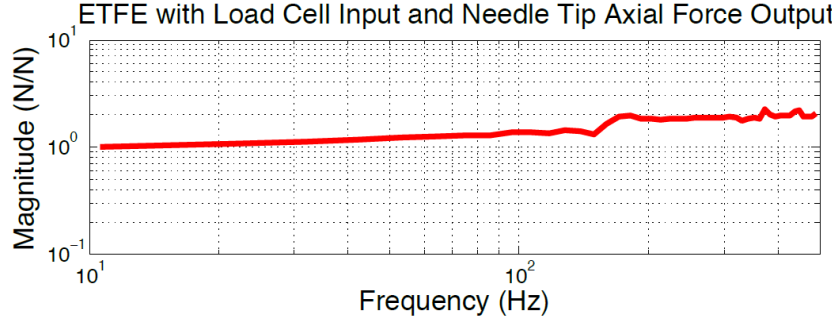
Figure 3.10: Plot of response to axial loading shows relatively constant amplitude over the frequencies of 10-500 Hz.

3.4 Force Calibration

In order to use the force sensing needle, it has to be calibrated with reference forces. The wavelength shift is linearly proportional to the strain caused by a force applied at the tip:

$$\Delta\lambda = (1 - P_e) * (\epsilon_z + \alpha\Delta T)\lambda + \zeta\Delta T \tag{3.6}$$

where λ is the reflected wavelength, P_e is the equivalent photoelastic coefficient, T is temperature, ϵ_z is axial strain, ζ is the thermo-optic coefficient of the FBG and α is the thermal coefficient of expansion of the material to which the FBG is bonded. For an FBG centered around 1550 nm, typical values are $P_e = 0.22$, $\alpha = 0.55e\text{-}6/$°C, and $\zeta = 10$ pm/°C for silica fiber. This equation can be simplified to:

$$\Delta\lambda = K_{force}\Delta F + K_{temperature}\Delta T. \tag{3.7}$$

Since the equations for force, F, and the reflected wavelength, $\Delta\lambda$, are linear, a 3×3 calibration matrix to map wavelengths to forces can be created:

$$\begin{bmatrix} \delta F_x \\ \delta F_y \\ \delta F_z \end{bmatrix} = C_{force} * \begin{bmatrix} \Delta\lambda_{3i-2} \\ \Delta\lambda_{3i-1} \\ \Delta\lambda_{3i} \end{bmatrix}. \tag{3.8}$$

The calibration matrix can be obtained from multivariate linear regression:

$$\delta f_n = C_{force} \cdot \delta s_n \tag{3.9}$$

$$C_{force} = \delta f_n \cdot \delta s_n [\delta s_n \delta s_n{}^T]^{-1} \tag{3.10}$$

where $\delta f_n = [\delta F_x, \delta F_y, \delta F_z]^T$ and $\delta s_n = [\Delta\lambda_{3i-2}, \Delta\lambda_{3i-1}, \Delta\lambda_{3i}]^T$.

For the tip force calibration, the changes in the wavelength from each FBG were measured with known loads applied to the needle tip. As explained above, the FBG sensors are sensitive to both temperature and force. The next sections address calibration methods and temperature compensation.

3.4.1 Setup for Force Calibration

A commercial optical interrogator (Model sm130-700 (2kHz), Micron Optics, Atlanta, GA) sampled the FBG wavelengths at $2\,\text{kHz}$, with 0.1pm resolution.

We assume a uniform temperature for each triplet of FBGs along the needle length. Hence, variations in temperature should affect each FBG equally. However, as seen in Figure 3.7, axial strain at the top FBG in the distal triplet is greater than that of the lower FBGs due to the modified cross-section at the tip. Consequently, the effects of temperature and axial loading should be separable. Nevertheless, to minimize the temperature effects on the force calibration, the tip was loaded with a muscle-lever arm (Model 305, Aurora Scientific Inc., Ontario, Canada) at $5\,\text{Hz}$. The muscle-lever arm can apply controlled dynamic forces with different magnitudes with a resolution of $1\,\text{mN}$ with a 0.2% force to signal linearity over a range of frequencies from 1 to over 200 Hz. Forces were also measured with a commercial ATI (Industrial Automation, Apex, NC) force/torque sensor. With the needle isolated in a foam-lined box, the dynamic force variations are easily distinguished from the much slower effects of ambient temperature variations.

The needle base was fixed to miniature linear stages to allow additional adjustment of the needle orientation. In order to apply load properly with the lever arm, a small extension spring, and a thin nylon thread were added to make a connection between the lever arm and the needle tip. This extension spring helped to preload the needle in tension to minimize strains due to bending as shown in Figure 3.11 (A). The thread was passed through the oval hole nearest to the tip and tied to make a loop. The the extension spring is connected to the loop for axial force loading. The thread was located collinear with the needle axis.
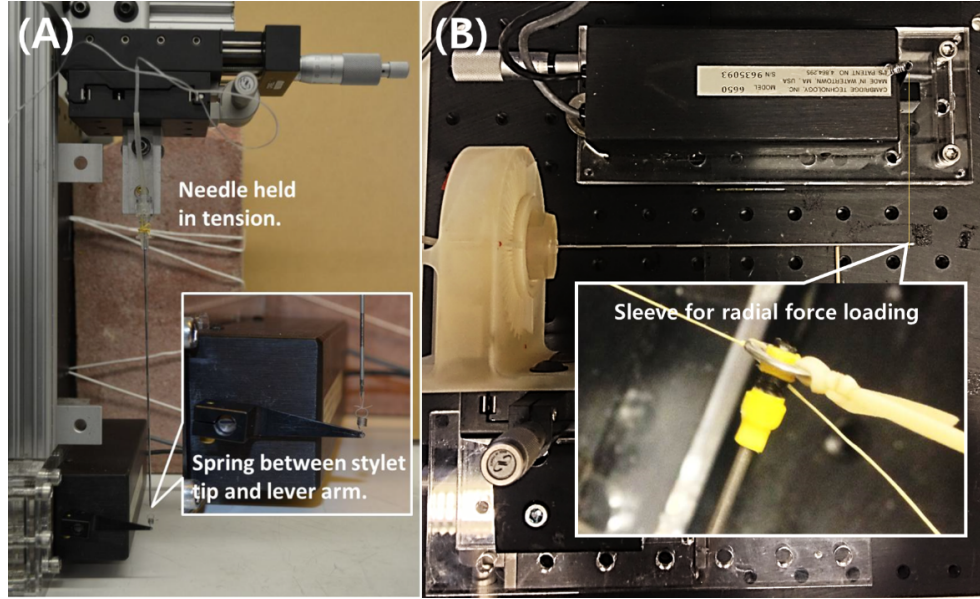
Figure 3.11: Detailed views of the loading connections for the axial and rotational calibration of the force sensing needle.

To obtain data for axial loading, the lever arm applied 5 Hz sinusoidal loading of which magnitude was varying from 0 to 0.25 N.

For radial forces, a new component was designed to rotate the base of the needle and fix it in various orientations. Figure 3.12 shows the setup for radial force calibration. The apparatus in Figure 3.12 (B) has grooves and four fins to fix the needle base for every 5°. Unlike the axial force, the radial test setup used a plastic guide ring to connect to the lever arm. The base of the needle rotates over 360° and twists the thread passed through the hole. This twisting creates an undesired torque applied at the tip and introduces small errors when measuring the strains around the needle tip. The guide plastic ring shown in Figure 3.11 (B) was designed to apply purely radial forces at different rotation angles without the artifact resulting from the thread. Similar to the previous axial force calibration, the lever arm applied a 5 Hz sinusoidal load of various magnitudes.

The sampled FBG data were filtered with a 10th order Butterworth filter to high pass frequencies above 2 Hz and low pass frequencies below 15 Hz to eliminate the thermal noise. A peak detection algorithm in MATLAB was used to find the wavelength shifts for the corresponding applied loads. Loading the needle dynamically with the muscle-lever arm allows us to eliminate temperature effects and explore the sensors' response to dynamic tip
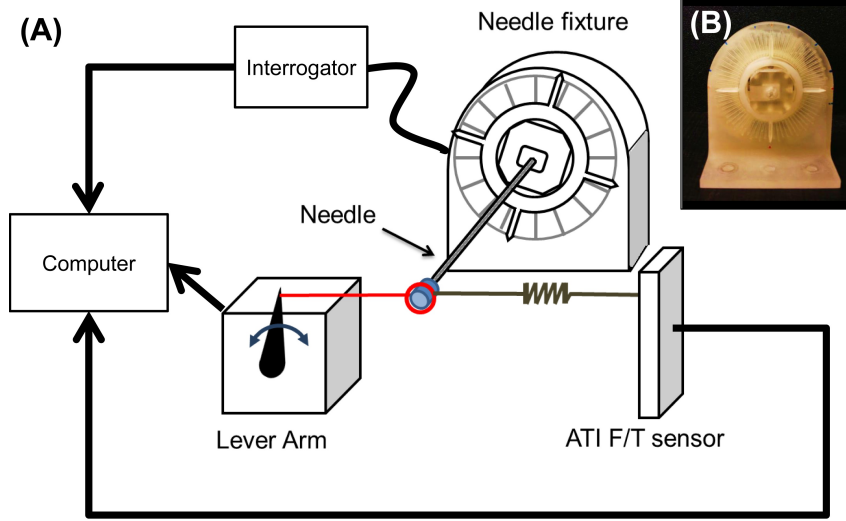
Figure 3.12: (A) Schematic of the needle calibration set up to measure wavelength shift due to various transverse loads while rotating the needle base 0° to 360°. (B) 3-D printed apparatus to fix the needle every 5°.

forces.

Figure 3.13 shows a typical result from the radial force calibration. The magnitude of loading remained the same for all the data points while the orientation of the base changed from $0\,°$ to $360\,°$. This plot shows how the sensors at $z = 135\,\mathrm{mm}$ and the tip ($z = 145\,\mathrm{mm}$) are actually spaced and how the features at the tip affected the reading. As shown in the lower plot of Figure 3.13, the change in wavelength for FBG10 has a smaller magnitude compared to FBG11 and FBG12, due to the asymmetric cross section near the tip of the needle. In comparison, the magnitudes of the upper plot are very similar because the three FBG sensors at that location (FBG7, FBG8 , FBG9) are located at $z = 135\,\mathrm{mm}$ where the needle has a solid cross section. A similar approach to determine the locations of fibers was taken by [66].

3.4.2   Force Calibration Results

Figure 3.14 shows the actual and estimated loads for data from the loading and temperature calibration tests. The best method for calibration was to filter out thermal effects and use a 3×3 calibration matrix to map wavelength shifts at FBGs 10, 11, 12 to (F_x, F_y, F_z) at the tip. The mean errors of force calibration for x, y and z directions are -1.1 mN (SD=8.4 mN),
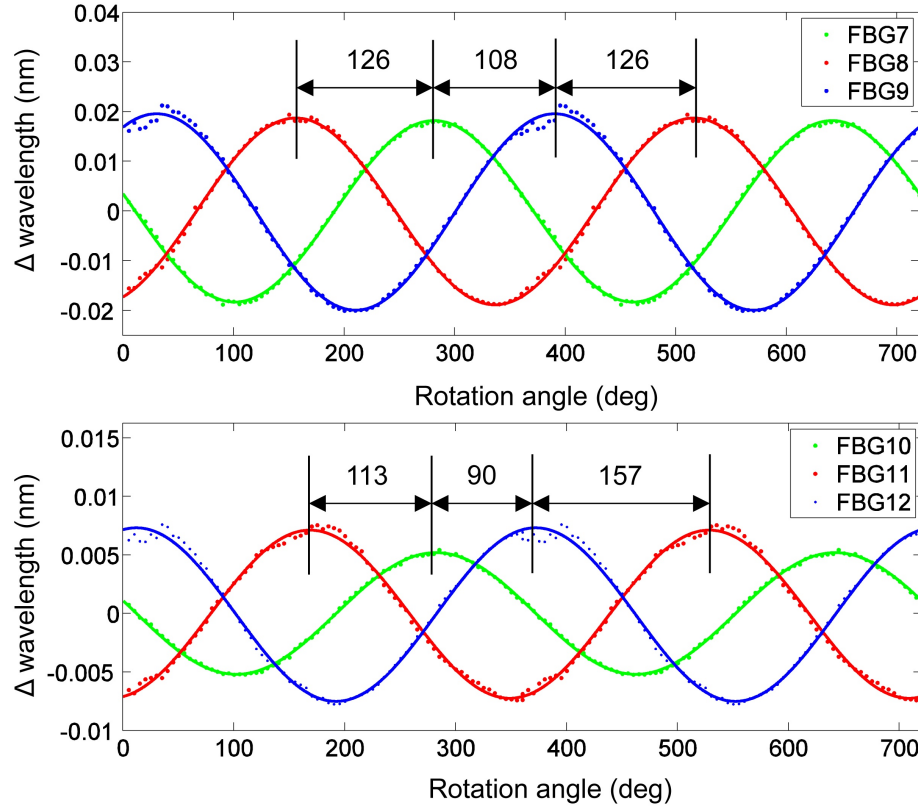
Figure 3.13: Data of wavelength shift for varying direction of applied transverse load at the (A) third and (B) fourth sensing locations.

-0.4 mN (SD=16.5 mN) and -1.2 mN (SD=4.4 mN) respectively.

3.4.3   Temperature Compensation

When the needle is inserted into the human body, the change in temperature from ambient temperature (typically 20 ℃) to body temperature at 37 ℃ produces a significant thermal strain which, for a symmetric needle cross section, is indistinguishable from the effect of a purely axial force.

For the original needle design, the expected wavelength shifts due to mechanical strains are comparable to those from temperature changes. Recall from Equation 3.6, a thermal strain caused by 1 ℃ change is 0.022 nm with a center wavelength of 1556 nm. This means that the wavelength shift for a 1 N axial load is similar to that of a temperature change of 1 ℃. The wavelength shift from a 1 ℃ change in temperature is comparable to the
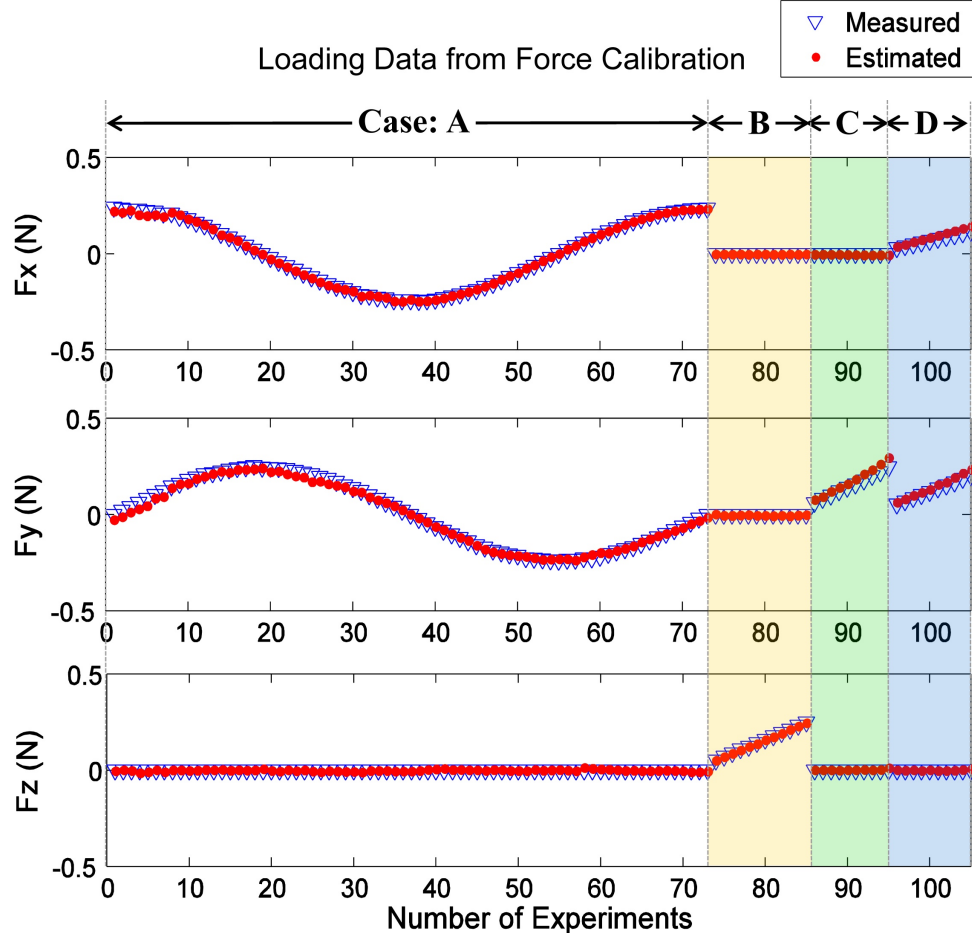
Figure 3.14: Actual and estimated tip loads in F_x, F_y, and F_z for loading experiments. Case A: when the transverse loading was varied; B: when only the axial loading was applied; C: when only forces in the y direction were applied; D: when forces in the x and y directions were applied.

wavelength shift due to a 1 N change in axial force, which is well within the range of forces that we desire to measure.

The modified needle design with asymmetric cross section has a potential to reduce the temperature effect. As shown in the FEA result (Figure 3.7), when the axial force is applied at the tip, the top FBG sensor is experiencing a slightly larger strain than other two FBG sensors because of the asymmetric geometry. On the other hand, the thermal strain from the temperature would be very similar for all three FBG sensors because the needle is thin.

One method to separate thermal strain and axial loads is by utilizing a filter for the
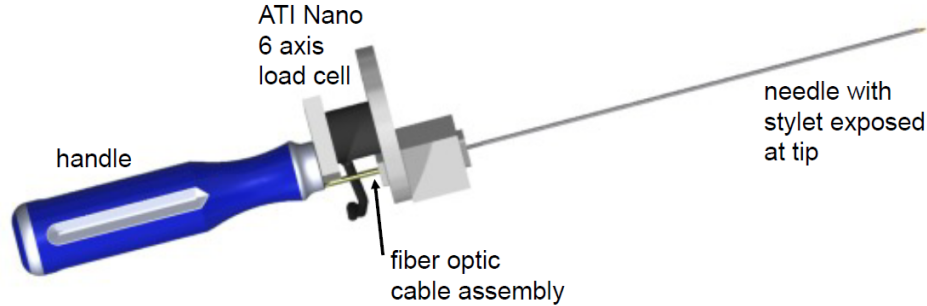
Figure 3.15: Needle fixed to a 6-axis force/torque sensor with handle for insertion experiments.

reduction of thermal noise. Wavelength changes caused by thermal variations are slow compared to those produced by dynamic loads on the needle. The filtering frequency range is selected by analyzing the lowest and highest frequencies of forces during needle biopsy interventions. Most of the lowest frequencies are in the tens of Hz, but when the needle is scraped against relatively hard textured surfaces (e.g. scar tissue), or when it punctures a membrane, the highest frequencies can reach over $100\,\mathrm{Hz}$. Thermal changes however, occur on the order of $1\,\mathrm{Hz}$.

Depending on the situation, different temperature compensation methods were used. Each method will be briefly described in following sections where we used the temperature compensation for display axial force.

3.5 Result: Comparing Forces at Tip vs. Base

The first tests of the instrumented needle were aimed at comparing it to forces sensed at the needle base. For this comparison, the needle was affixed to a small 6-axis force/torque sensor (ATI Nano 175), which was mounted to a small plastic handle. An illustration of the arrangement is shown in Figure 3.15. With this apparatus it is possible for a user to insert the needle into tissue phantoms, while recording forces from the needle tip using the FBG sensors and from the needle base using the force/torque sensor.

To show the correlation between the FBG data and the force/torque sensor data, the handle assembly was first used to tap on a sample of urethane rubber (shore 60A durometer) in a water bath. The needle tip was pressed against the rubber, tapped three times and
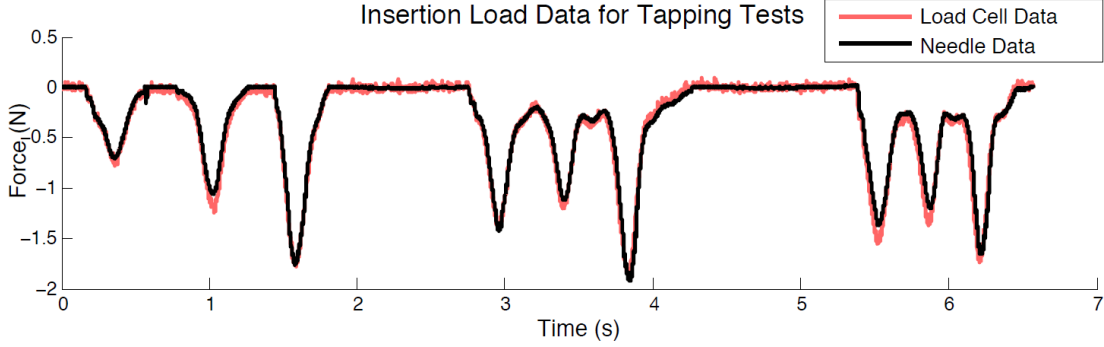
Figure 3.16: Axial FBG data from needle tip compared to force data from needle base during tap testing.

lifted completely off the rubber three times. The initial non-contact readings from both the force/torque sensor and the needle were subtracted from the readings during contact. For the needle, the wavelength common mode (i.e., the average wavelength shifts for the three distal FBGs) gives the wavelength change due to axial loading for comparison with the measured f_z force from the force/torque sensor. As seen in Figure 3.16 the recorded signals from the needle tip and the force/torque sensor at the needle base are nearly identical, with a lower noise floor in the case of the needle. This correspondence is to be expected as the tapping velocities were relatively low, so acceleration forces due to the mass of the needle did not significantly affect readings from the force/torque sensor in this case. A more interesting comparison is seen in Figure 3.17. In this case the needle was pushed through a Plastisol phantom (2:1 ratio of plastic and softener). The needle went through the phantoms skin, which included three layers of plastic and wax sheets, pierced two inner membranes, came in contact with a hard surface, and then was completely extracted.

As in Figure 3.16, the axial components of the needle and force/torque data are compared. Visible events in Figure 3.17 are verified from video data and include membrane contact and puncture (b), hitting a hard surface (e), and exiting through membranes (f), which can be seen more clearly in the FBG data compared to the load cell. A tap was used to synchronize the F/T sensor, FBG, and video data, and can be seen before (a) initial contact with the phantom.

The needle stylet tip is partially exposed outside the needle sheath, and one hole is partially visible outside the sheath. The tip forces experienced at the needle during insertion and piercing of the three-layer skin at (b) at times became larger than zero, and it is
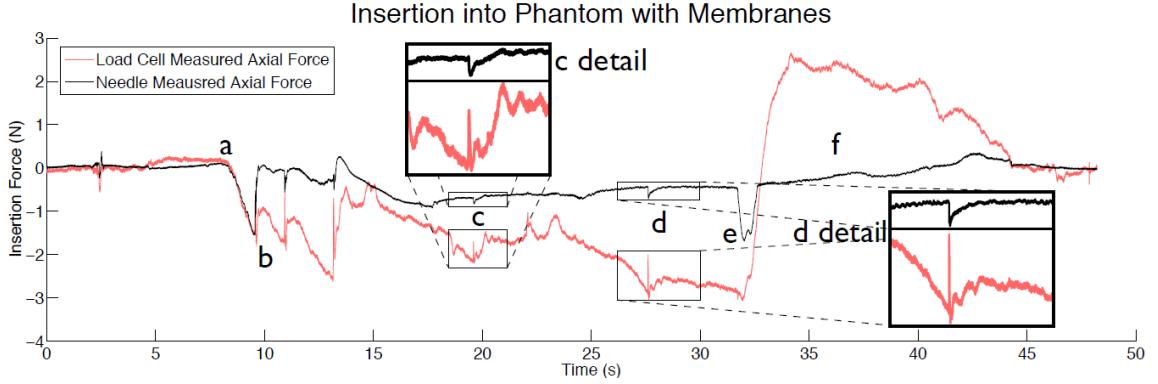
Figure 3.17: Axial FBG data from needle tip compared to force data from needle base during insertion in phantom: (a) initial contact of needle and phantom, (b) piercing through the first of three skin layers, (c) piercing first inner membrane, (d) piercing second inner membrane, (e) hitting hard surface, (f) extraction of needle from phantom.

possible that the needle undergoes some tensile effects as the sheath edge gets caught on a membrane. Similarly, during the retraction phase (f) of the needle, the tip may experience some tension while pulling on the inner membranes on its way out, hence a positive force reading is observed in the FBG data.

Beyond the higher signal to noise ratio from the instrumented needle, a major difference is that the stylet is housed inside a sheath which slides against the tissues, producing friction forces that are transmitted to the needle base. The friction felt at the base masks the effects of small variations in the tip forces. Secondly, for sudden changes in velocity, the force sensor at the needle base experiences inertial forces due to the mass of the needle. The FBGs near the tip of the inner stylet do not experience either of these effects, and are therefore capable of discerning smaller dynamic forces at the tip.

3.6 Discussion and Conclusion

The data obtained from FBGs at the modified needle tip provide estimates of tip forces that are at least as accurate as those that can be obtained from a commercial, non MR-compatible force sensor. However, they can also provide force information not easily detected from the base of the needle. In particular, when friction between the needle sheath and tissue is significant, the tip sensors are better able to discriminate small variations in the tip forces. This instrumented needle has potential to validate models on needle interaction

forces in vivo. This needle can be used in subsequent chapters to conduct controlled haptic experiments to determine whether subjects can easily detect events such as puncturing a membrane or targeting an object which is movable. The purpose of these user studies would be to show whether the ability to sense tip forces directly (as one physician put it, "to shrink ones fingertips and put them at the tip of needle") is useful in clinical practice.

Chapter 4

Radial Force Display

As noted in Chapter 1, locating the needle tip at a desired location is essential for successful needle interventions. However, it is often challenging due to the movement of the target. Because target tissue and other organs are not rigidly fixed inside of the patient's body, if the tip of the needle contacts the target at an angle or hits the side of the target instead of the center, the needle can exert an undesired torque or side load on the target and cause target movement. When this occurs, the corresponding radial force on the tip of the needle can provide information about the contacting angle and the needle tip location relative to the center of the target. Therefore, if this information is relayed to a user, it could reduce the number of failures prior to a successful targeting action (positioning the needle tip inside the target).

4.1 Preliminary Test

4.1.1 Design of a Non-collocated Haptic Device

To display the forces applied to the tip of the needle, we designed a first prototype which has three non-collocated skin deformation tactors, as shown in Figure 4.1. Green and blue tactors were dedicated to mapping F_x and F_y (radial forces) respectively, and the other tactor displaced skin to display the F_z (axial) force. Each tactor movement was created by using a scotch yoke and a servo motor (HITEC HS-35HD). The size of the haptic device was 3.7 cm x 3.5 cm x 14 cm, which is similar to the dimensions of a biopsy gun. Users were asked to hold the device like a biopsy gun as shown in Figure 4.1. Forces measured at the

needle tip are linearly mapped to the displacements of tactors. The vector sum of the three independent displacements represents a force vector applied at the needle tip. For instance, if the direction of the measured tip force is a red arrow as shown in Figure 4.2, the tactors' displacement would as shown with magenta arrows.
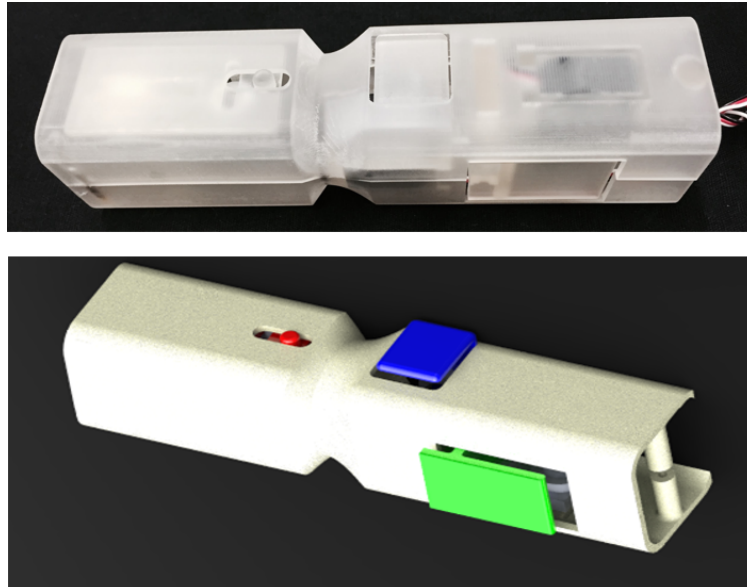
Figure 4.1: A prototype of the hand held skin deformation haptic device has three tactors that relay axial and radial forces through tactor displacements. The size of this device was similar to the handle of a biopsy gun and the device was held like a biopsy gun.
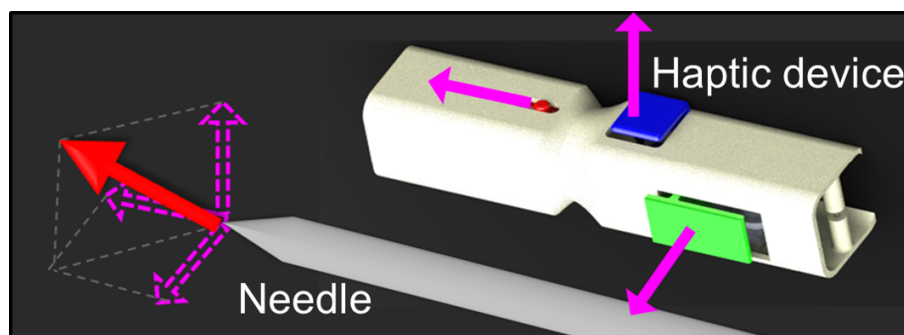
Figure 4.2: Configuration shows how a tip force direction is displayed through displacements of three tactors.

4.1.2   Pilot User Study

To test whether a user can successfully detect the tip force direction with this non-collocated
haptic device, a simple preliminary user study was conducted. Users were asked to feel the
tactor movements and determine the corresponding vector from the Figure 4.3. Although
the device can render any direction in a 3-D space, 8 possible vector directions were chosen
for the test. To calculate the accuracy of direction perception, 10 stimuli for each direction,
for a total of 80 stimuli, were relayed to the user during the test. The displayed direction
was changed randomly.
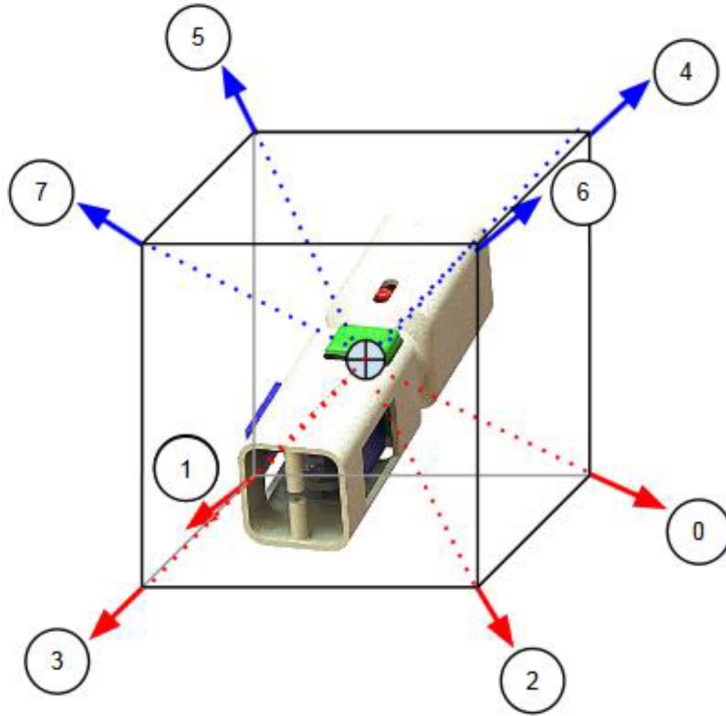
Figure 4.3: Figure shown to users during the preliminary user study. The user provided the
corresponding number for each direction based on the haptic stimulus they perceived.

In order to check how intuitive the device is, we first asked the user to guess the direction
before training. During this first part of the test, there was no training or trials to feel the
stimulus. Only verbal and visual explanation of the device were given to the users. Then
users were asked to feel the skin deformation stimulus and answer with the direction they
perceived. During this test, users did not have any feedback on their answers (i.e., how well

their guess matched the displayed directions).

After the first part of the test, we gave the users a training session. The session helped users match the tactor movements to the direction of the vector. After the training, the second part of the user study was conducted. As in the first part, the users answered with the perceived directions based on the skin deformation stimulus.

A total of 5 users participated in the test. As shown in table 4.1, successful detection of the direction was highly influenced by training. A paired t-test was used to check the statistical significance of the difference (P-value 0.0233).

Table 4.1: Test results of 5 human subjects. The training effect was significant.

	No Training	After training
User 1	11.25 %	90.00 %
User 2	48.75 %	78.75 %
User 3	63.75 %	85.00 %
User 4	61.25 %	93.75%
User 5	7.50 %	32.50 %

The confusion matrix shows that users often got 2 directions right but failed to guess all 3 directions correctly (Figure 4.4).

After the test, user feedback was collected. Many of the users reported that the non-collocated stimulus made it challenging to recognize the direction in three dimensions. In addition some of the users were confused because the tactors lost contact with skin due to the small size of their hands.

Based on these preliminary results, and because a passive teleoperation system (e.g. [67]) is likely to be more compliant in the radial direction than the axial direction – which suggests that axial forces may be transmitted adequately without a separate display – we created a new device that displays only radial forces. To reduce the confusion from the non-collocated display, we displayed collocated radial skin deformations. The grip style of the device was also changed to ensure skin/tactor contact for various hand sizes.

Direction Perceived

	0	1	2	3	4	5	6	7
0	34		5		1			
1	1	31		3		5		
2	1	1	32	1	1		5	
3		6		30		1		3
4		1			36		3	
5		1				37	1	1
6					1	1	38	
7								40

Direction Rendered
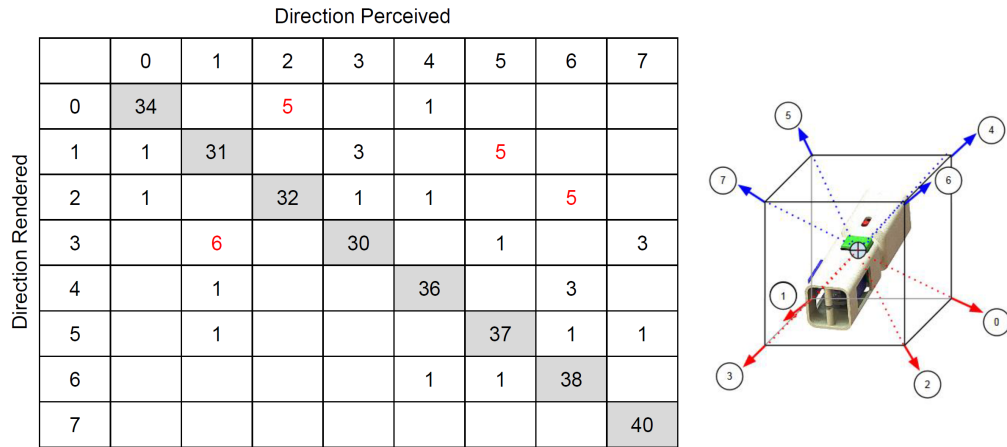
Figure 4.4: Confusion matrix of the non-collocated tactor result.

4.2 Collocated Skin Deformation Haptic Device

To design a collocated skin deformation display we first interviewed physicians who regularly perform needle interventions. The grip style of biopsy needles and biopsy guns were different as shown in Figure 4.5. Physicians held biopsy needles like a pencil while they held a biopsy guns like a tennis racket. Since the finger pad is in contact with the needle shaft to control the orientation of needle, perceiving tool-tissue interaction force could be more accurate, compared to the case of holding a biopsy gun.
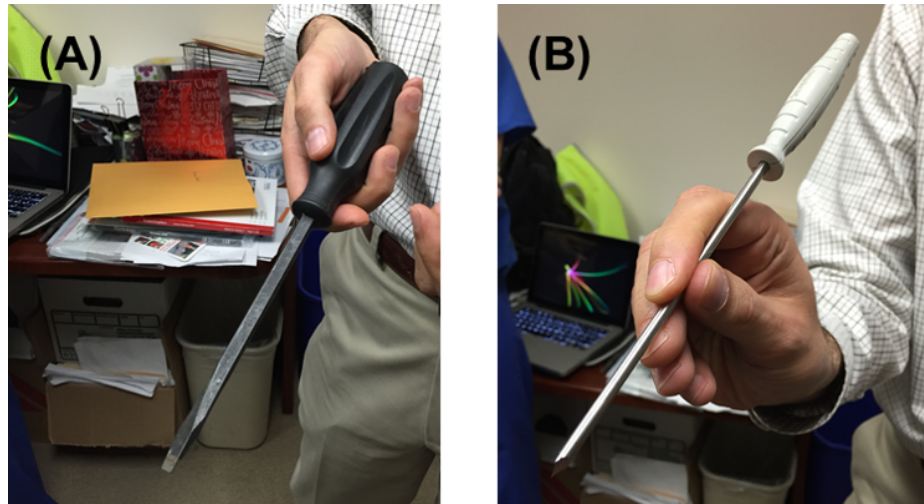
Figure 4.5: (A) a biopsy gun grip style, (B) a biopsy needle grip style.

4.2.1 Device Design

When doctors perform needle interventions, they experience skin deformation at the contact location between their fingertips and the needle due to tool interaction forces. In the radial force display, the haptic feedback device presents a small knob or post, which users grasp with their fingertips. The thin cylindrical shape of the knob makes the user hold it like a biopsy needle to create more realistic skin deformation. The backs of the fingertips are supported by a pair of external braces to maximize the skin deformation. The brace also helps when applying forces to the device.
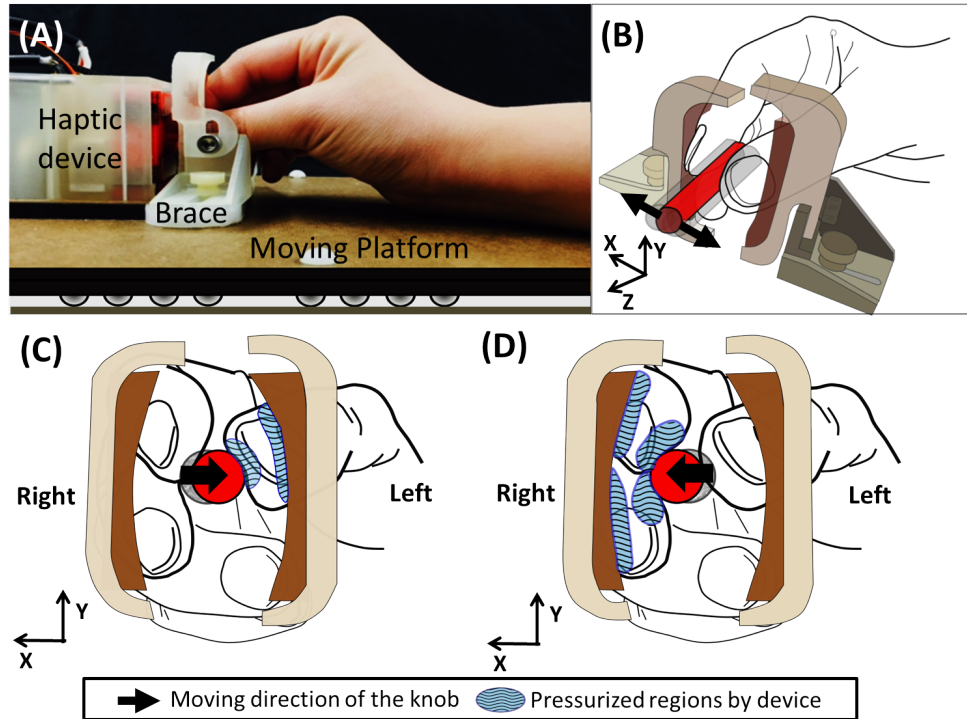
Figure 4.6: Subjects displace a freely moving platform to manipulate a needle while they interact with the haptic device (A). The haptic device imparts small lateral motions to a knob (B) which presses the subjects fingertips against braces. Subjects use the skin deformation cues on their fingerpads (C, D) to interpret what happens at the needle tip.

To impart the motion of the knob, we adapted a flexure mechanism presented in [68] as shown in Figure 4.7. In order to transform the rotational motion of the motors to small translational motions, the flexure contained two scotch-yoke mechanisms, one for x motions and one for y motions.
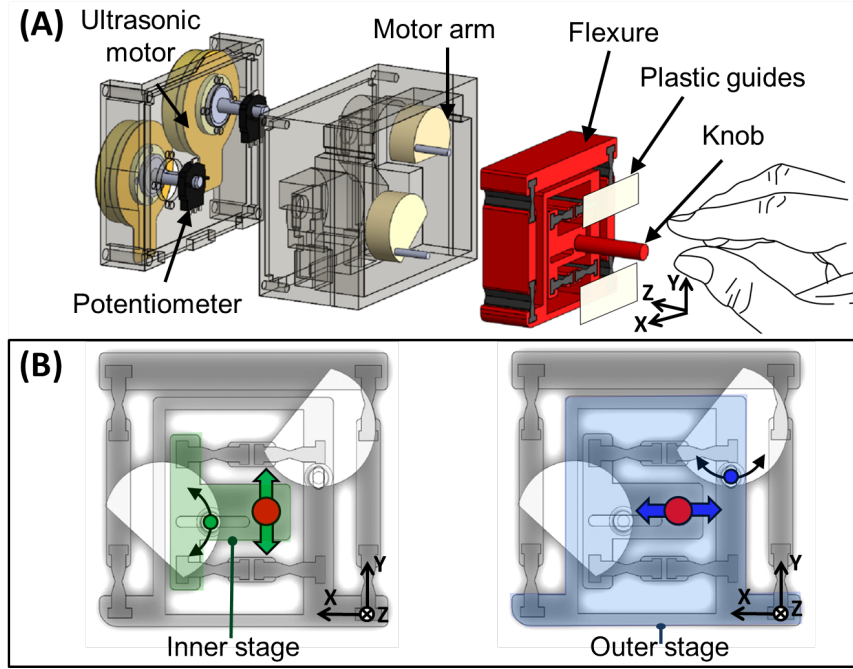
Figure 4.7: (A) Exploded view of the haptic device shows the arrangement of the ultrasonic motors, motor arms and flexure mechanism that enables Cartesian position control of the knob. (B) shows independent stages that two motors actuate with pins in slots to achieve position control in the x and y directions.

The flexure was printed with a 3D Printer (Flashforge Creator Pro), using polylactic acid (PLA) for the stiff components and thermoplastic elastomer (TPE) for the compliant components. Finite element analysis was performed in Solidworks to ensure that the two dimensions of the flexure had similar spring constants of approximately 1000 N/m. Nonplanar motion was minimized by adding additional plastic guides on top of the flexure, as seen in Figure 4.7.

Each motor has an arm with a pin which travels in a slot on its associated stage. The arm length, the distance between the center of the motor shaft to the pin, was 8.25 mm. Hence we are using a scaled-up version of the flexure design in [69] to apply larger forces at the fingertips. The radial contact forces sensed at the tip were mapped to the displacement of the device. In particular, the displacement of the knob produces normal and lateral skin deformation cues at the finger pads as well as pressure on the fingernails when the fingers were enclosed by the braces. These finger pad deformations are intended to be similar to those that occur naturally during interactions with pen-like tools when lateral forces are

applied at the tip. The knob can move $\pm 3\,\mathrm{mm}$ in either direction. On a finger pad, humans can perceive very small skin deformations, which are in the sub-millimeter range [4] so 0 to $3\,\mathrm{mm}$ of displacement range is adequate to display a wide range of force magnitudes. If needed, the maximum displacement could be increased further by elongating the slot length of the scotch-yoke mechanism.

4.2.2 Device Actuation

We chose Shinsei USR-30 piezoelectric ultrasonic motors to actuate the device because they are compact, high-torque, and MR-compatible (the vendor offers MR compatible variants for MR applications). For these reasons, these actuators have been used in other MR-compatible medical robotic systems in the past [70–72]. They also run very smoothly with no perceivable vibration, unlike most RC servos, making them a good fit for haptic applications. Their high torque capability makes gearing unnecessary for our application. Figure 4.8 shows the torque-speed plot of the Shinsei ultrasonic motor.
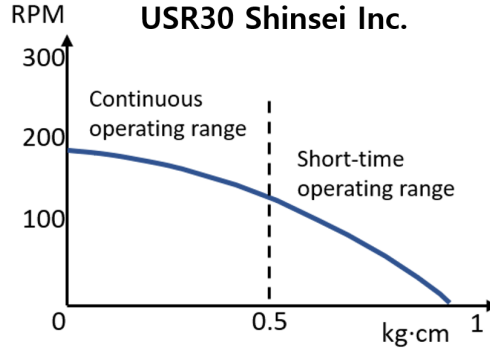
Figure 4.8: Shinsei motor torque-speed characteristic.

Rotary potentiometers (Panasonic EVW-AE4001B14) were added to the motor shafts to close the position control loop. The signal to noise ratio of the potentiometer is 1:0.001 and its average noise amplitude is 0.3°, which corresponds to a $0.043\,\mathrm{mm}$ displacement resolution.

The ultrasonic motor is not back-drivable [73] and this is often undesirable for haptic devices, which are usually impedance-type devices with low inertia and gear ratio. Our actuators are closer to those used in admittance-type devices, which require force sensing to function. In the present case we did not have a force input for the admittance display

but we used the motors to create displacements to deform the finger pads. The pressure cues created by the displacements were proportional to forces sensed at the needle tip.

A drawback of ultrasonic motors is the presence of a velocity deadband [74, 75], which hinders smooth position control, especially at low speeds and small displacements. Various methods have been developed to compensate for this deadband, including a differential gear system using two ultrasonic motors to control one degree of freedom [76], fuzzy control schemes [77], and neural networks [78]. However, we chose a simpler approach that is adequate for this position-controlled implementation. The approach involves shifting the deadband velocity from a nonzero magnitude to zero by tuning the motor velocity range setting on the Shinsei motor driver. Then, by applying a threshold voltage to the input of the ultrasonic motors, we are able to achieve a relatively linear, controllable speed (Figure 4.9). Closed-loop position control results with the flexure in place are seen in Figure 4.10 for a smooth 0.5 Hz sine wave.
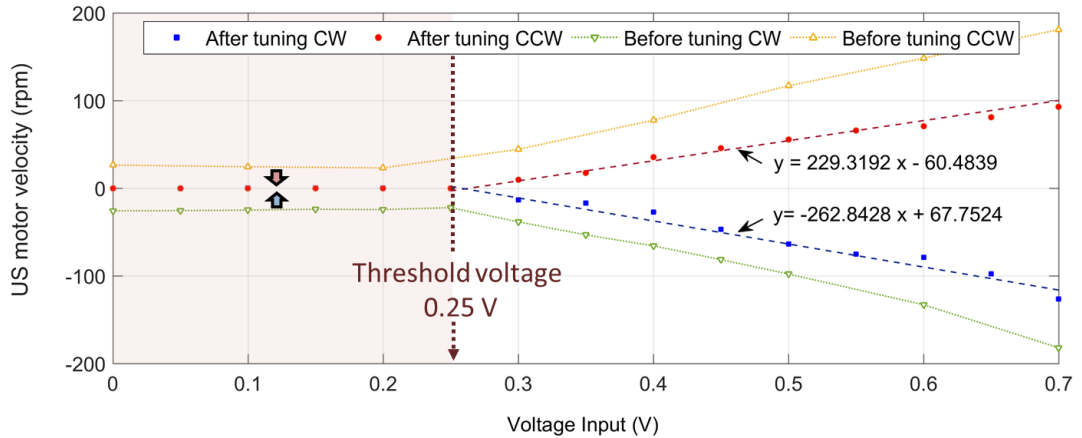
Figure 4.9: Ultrasonic motor speed characterization. After tuning the ultrasonic motor driver, the deadband velocity becomes zero over a voltage range of 0-0.25V.

As noted earlier, useful haptic information ranges from approx 0-400 Hz. However, the focus in this implementation is to provide directional cues at relatively low frequency. This is because higher frequency information tends to lose its directional information as it becomes vibratory (normal skin deformation can be felt from 0-30 Hz; directional skin stretch is felt from 0-15 Hz [79]). Vibration could also be added later with an additional actuator in order to complement the directional feedback [80]. We tested the frequency response of the ultrasonic motor flexure system for a series of commanded sine waves to determine its
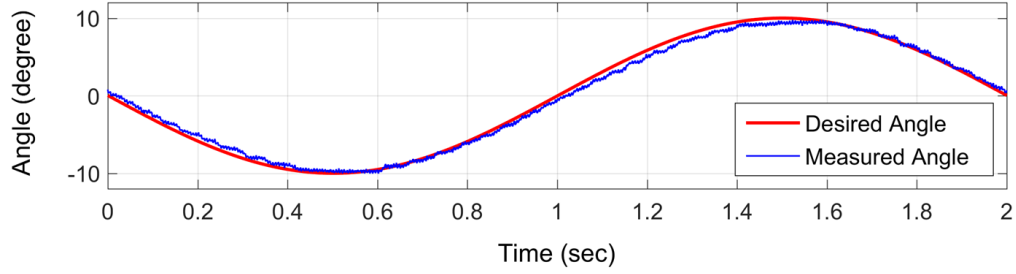
Figure 4.10: Motor position control result after adjusting velocity deadband with flexure in place.

frequency capabilities. The resulting bandwidth for an input amplitude of approximately $10°$ is 22.5 Hz, as shown in Figure 4.11.

Force amplitude and direction information read from the tip of the needle are linearly mapped to the displacement of the knob, x_{knob}. The following equations relate sensed forces, F_x and F_y, to the motor positions:

$$x_{knob} = F_x \kappa_{fd} \tag{4.1}$$

$$y_{knob} = F_y \kappa_{fd} \tag{4.2}$$

$$\theta_{Xmotor} = \theta_0 + \sin^{-1}(x_{knob}/r) \tag{4.3}$$

$$\theta_{Ymotor} = \theta_0 + \sin^{-1}(y_{knob}/r) \tag{4.4}$$

where x_{knob} and y_{knob} are the displacements of the knob in the x and y directions (Figure 4.7) respectively, θ_0 is the home position of the motor at zero displacement, and r is the
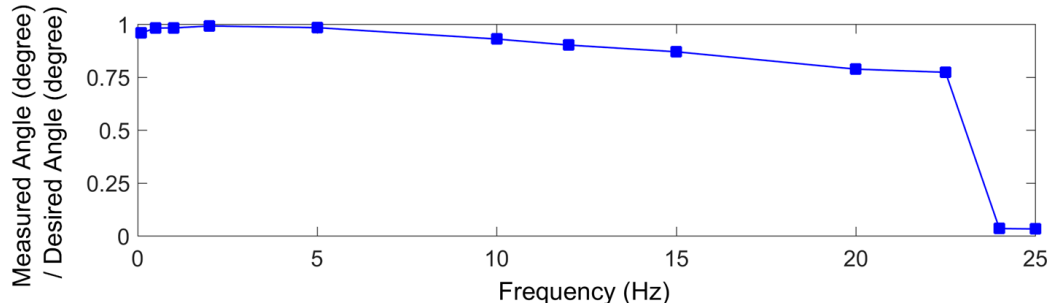
Figure 4.11: Frequency response of the ultrasonic motors after deadband velocity adjustment, measured by giving a series of $\pm 10°$ sinusoidal commands to the motors.

offset distance between the motor shaft and the pin of the scotch-yoke mechanism in the haptic device. The value of κ_{fd} was chosen based on pilot user experiments.

Subjects indicated that they had difficulty in sensing the axial forces naturally transmitted through the needle and moving platform (described in Section 4.3.1) when the lateral haptic cues were too large. Based on this observation, we decided to keep the scale factor small to conserve axial sensitivity. However, we chose a large enough value for κ_{fd} that subjects could still accurately identify the direction of displacement when feedback was provided. We obtained an initial estimate of the minimum displacement through a pilot test with five subjects. Subjects were able to identify the direction of 0.1 mm displacements with an average accuracy of 90%.

4.3 User Study

4.3.1 Test Setup

Moving Platform

For targeting tests, the needle and haptic display were mounted to a freely moving platform that rolled on ball bearings. The platform is a planar analog to a passive teleoperation system for manipulating a needle (e.g. [67]). It permits forces on the needle to be transmitted directly to the user (especially axial forces, as the needle is much stiffer in compression than in bending), but with some masking due to inertia and a small amount of friction.

To simulate the compliance of the passive teleoperation system, we attenuate the direct radial force transmission by locating the user's hand and the needle at two different locations of the moving platform. The needle was mounted to the first layer of the moving platform. The haptic device and the hand of user were located on the second layer of the platform (Figure 4.12). Two ball bearing plates (shown in right side of Figure 4.12) allowed the platform to move freely in the plane. To steer the force sensing needle for user study, the user translates and rotates the moving platform in the plane.

4.3.2 System Integration

As described in Chapter 3, the wavelength of reflected light from FBGs shifts in proportion to strains at the tip of the needle. To compute forces and transmit them, a control and communication system is required. This system has to retrieve wavelength data from the
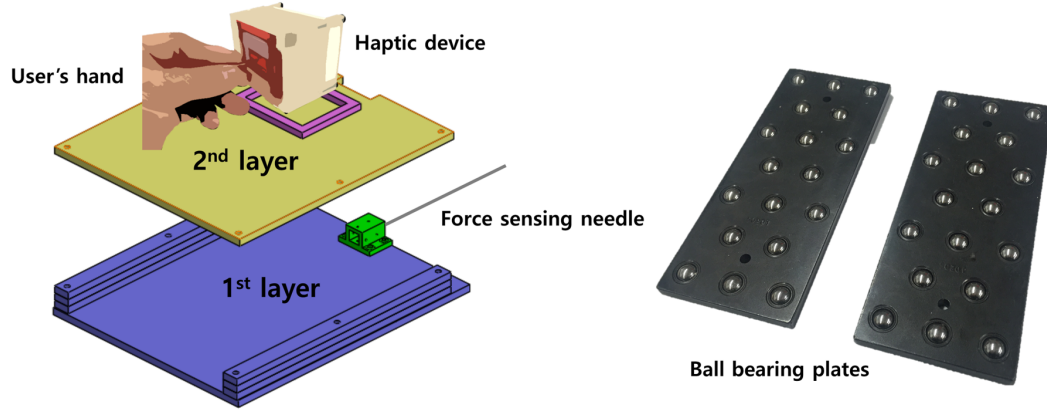
Figure 4.12: Configuration of the moving platform. Two ball bearing plates were used to make the platform freely movable in the plane.

optical interrogator through TCP/IP communication and create the necessary output for the ultrasonic motor drivers. The information flow of this control/communication system for haptic feedback is shown in Figure 4.13.

Close integration is important because axial forces are also being transmitted directly along the needle shaft. Delays between an event and the corresponding haptic stimulus become noticeable when they are larger than 45 ms [81,82]. Minimizing the delay is important in our system to prevent the displayed radial forces from apparently lagging the directly transmitted axial forces.

The control/communication system consists of two ethernet boards; one for reading the interrogator (tip-force sensing data) and another dedicated to a Linux based EtherCAT
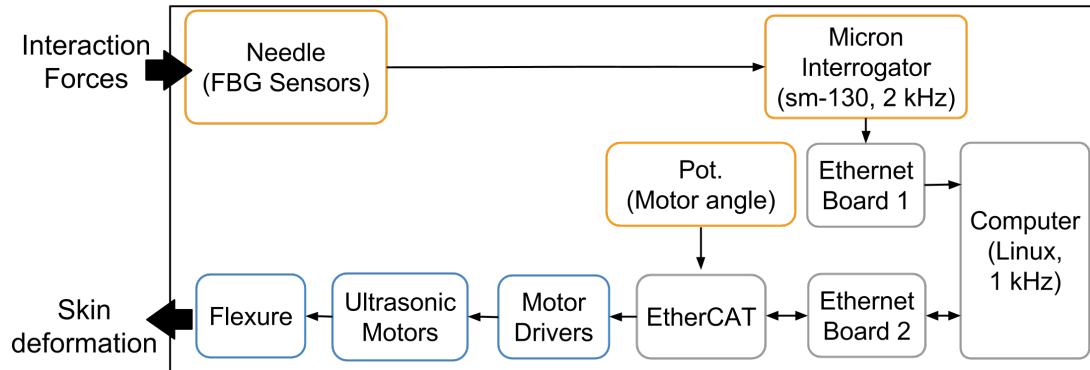
Figure 4.13: Haptic device system information flow schematic
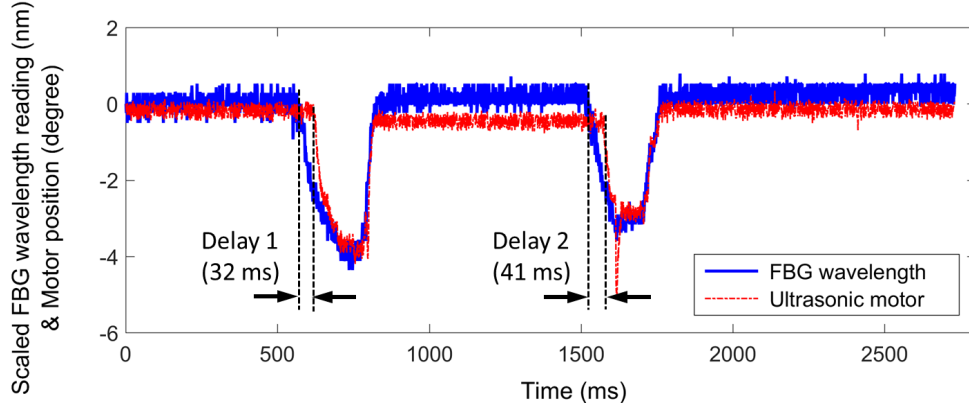
Figure 4.14: Haptic device system delay between FBS sensor data at the needle tip and position data of the ultrasonic motor. Average delay was 36ms.

system used for controlling the motors. By setting the execution priorities in a C++ program, we were able to build a "soft realtime" system. To minimize the delay from the interrogator, we used an unbuffered data collection function from the sm-130 interrogator API (Micron Optics Inc., Atlanta, GA, USA) to read wavelength data. We then calculated the lateral forces using a calibration matrix. The forces are linearly mapped to the desired displacements, which are further mapped to the corresponding motor angles. The EtherCAT analog input module measures the motor positions by reading the analog voltage level of potentiometers. A proportional-integral controller is used to achieve the desired motor positions. The average latency between the sensed strain data and the position feedback output was measured for a 1 kHz acquisition speed, and was found to be approximately 36 ms, which is within our desired range. Figure 4.14 shows the delay between sensing and actuation as the needle tip is tapped twice from the right.

Tissue Phantom Preparation

Based on our observations and interviews from physicians, the target (Figure 4.15 (C)) is designed to simulate a prostate, including the outer membrane. It consists of a rotating cylinder covered with a thin layer of ripstop nylon tape. Unless the tip of the needle is aligned with the central axis of the target, the cylinder rotates away, evading puncture. While two small ball bearings held the shaft of cylinder, a small rotary damper prevents the cylinder from spinning too freely. A torsional spring (0.43 Nm/rad) was added to restore the cylinder to its equilibrium orientation. Although an actual prostate can both translate
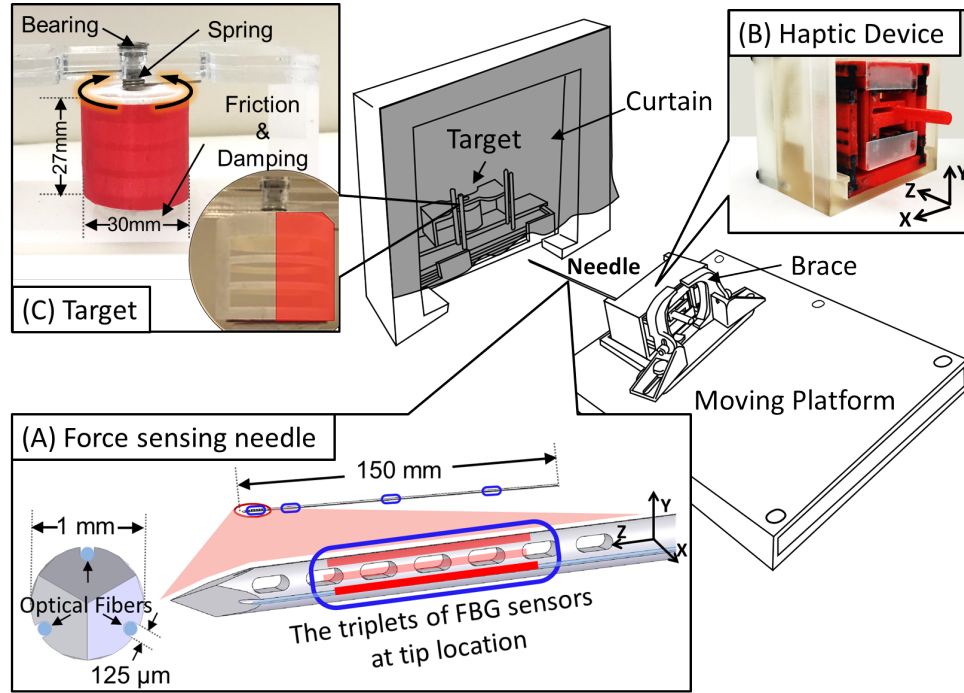
Figure 4.15: Experiment setup consists of a needle instrumented with optical fibers (A) and a pen-like haptic device (B) mounted on a 3-DOF rolling platform. Users manipulate the platform and needle with the goal of puncturing a target (C) occluded by a curtain. The target rotates, evading puncture, if the needle is not accurately aligned.

and rotate [83,84], the current setup was judged by physicians to present an equivalent level of difficulty for membrane puncture.

In front of the target cylinder, a layer of "extra firm" tofu (bean curd) simulated the effect of soft intervening tissue [85], which the needle had to traverse on its way to the target. The tofu and the cylinder's ripstop tape were replaced frequently. A curtain was placed just above the plane of the needle to conceal the target

4.3.3 User Study Design

In order to test the potential for an augmented directional feedback system, we designed a task that simulates a prostate biopsy to improve surgical procedures. Ten subjects were each instructed to puncture a prostate phantom 20 separate times by steering the moving platform and needle with their hands.

In operation, a user grasps the haptic display with the thumb and index finger while
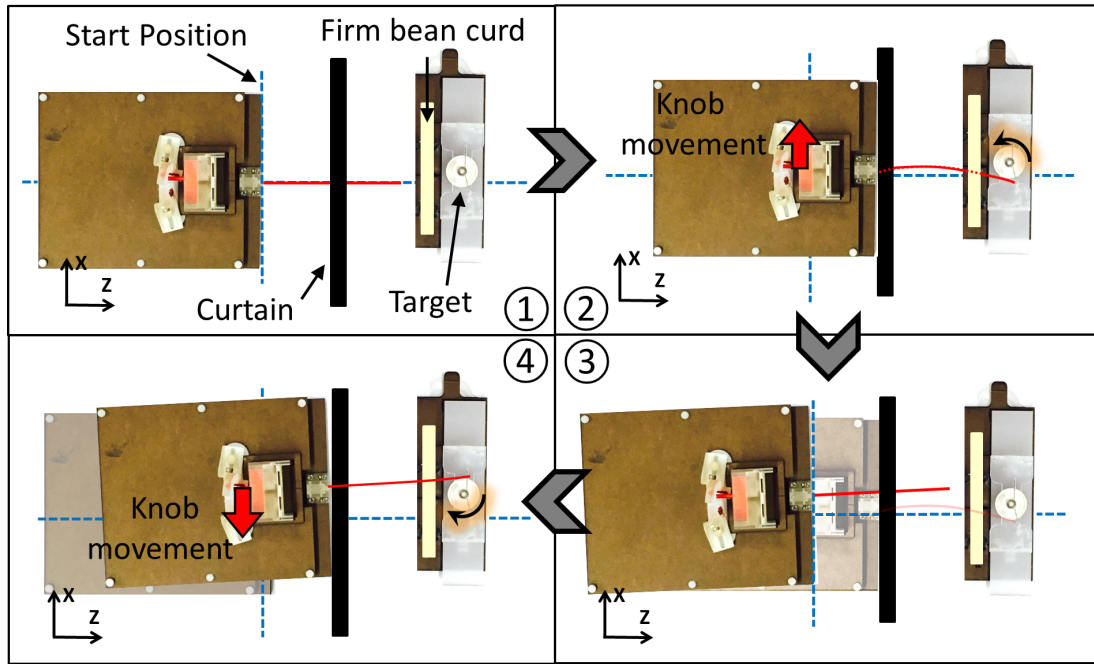
Figure 4.16: Typical starting sequence: (1) initial position; (2) first attempt to penetrate the target (needle deflects in $-x$ direction, feedback applied in opposite direction); (3) user retracted needle and reorients; (4) second attempt results in needle deflected in $+x$ direction with feedback in $-x$ direction.

resting his or her hand upon the platform. The hand pushes the platform, guiding the needle into contact with the target. When interaction forces are detected at the tip of the needle, the haptic display presses upon the user's fingertips providing additional feedback.

As noted in the previous section, a curtain hides the target from view. The target was randomly positioned $\pm 6\,\text{cm}$ to the left of right for each trial so that the needle was never aligned perfectly with the target and its position was not predictable. The intervening tissue phantom (extra firm tofu) was replaced after each attempt, and the membrane was replaced between trials so that repeated punctures would not reduce the difficulty of the task over time. Half of the trials were provided with augmented haptic feedback, while the other half were not. To simplify the experiment, forces were only sensed and displayed in the x direction, as shown in Figure 4.16. Due to the cylindrical shape of the target, forces in the y direction were not particularly useful.

The haptic feedback displayed to the subject was opposite to the direction that the target deflects the needle and proportional to the needle deflection. As a result, it directs

the subject toward the center of the cylinder.

Subjects were instructed to view the feedback as directional guidance information. Figure 4.16 illustrates a typical starting sequence: (1) the subject pushes the needle forward, but the needle is not aligned with the target center; (2) the needle deflects in the $-x$ direction so that haptic feedback is applied in the $+x$ direction; (3) the subject corrects by tilting the needle and tries again; (4) the subject has over-corrected so that the needle now deflects in the $+x$ direction and feedback is applied in the $-x$ direction.

For each trial, a subject was allowed ten attempts to puncture, with each attempt consisting of driving the needle toward the target and then removing it. After each attempt, the following information was verbally collected from the subject: (i) whether they believe they punctured the membrane of the target, (ii) whether they thought the needle was to the left or right of the target center, and (iii) whether they were confident of each of the previous two answers. Between attempts, the subjects were instructed to make lateral position corrections based on the previous attempt to align the needle with the center of the target as well as they could. All tests were conducted in accord with Stanford IRB Protocol 26526.

4.4 Results

Experiments were conducted with 10 subjects, (8 male, 2 female) with ages ranging from 23 to 29. Among these, 4 had experience in haptics and none had prior experience in needle procedures. Of the 20 puncture trials (maximum 10 attempts to puncture for each trial) required of each subject, the average number of attempts to puncture in the case of no added feedback was 4.75 with a standard deviation of 1.32, while the average with feedback was 3.13, with a standard deviation of 0.53, as seen in Figure 4.17. We performed a one-tailed paired t-test with the following null hypothesis: (*average number of attempts without feedback - with feedback*)>0. The result shows a statistically significant difference (p-value= 0.0028).

Another metric for performance of the device was how accurate the subjects were at determining where the needle tip was with respect to the target (Figure 4.17 (B)). With directional feedback, subjects reported the correct needle location 61.8% of the time with a variance of 0.03 (3%). Without the additional feedback, subjects were correct 46.8% of the time with a variance of 0.012 (1.2%). A one tail paired t-test shows a statistically
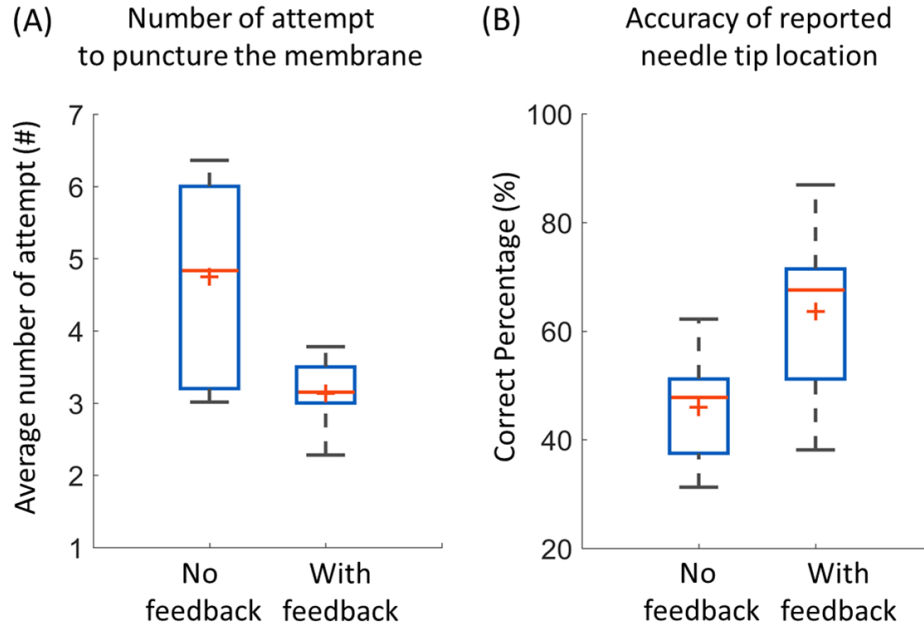
Figure 4.17: (A) Number of attempts before puncturing the target membrane. (B) Accuracy of subject-reported needle tip location with respect to the target. Boxes represent 25-75% of data, + mark is the median, line is the average. Whiskers show data between 10-90%.

significant difference (p-value= 0.0041). There were large differences between subjects in terms of how well they utilized the feedback, with one subject achieving 93% accuracy at direction determination, while the lowest accuracy was 30%.

4.5 Discussion

Results of the targeting test indicate that directional fingertip haptic feedback successfully reduced the number of attempts needed to puncture a membrane on a movable target and the performance was more consistent (smaller variation). The direction identification accuracy improved greatly for some subjects, while others did not improve, showing that the device worked well for some, but not all, subjects.

In general, puncturing the nylon membrane was challenging because it required significant axial force and the cylinder rotated easily if the needle was off-center. However, subject performance improved rapidly, showing that a significant training effect existed. Randomizing the trials was therefore important. Our haptic feedback device did not augment axial

force or provide high frequency feedback associated with puncturing membranes, both of which could have made the task easier. However, the focus of the task was to test how well lateral force feedback can help users locate the best place to puncture, as opposed to how well they could actually execute the puncture. The metrics show that the feedback helped users locate the center of the prostate phantom.

One interesting issue raised during the pilot phase of this experiment was whether users preferred feedback in the same direction as the tip load or in the opposite direction. Our initial thought was to provide feedback in the same direction, thinking that it should feel as if the subject's fingers are at the tip of the needle and experiencing exactly the same forces. However, when we tested this style of feedback, the results were not uniform. Some subjects understood the feedback well, while others became confused or always responded in the opposite way from what was expected. This result may arise from users perceiving the haptic feedback as corresponding to a reaction force felt at the base of the needle instead of the contact force at the tip. To sidestep these issues and improve consistency, we decided to adopt the convention that the feedback is a guidance force pointing toward the ideal puncture location based on sensing data – a simpler concept to grasp.

4.6 Conclusion

Subjects could easily determine the direction in which haptic feedback was guiding them, and the guidance improved their task performance. The puncturing element of the task might have been easier if the haptic device also provided augmented axial feedback to the subjects, which could be a useful addition for future experiments. Adding a third degree of freedom should further increase realism and allow for experiments using biological phantoms with more complicated geometries.

Another reasonable modification would be to replace the ultrasonic motors with actuators that have lower impedance, so that we can truly transmit dynamic forces instead of displacements. This may increase the intuitiveness of the feedback and perhaps reduce some of the confusion that arose when subjects were told to interpret the feedback as a force felt at the needle tip. As discussed in Chapter 5, electroactive polymer artificial muscles show promise as a way to achieve true impedance control while keeping the device MR-compatible.

Finally, a high frequency actuator (e.g. as in [86]) could be added to complement the low

frequency skin deformation. This would likely enhance the perception of puncture events, texture of tissue, and impacts.

Chapter 5

Axial Force Display

During needle insertion, axial forces provide information associated with membrane contact and penetration, and corresponding tissue mechanical properties such as stiffness and texture. In this chapter, we focus on membrane contact detection and sensing of the instant of puncture based on the axial forces measured at the needle tip.

Knowing the moments of membrane contact and puncture is useful in performing many needle procedures. For example, in portal vein bypass surgery, which is often performed to solve the blood circulation problem of cirrhotic liver, a needle or catheter is used to create a channel between the hepatic vein and the portal vein. The ideal way to connect these two veins is to puncture only one side of the portal vein and connect the puncture to the hepatic vein. If the needle punctures through both sides of the wall, blood leaking from the second puncture can cause complications. Another example is prostate needle intervention. The prostate is located very close to the urinary bladder and if this is punctured it can cause serious infection problems. Thus knowing the moment when the needle traverses the prostate capsule and enter the gland is helpful for the user to stop insertion right away and avoid bladder. If doctors are better informed about needle axial forces during procedures, they may be able to prevent possible complications or problems due to undesired membrane puncture. Furthermore, they will likely be able to locate the needle tip more precisely within a small target (e.g. blood vessels) since they know when the needle enters the target.

5.1   Preliminary User Study - Voice Coil

In this section, we demonstrate the use of axial force feedback in preliminary bench-top experiments. A voice coil actuator was used to display the measured axial force at the tip of the force sensing needle in order to ascertain the utility of a tip-force sensing needle over a traditional 6-axis force-torque sensor mounted externally at the base of the needle. Although the haptic display was not MR-compatible, this preliminary test shows the benefit of reading axial force with minimum effect of friction, which could mask small changes in axial forces [33]. This section describes the results of controlled membrane puncture detection tests in which subjects received haptic feedback dependent on either the needle tip-force (FBG sensors) or the force as measured from the the needle base (commercial force/torque sensor) in order to detect membranes embedded in tissue phantoms. As a reference, the baseline case in which subjects received no added feedback was included in the test.

5.1.1   Test Setup

Phantom Materials for Physiological Tactility

We first investigated which materials best mimic human tissue for bench-top testing of our force sensing needle. Two types of phantom tissues were made based on materials used in the literature [8,87,88]. Phantom tissue materials included 2:1 and 4:1 ratios of PVC plastic to softener (Plastisol, M-F Manufacturing Co, Fort Worth, TX) and agar. Membranes made of polypropylene and polyester films were placed between blocks of phantom tissue as shown in Fig 5.1.

To evaluate the phantoms we interviewed doctors in the Diagnostic Radiology department at the Stanford Medical Center. Four physicians with an average of 24 years of experience since residency, and one fellow, were given the sample phantoms and a biopsy needle, and then asked to describe the feeling during insertion by hand.

One interventional radiologist described the agar phantom as what he's used to feeling for normal tissue, whereas the PVC phantom felt more like a breast tumor. Another senior physician said the agar feels like fat, normal liver and normal tissue, whereas the 2:1 PVC phantom felt like a "more convincing" real tumor. Next, a phantom was prepared with alternating agar and PVC blocks, with polypropylene film between the layers. One doctor feeling this phantom said the PVC with membranes felt realistic for going through a

membrane, however the phantom had a lot of resistance. Going from agar to the membrane felt like hitting a calcified lesion. The PVC felt like breast tissue, the agar felt like fat, and a cyst would feel like the membrane against agar.
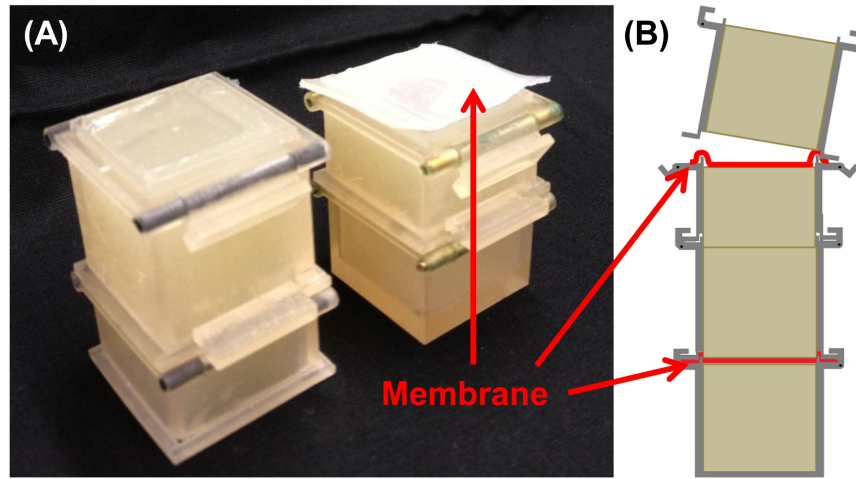
Figure 5.1: Reconfigurable membrane and tissue phantom (A) photo and (B) assembly diagram.

With the multi-material phantom (agar, membrane, PVC, membrane, agar), we covered the phantom and gave the physicians a task: to stop insertion when they think they have reached the 2nd membrane. One physician said it was difficult to feel the 2nd membrane, yet was successful in all trials. The physician also commented that drag is felt when the needle gets into the second agar layer. Another physician said this task "feels like thyroid biopsy," in which the fascia layer where anesthesia is delivered can be felt. He was also successful in feeling each membrane and commented on the resistance through the PVC layer. Drawing from experience in real procedures, he said, "The deeper you go, the less sensitive your fingers are. In the liver, once the needle is 5 to 7 cm in, it gets difficult to feel anything." Physicians expressed desire for haptic feedback and said that after years of doing biopsies, "You learn to trust your feel as much as your eyes."

Overall, it was decided that agar better mimicked healthy soft tissue, and the PVC phantoms mimicked tumors and tougher tissue, yet caused significant drag and high frictional forces along the needle during insertion.

Needle Insertion System and Haptic Device

A single degree of freedom (1-DOF) needle insertion system was designed as shown in Figure 5.2. To restrain the movement of the system in 1-DOF, a rail and two carriages (DryLin T TW-01-15, Igus Inc., Kln, Germany) were used. On the first carriage, an external 6-axis force/torque sensor (Nano 17, ATI Industrial Automation, Apex, NC) and the force sensing needle described in the Chapter 3 were mounted; this represents the slave side of an ideal 1-DOF teleoperation system. The master side consists of a voice-coil haptic display which displays the dynamic force information read from either the base of the needle (using the ATI force/torque sensor) or from the tip of the needle (using the tip FBGs). A block of PVC rubber (Plastisol in 2:1 plastic:softener ratio) was used to isolate the master from vibrations in the slave during needle insertion – as would be the case when using an electromechanical master/slave system. However, the compliant master/slave coupling does transmit large, low-frequency forces, freeing the voice coil actuator to produce vibrations instead of kinesthetic forces. Thus, the 1-DOF master/slave system with its
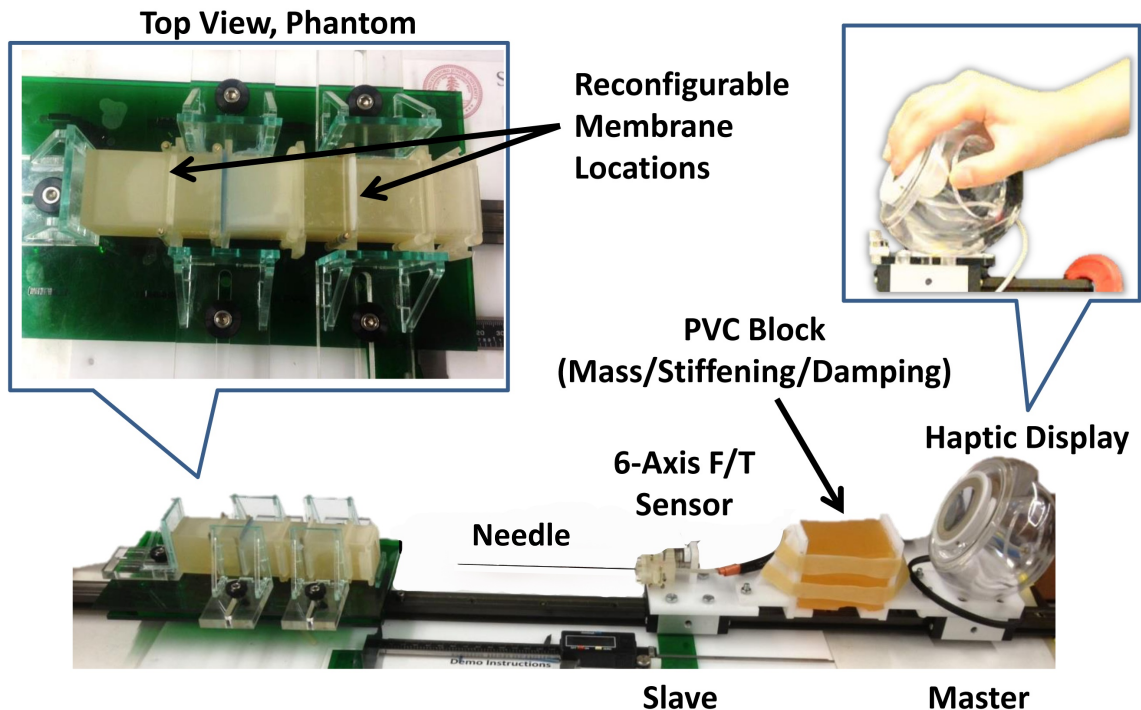
Figure 5.2: Master/slave system restricting insertion motions along the axial direction, with haptic display as used in the benchtop experiments.

damped, compliant coupling and the voice-coil haptic display together provide a simulation of the feeling to be expected from an electromechanical master/slave system augmented with vibrational haptic feedback.

To test the isolation of the master and slave platforms, two accelerometers were attached to the master and slave side, and the slave side was struck by hammer several times. The set up was the same as for the haptic experiments, with the damping block placed between the master and slave such as in Figure 5.2. The average cutoff frequency of the block from 6 trials was 17.7 Hz. The frequency response data from a test is shown in Figure 5.3.

Haptic feedback was given based on the tip FBG sensors or the ATI force/torque sensor at the needle base. There is some baseline noise in both the FBG and force/torque sensor measurements. The FBG sensor system had a noise level equivalent to 0.07 N at the master display; the force/torque sensor had a noise level equivalent to 0.16 N. This noise would produce noticeable displacements at the haptic display if played directly. Therefore the baseline noise is filtered for both the force/torque and FBG data using a point by point median filter. The window of the median filter is minimized such that the hardware execution loop can run at 1 to 2 kHz, which minimizes any latency in forces felt by the user.

Due to the water evaporation from the agar phantom, there was a temperature difference between the top and bottom of the phantom (around 3 ℃). Since the FBG readings are sensitive to temperature, a secondary point by point mean filter is applied to the wavelength data. This low pass filter gathers data for 800 samples and establishes a baseline to track thermal drift, which is subtracted from the original data. The mean filter does not affect the speed of the haptic system, but is used as a comparison for the current wavelength shifts which, if above a certain threshold, are considered to be due to physical contact and not
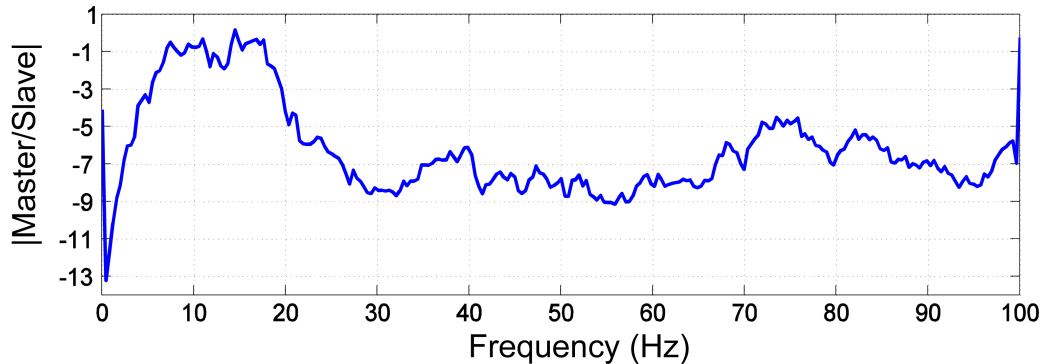
Figure 5.3: Frequency response of the PVC damping block from a test.

temperature change. In this way, the mean filter acts as a low pass frequency filter and is used to measure slow changes in the FBG data and reduce effects of temperature.

We used an sbRIO (Model 9632, National Instruments Corp., Austin, TX) data acquisition board; an Ethernet switch from the optical interrogator, control computer and sbRIO; and custom software written in LabView to drive the haptic display. While the needle tip is loaded, either the filtered reading from the sensor most sensitive to axial loading (FBG number 10, which lies on top of the slotted holes) or from a voltage output from the external force/torque sensor, is used to drive the voice coil actuator. The voice coil is controlled by a linear current amplifier which receives an analog voltage from the sbRIO. Gains on the sensor data are set such that the voice coil actuator produces the same displacement for the same load as measured by the base ATI sensor and the tip FBG sensors. Figure 5.4 shows how the force information from the ATI and the force sensing needle was displayed to the user during the user study.
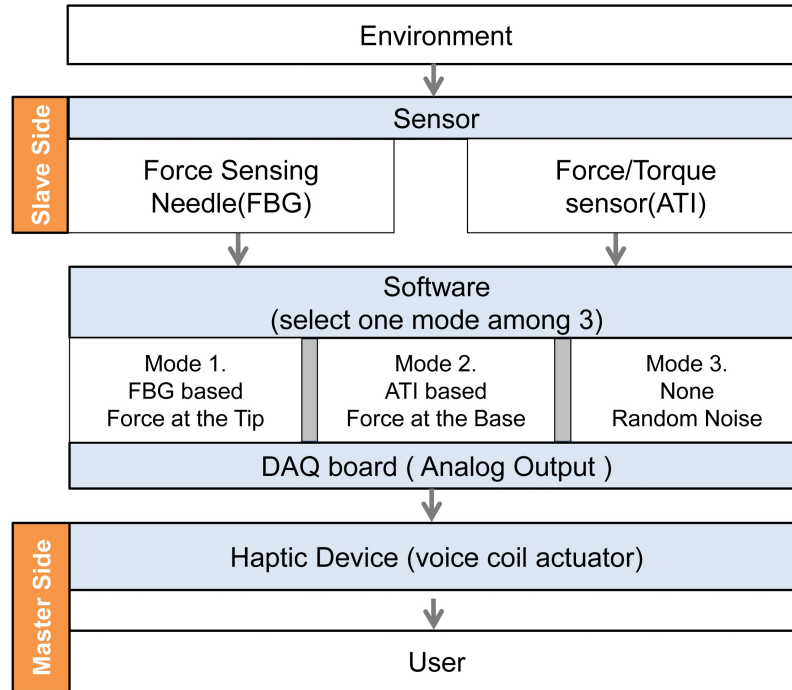
Figure 5.4: Schematic of mechanical and software parts of haptic feedback system. The software part randomly selected one haptic mode at a time during the user study.

5.1.2 User Study Design

The experiments required users to insert the needle via a mechanically coupled master/slave system into an agar phantom with membranes placed at different locations. Users pushed from their palms on the haptic display to insert the needle into the tissue phantom. While inserting the needle, they felt the displacement from the front face of the haptic device through their fingertips (Figure 5.2). They were asked to stop insertion when they felt they encountered a membrane. The membranes were made of Shore 2A durometer silicone (Dragon Skin FX-Pro, Smooth On Inc, Easton, PA), cast inside molds 0.1-0.3 mm thick with embedded tissue paper (34155, Kimwipes, Kimberly-Clark, Irving, TX) to mimic the connective tissue layer in natural visceral membranes. Trials were randomized in the position of the membrane along the phantom, and whether or not the subject received haptic feedback. In the no-feedback case, a small amount of white noise, indistinguishable from the noise encountered with the FBG and external force/torque sensors, was played to the voice-coil. The insertion distance was measured via a fixed digital caliper along the 1-DOF stage. The membrane could be placed anywhere from 2 to 10 cm along the agar block. The subject was asked to stop insertion when they believed they encountered a membrane; then the insertion distance was recorded.

5.1.3 Results

Of 87 insertions by 10 healthy subjects, the success rate of identifying a membrane encounter was 47.5% with feedback from the needle's FBG tip sensors, 25.8% from the external force/sensor (ATI) at the needle base, and 13.3% in the case of no haptic feedback. The test subjects were healthy, approximately half male and female, and with an average age of 28.5 years; however, they were not physicians experienced in needle biopsies.

A success was characterized as stopping the needle tip within 18 mm of the actual membrane location. This distance threshold was set because first contact, where forces are still low, can occur a large distance before puncture does. The membrane stretches and deforms significantly before it is pierced, at which point the needle tip will experience the greatest change in force. Furthermore, after trying the experiment protocol in a 3-D cone beam CT scanner (Siemens Zeego), we noticed that even though an obvious membrane puncture was detected, it was difficult to stop the stage within a centimeter past the membrane. Based on various trials and measurements between the needle tip and membrane as seen in the

Table 5.1: Percent of Total Failures per Feedback Method

	FBG	ATI	None
Success rate	47.5%	25.8%	13.3%
Missing a membrane	32.5%	38.7%	33.4%
Did not feel anything	5.0%	22.6%	33.4%
Sensing a non-existent membrane	10.0%	9.6%	13.4%
Stopped too early	5.0%	3.3%	6.7%

CT images, we set the success threshold to 18 mm.

Paired t-test calculations were used to compare the success rate among the subjects for two modes against the FBG sensors: the no haptic feedback mode and the force/torque mode that senses the forces at the base of needle. From a one-tailed test as to whether FBG feedback was better than ATI feedback, there was a statistically significant difference between two modes (mean success FBG - ATI = 0.255, within a 95% confidence internal, t = 1.896, p-value = 0.045). However, when comparing the success rate of the ATI based mode versus no haptic feedback, there was no significant difference (mean success ATI - No feedback = 0.264, within a 95% confidence internal, t = 1.54, p-value = 0.079). FBG compared to no feedback was very significant (mean success FBG - No feedback = 0.519, within a 95% confidence internal, t = 3.71, p-value = 0.0024). These results suggest that the FBG tip sensing mode helps subjects to detect the membrane more successfully than the other two modes.

Reasons for failure in all cases included when a user "Did not feel anything," meaning he/she moved the stage through the entire phantom without detecting a membrane, and "Missing a membrane," meaning that he/she felt the membrane after puncturing it. "Sensing a non-existent membrane" was a false positive error.

The FBG based feedback had only two failures with "Did not feel anything", whereas the base force/torque sensor and no feedback cases had seven and five failures of this type respectively. The majority of FBG based feedback failures (32.5%) were due to the subject just passing the membranes ("Missing a membrane"). In the cases of just "Missing a membrane", the average distance between the needle tip and the threshold after stopping was 6.7 mm for the cases with FBG feedback, 17.5 mm for the external sensor, and 8.7 mm for no feedback. Therefore, users were closer to stopping just after the membrane in the

cases in which feedback was based on the FBG sensors over the other cases.

5.1.4   Discussion

It is difficult to apply pure axial loads to the needle, and the sensitivity of the needle is considerably higher for radial loads than axial loads. Hence, even when inserting the needle with a single degree of freedom apparatus, it is likely that small radial loads at the needle tip are a substantial fraction of the measured tip force. In practice, this may not be particularly important as membrane puncture and other needle/tissue interactions are often accompanied by a combination of axial and radial dynamic forces. Moreover, for forces with frequencies in the tens of Hz and up to a few hundred Hz, the dominant human sensing mechanism is likely to be the Pacinian corpuscles, which have large receptive fields and are not particularly directional [38].

Although small changes in temperature can produce strains comparable to those of forces at the needle tip, it was possible to minimize these effects by using dynamic forces during calibration, and by high-pass filtering during insertions. In particular, it was found that a secondary filter was helpful in eliminating error in the FBG sensor force readings due to gradual temperature change when the tip moved inside of the agar block; however some variation like the sudden temperature variation from air to agar was still present, which could be mistaken for a membrane puncture. Therefore, in the haptic experiments, we made the starting position of the needle tip in each trial be just inside the agar block such that there would not be a noticeable change due to temperature during insertion.

It was also observed that due to the secondary filtering, if the stage was moved too slowly, it was difficult to pick up a significant change in applied load. It may be that the secondary filter and threshold parameters need to be adjusted to better remove effects of temperature while allowing for detection of higher frequency changes in axial load during membrane deformation and puncture. In addition, human haptic perception is better at detecting fast changes than slow changes in forces.

Some subjects discovered that dithering the stage (moving the stage gently back and forth with small quick motions) made it easier to feel the membranes. Dithering is a human strategy that helps us to detect small force changes. [89] It also takes advantage of a reduction in system friction, because the dynamic coefficient of friction is usually less than the static coefficient.

5.1.5 Conclusions

Tip forces can easily be discerned by the sensorized needle, especially above 0.05 N, when changes due to temperature are filtered out. Future methods to improve axial and temperature calibration may include the use of dual period FBGs or the use of full spectrum FBG data. Other feasible approaches to measure force and temperature independently include bilateral cantilever beams [90], the use of the bifringence effect [91], and hybrid dual-grating sensors [92].

Although the haptic feedback test results presented here used a haptic display which is not MR compatible, and recruited non-experts as subjects, it was shown that the FBG embedded needle helps significantly (p<0.05) in identifying needle tip contact with a membrane in a tissue phantom. Experts in needle driven procedures may be more conscious of loading at the needle, even through the 1-DOF master/slave mechanism. Future work includes running these tests with clinicians as subjects, in a more clinical setting.

5.2 MR-compatible EAP haptic device

The previous section covered a preliminary user study result with a voice coil haptic display. Although the device was not MR-compatible, the user study showed the benefit of having haptic feedback based on the force sensing needle in membrane detection, especially for the teleoperated needle intervention (Figure 5.5). This section presents the design of an MR-compatible haptic display that can be used for needle interventions.

5.2.1 Electroactive Polymer (EAP) Actuator

Various methods of actuation are possible for display. Ultrasonic piezoelectric motors can be designed with non-ferromagnetic materials and low electric currents, which allow them to be MR-compatible [93–95]. However, they are inherently best suited as position-display devices as they are not back-drivable.

Electrostatic motors are another admittance-type option [96]. Additional possibilities include pneumatic or cable-driven systems [97–100], although these systems inevitably introduce some compliance and friction, especially if interaction forces must be transmitted through the entire system from slave to master. If electromagnetic motors are used, they require extensive shielding, even if located some distance from the bore [100]. Reviews of various MR-compatible actuators are available in [101, 102].
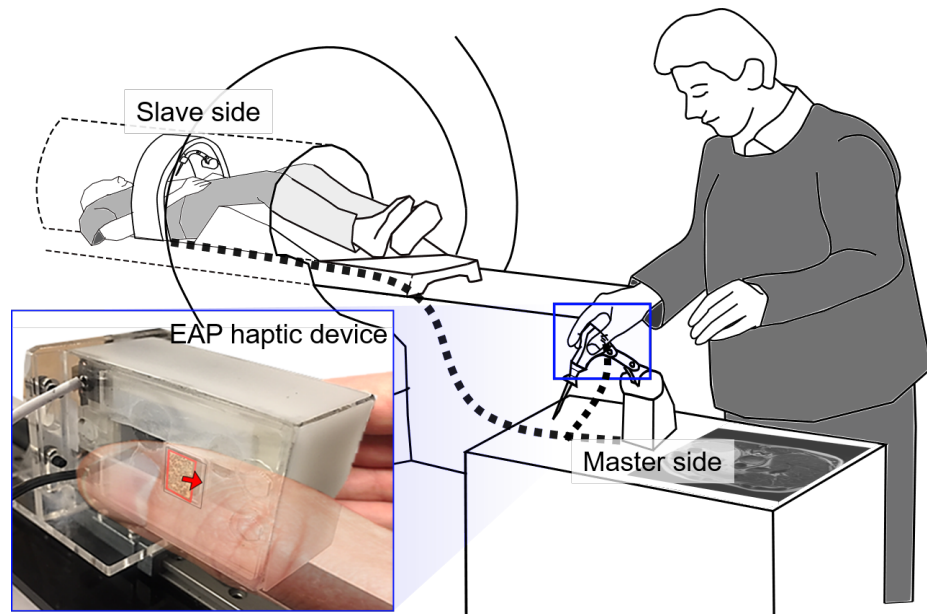
Figure 5.5: A haptic display can relay tool tip forces to a physician performing MR-guided procedures. Inset: detail of display held between thumb and index finger.

EAPs are lightweight, compliant, back-drivable and inherently MR-compatible with no metallic components and electrical currents on the order of microamps. Although they are compliant, they are more compact and light-weight than pneumatic and cable-driven solutions and therefore can be mounted at the manipulandum of a master device. The compliance does not substantially affect the overall dynamics of a robotic or teleoperated system if they are used only as small cutaneous displays at the user's fingertips. Other researchers have used EAPs for various haptic display applications including braille and wearable haptic interfaces [103, 104].

Additionally, EAPs have demonstrated feasibility for applications requiring MR compatibility [105–107]. As actuators, EAPs have interesting properties in between those of ultrasonic motors and voice coil actuators: they are neither primarily displacement nor force sources. Rather, they are viscoelastic springs with varying force and stiffness as a function of the applied voltage. They can be matched to the requirements of a fingertip skin deformation display, which requires modest forces and moderate frequencies.

In summary, EAP actuators are good potential candidates for an MR-compatible skin deformation display. In this section, the design and fabrication of the EAP display will be described.

EAP Design and Fabrication

The EAP is a dielectric elastomer covered with stretchable electrodes on the top and bottom surfaces. When a voltage is applied between the electrodes, the induced Maxwell stress squeezes the dielectric elastomer, which subsequently expands in the planar directions. This planar expansion of the EAP creates the displacement and force that are displayed through a skin deformation haptic device. The Maxwell stress can be represented as [108]:

$$\sigma = \epsilon_0 \epsilon_r E = \epsilon (V/t)^2 \tag{5.1}$$

where ϵ_0 is the vacuum permittivity, ϵ_r is the relative permittivity, V is the applied voltage, and t is the thickness.

To actuate the skin deformation haptic device, the elastomer is stretched over acrylic frames and approximately half of its area is covered with electrodes. The electrodes expand only in the $+x$ direction because the frames prevent motion in the y direction. Figure 5.6 (A) shows the EAP unpowered and (B) shows it actuated at $5.75\,\mathrm{kV}$.
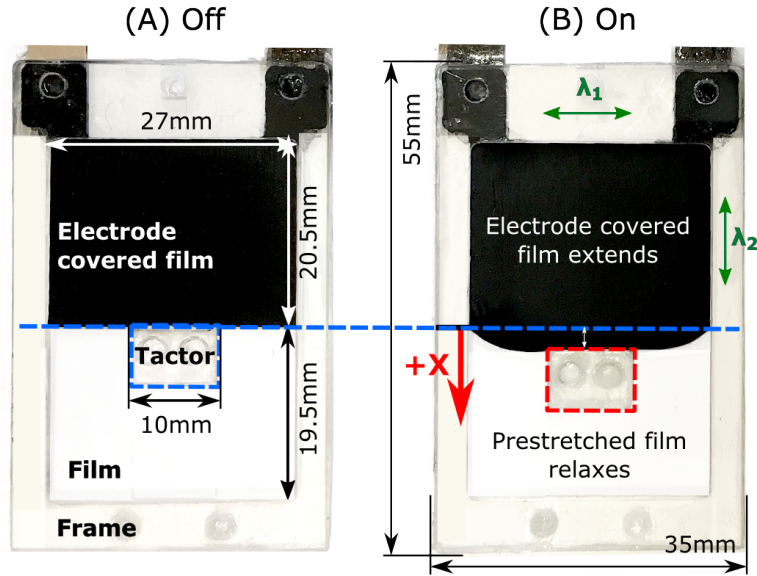
Figure 5.6: EAP before (A) and after (B) applying $5.75\,\mathrm{kV}$, which causes the film between the black electrodes to expand, producing motion in the x direction. The film prestretch directions are depicted as λ_1 and λ_2.

As with many EAP devices in the literature, we use 3M VHB 4910 acrylic film as the

dielectric elastomer. It is first prestretched to 400% by 375% in the λ_1 and λ_2 directions respectively, as indicated in Figure 5.6 (B). The prestretch ratio involves a trade-off between displacement in the x direction and maximum force as described in [17]. While the device force can be adjusted by adding additional layers of EAP actuator, the displacement of the device is predetermined by the prestretch ratio of the EAP actuator. The prestretch ratio was selected to give maximum displacement although it does not offer maximum force.

The film and frame dimensions are 35 mm x 55 mm x 2.5 mm thick, including electrodes. Masking patterns for the electrodes are laser-cut and placed on the stretched elastomer. Next, a thin layer of electrode solution is applied with a squeegee to the acrylic film (dielectric elastomer). The electrodes are made with a mixture of soft silicone rubber (Smooth-On Inc., Dragon Skin Fx-Pro Fast), carbon particles (FuelCellStore, Vulcan XC 72R), and toluene, mixed with a weight ratio of 9:1:26, respectively, following an approach described in [109]. This liquid electrode solution cures after a few hours and forms silicone rubber electrodes on the top and bottom of the elastomer. Connections to these electrodes are made with soft, conductive fiber tape.

During the manufacturing process, the prestretched area of the elastomer, the amount of electrode solution and the number of strokes to apply to the electrode solution were controlled to maintain a similar consistency. However, there is inevitably some variability between samples because the fabrication was done by hand. Each EAP layer's performance differed by up to 5%.

5.2.2   Device Layout

The primary design requirements are that the device be lightweight, compact, and able to produce displacements ranging from 0.05 - 1 mm and forces from 0.1 - 2 N, values shown to be appropriate for lateral skin stretch [69]. Six layers of EAPs were stacked to achieve the desired force levels, giving a maximum of 1.6 N blocking force (blocking force of an EAP is analogous to the stall torque of a DC motor) at 5.5 kV. We use sand paper as the tactor covering to provide adequate friction with the finger pads and minimize slipping as well as improve the communication accuracy of the device [50]. The tactor is slightly recessed with respect to the surface of the device; this configuration grounds the skin at the periphery of the tactor window, a desirable property for lateral skin stretch to maximize the skin deformation felt [50].

A modular design allows easy scaling of force as well as convenient repair of individual

EAP layers. An insulating film is placed between EAP layers to prevent arcing between electrodes. An exploded view, dimensions and weight of the device are shown in Figure 5.7.
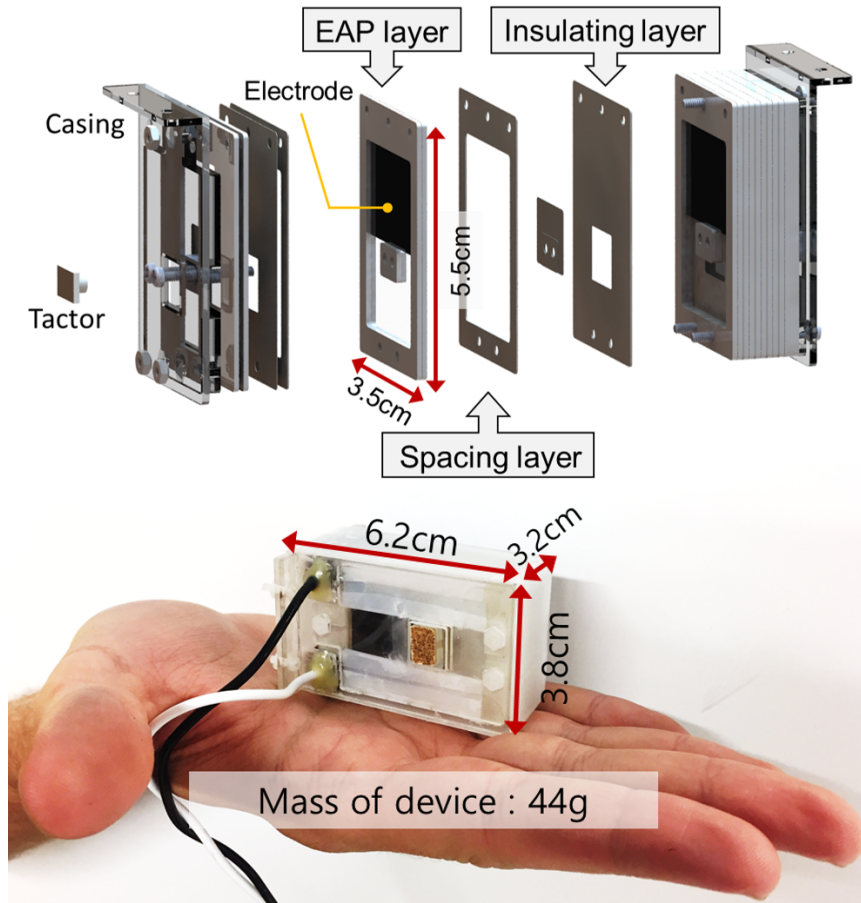
Figure 5.7: Exploded view of the haptic device showing dimensions compared to a hand. Six layers of EAP actuators are stacked to power the device. Insulating layers prevent arcing and spacing layers facilitate smooth tactor movement by preventing friction.

5.3 Device Characterization

Tests were conducted to measure the force and displacement properties of the EAP display as a function of applied voltage for a single EAP layer and for the multi-stack device shown in Figure 5.7.
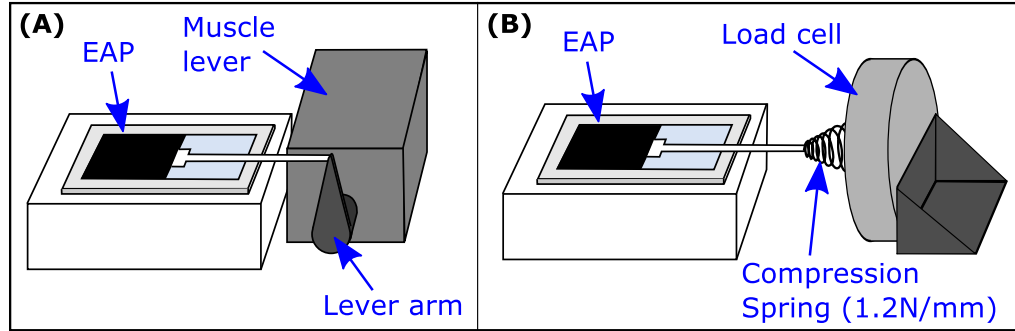
Figure 5.8: Testing apparatus. (A) EAP actuator is connected to a muscle lever for force and displacement measurements. (B) EAP is connected to a compression coil spring and a load cell for predicting the behavior when pressed against a human fingerpad.

5.3.1 Testing Setups

EAP force and displacement characterizations were performed with two setups: a muscle lever actuator (Aurora Scientific, 309C), and a load cell (ATI$^{®}$ Gamma), as shown in Figure 5.8. MathWorks Simulink$^{®}$ was used to control the voltage output of a bench-top high voltage supply (TREK, 610B). To track the displacement, we recorded video of the EAP with a machinist's ruler in the video frame for reference. Four to five trials were undertaken in each case. The noise of the ATI is ± 0.03 N and for the muscle lever is ± 0.01 N. The displacement measurement resolution is 0.1 mm.

5.3.2 Performance with a Spring

To estimate the performance of the EAP when the tactor is in contact with a user's fingertip, a coil spring was connected to the EAP as shown in Figure 5.8 (B). Its stiffness is 1.2 N/mm, which is similar to that of a lightly loaded human fingerpad in the proximal-distal direction [69].

Although it is common to report the blocking force (zero-displacement force) and free (unloaded) displacement of EAP actuators, the primary interest of this work was the performance when connected to a load having approximately the stiffness of a human fingerpad. The blocked force and free-motion results of the display are reported in [17].

Figure 5.9 shows the force-displacement performance for one, three and six layers of EAP film in the haptic device, connected to a 1.2 N/mm spring, at voltages from 0 to 5.75 kV. The voltage was reset to zero prior to each displacement test. Also shown are the
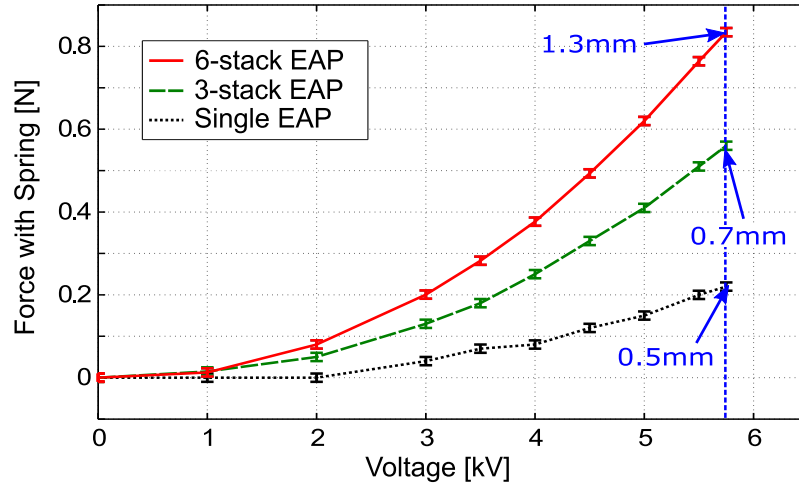
Figure 5.9: Characterization of EAPs with a spring in series. The displacement noted for each case at 5.75 kV is the maximum displacement when connected to a spring.

corresponding displacements at 5.75 kV. The final design with six layers produces 0.85 N at 1.3 mm.

5.3.3   Force-Displacement Relationship

Although performance with a spring is a reasonable baseline, human fingerpad stiffness can vary between individuals or as a function of gripping force [110]. To address this issue it is useful to measure the force-displacement behavior at a given voltage.

The force-displacement relationship for several voltages was found using a muscle lever as illustrated in Figure 5.8 (A). First, to eliminate the viscous behavior of the EAP, it was charged for four seconds while held in place with the muscle lever at its undeflected position, as in Figure 5.6 (A). The lever displacement then increased in increments of 0.1 or 0.2 mm, allowing the electrodes to expand. The corresponding force was measured at each position, resulting in the curves shown in Figure 5.10.

To interpret the data in Figure 5.10 it is useful to consider two different users. In this example, user (A) has a stiffer fingerpad than (B). This could be due to inherent properties like stiffness of the skin as well as controllable factors like tightness of the grip [110]. The EAP actuator and the fingertip skin will move together, with the same displacement. The equilibrium point, where they come to rest, occurs when the forces are also equal – i.e., where the ascending (dashed) and descending (solid) lines intersect. Thus we see that user
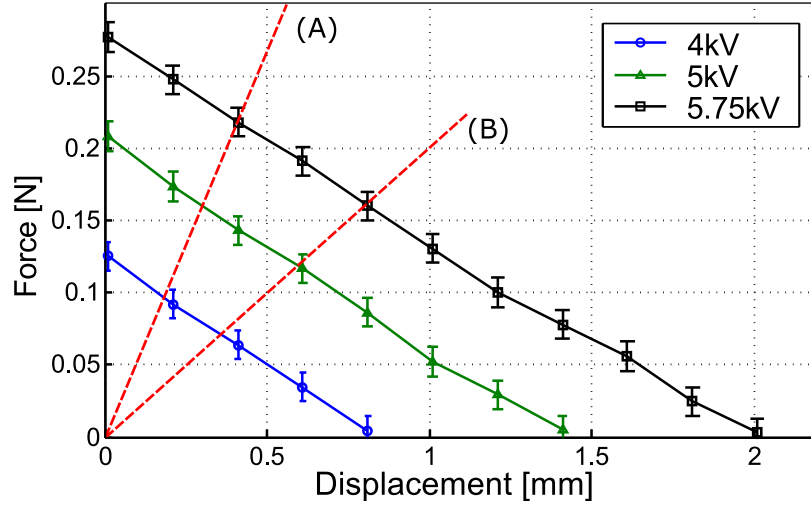
Figure 5.10: Force-displacement relationships of a single EAP for different voltages represented by solid lines. Dashed lines (A) and (B) represent two different human fingerpad stiffnesses. The force and displacement experienced by a fingerpad of stiffness (A) or (B) is equal to the coordinates of the intersection point with the line of that stiffness and the force-displacement line of the correct voltage.

(A) will experience less displacement but a higher force than (B) for the same voltage. In summary, the perception of the stimulus depends on both force and displacement and we can estimate the force and displacement that a user experiences depending on their skin stiffness from Figure 5.10. While the user studies presented here do not have controllers that take individual skin stiffness into account, the variance of the absolute threshold test results, which will be presented in Section 5.6.1, provides enough information to create a haptic signal that is easily perceivable. Fully integrating the characterization results of Figure 5.10 into a subject-specific closed-loop controller is a promising area of future work.

5.4   MR-compatibility Test

To use the haptic display for a robotic or teleoperated needle intervention under MR guidance, it is important to establish MR-compatibility.

The standard requirements for MR compatibility are (i) that the device should be safe to use in the high magnetic field and radio frequency waves from an MRI scanner, (ii) that the performance of the device should not be significantly affected by the MR field, and (iii) the device should not reduce the quality of MR images. As the haptic device has no

ferromagnetic materials and current on the order of μA, we anticipate compatibility; to confirm this, MR-compatibility tests were conducted. Typically the haptic device would be near the front edge bore during procedures as shown in Figure 5.5. In addition to that scenario we also examined the more demanding case where the device is placed inside of the bore near the iso-center. Furthermore, we used the fMRI imaging sequence, which is more sensitive to disturbances in the magnetic field.

The high voltage (HV) circuit used to test the MR compatibility of the device is shown in Figure 5.11. The circuit was designed to utilize an existing data acquisition system in the MR facility. Two optocouplers were used to control the EAP haptic device. An inductor and capacitor were added to reduce possible noise. A small regulated HV DC to DC converter (EMCO X60, size 28 x 66 x 13 mm) amplifies an input signal ranging from 0-5 V, producing an output voltage from 0-6 kV. The data acquisition system has a limited number of output pins which have small output current. To actuate the device with this data acquisition system, the output of the converter is held at a constant high voltage and the optocouplers are used to charge and discharge the EAP devices. Two transistors turn the optocouplers on and off in accordance with a control line from the computer. A 1000:1 high voltage differential probe (Keysight Technologies Inc., N2891A) was used for testing the circuit.
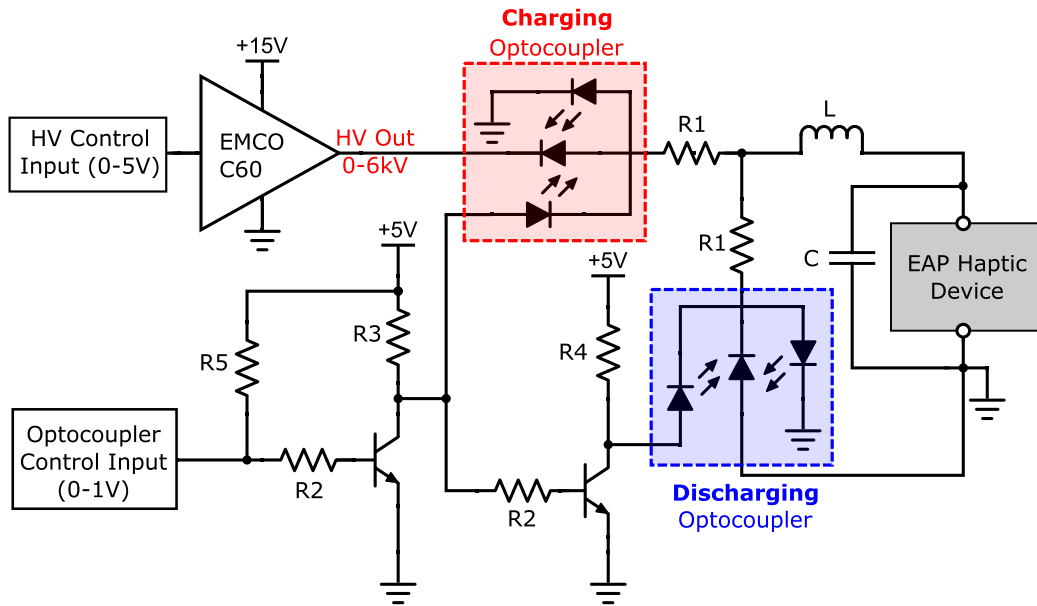
Figure 5.11: Modified miniature HV circuit for usage in MR room.

The DC power supply for the HV control circuit and computer were located outside the MR room. Wiring was passed through a standard filtered connector to the MR room to minimize RF noise from the computer and electrical system.

5.4.1 Safety in MR Environment

All the materials of the device and the EAPs were non-ferromagnetic and there was no force/torque or heat due to the magnetic field while the device is actuated inside the MR room.

5.4.2 Effect of MR field

To test the effect of the MR field on the performance of the device, the free displacement and the displacement when connected to a nonmagnetic spring of stiffness $1.37\,\mathrm{N/mm}$ were compared for conditions outside the MR room versus next to the head coil for a $3\,\mathrm{T}$ magnetic field (GE MR 750, Lucas center for imaging, Stanford).To track the displacement, we recorded video of the EAP with a paper ruler in the video frame for reference.

The test results are shown in Figure 5.12 and Welch's t-test shows that there is no significant difference in free displacement (p-value: 0.08) or spring deflection (p-value: 0.6) when the EAP device is inside the MR bore and when it is outside of the MR room.
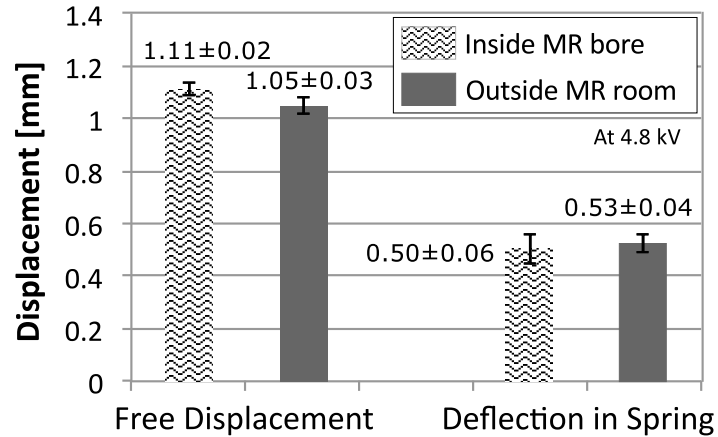
Figure 5.12: Effect of 3-Tesla magnetic field on the performance of the EAP haptic device. There is no significant difference in displacement and force (deflection in spring) when the EAP device is inside MR bore or outside of MR room.

Furthermore, the results of this MR compatibility test were compared to the capability of a distant single layer EAP in Section 5.3.3. Compared to the one layer EAP force values (Figure 5.10), the force capability of the device (a six layer EAP) should be approximately six times larger, corresponding to a value of 0.76 N at 5 kV (with 0.5 mm displacement). The force of the six layer EAP device is derived to be 0.69 N (at 0.5 mm) and 0.72 N (at 0.53 mm), inside and outside the MR room, respectively (Figure 5.12). These values were measured at 4.8 kV; therefore, they are expected to be slightly smaller than the force level at 5 kV (0.76 N).

The device displacement capability should be independent of the number of EAP layers because they are attached in parallel. The free displacement at 4 kV and 5 kV (when the force is 0 N) is 0.75 mm and 1.4 mm, respectively (Section 5.3.3). The free displacement measured at 4.8 kV for the MR-compatibility test is 1.1 mm inside the MR bore and 1.04 mm outside the MR room, which fall in the predicted range.

Since the force and displacement test results do not differ significantly when the device is inside the MR bore and outside the MR room, and fall in the range predicted from Section 5.3.3, it is confirmed that the performance of the haptic device was not significantly affected by the MR field.

5.4.3   Imaging Effects of Haptic Device

In this subsection we report on two types of test results of the imaging effects of the device and its miniature high voltage (HV) circuit in several configurations:

A Baseline (everything off): miniature HV circuit and device inside the MRI room, 3 m away from the MR bore.

B Located near an fMRI head coil (everything off): circuit located 3 m from bore, device located 14 cm from isocenter of the scanner.

C HV circuit powered but no voltage sent to device; locations as in case B.

D 3 kV square wave (50% duty cycle at 0.5 Hz) applied to device; locations as in case B.

E 4.8 kV square wave (50% duty cycle at 0.5 Hz) applied to device; locations as in case B.

The locations mentioned in above list were selected for testing the device where the magnetic field strength is near minimum and maximum. For the 3 T MR machine, the magnetic field strength falls below 10 Gauss (= 0.10 mT) at a distance of 3 m from the iso-center. The device functionality was checked under both a very weak and a strong magnetic field (3 T) at a distance of 14 cm from the iso-center (the distance from the iso-center to the end of the head coil).

A first type of test was to analyze the temporal signal/noise ratio (tSNR) for each of the tested cases (A-E). A 3 T GE MR 750 system and 8-channel head coil were again used to collect test data. The imaging target was a 175 mm diameter spherical agar phantom. An fMRI spiral-in/out imaging sequence was used with TR/TE/FA = 2000 ms/30 ms/90 deg and 3.43 x 3.43 x 0.4 mm voxel size.

The results summarized in Table 5.2 show that there is not a significant decrease in tSNR when the device is activated. However, there is a small reduction in tSNR introduced by the electrical system compared to the baseline (case A).

<p align="center">Table 5.2: tSNR Values for Test Conditions A-E</p>

Case	HV Circuit	Voltage Across EAP	Distance of EAP from Iso-center	tSNR	tSNR Reduction Relative to:	
					Case A	Case C
A	Off	0	Outside of magnet (3 m)	472		
B	Off	0	Next to head coil (14 cm)	465	1.48 %	
C	On	0		464	1.69 %	
D	On	3 kV		464	1.69 %	0 %
E	On	4.8 kV		462	2.12 %	0.43 %

A second type of test was performed using three plane images of the localizer scan and a Fast Gradient-recalled Echo image method with 31 kHz bandwidth. From the anatomic images acquired from the localizer scans (Figure 5.13) we observe that the ROI standard deviation (SD) is nearly the same for the baseline (case A) and when the EAP device was actuated with a 4.8 kV square wave (case E).

From the test results summarized in Table 5.2 and Figure 5.13, we can conclude that there is not significant noise from operating in the MR field and that only minor image distortion was introduced by the haptic device.
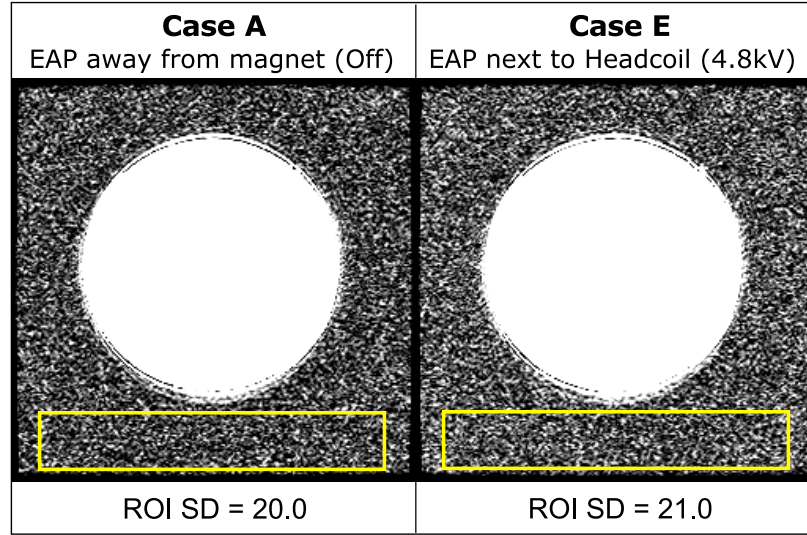
Figure 5.13: Comparing anatomic images with $0\,V$ and a $4.8\,kV$ square wave. The yellow boxes indicate the regions of interest (ROI)

5.5   Haptic Feedback System

5.5.1   System Components

The EAP haptic device's characteristics and MR-compatibility were checked in the preceding sections. In this section, we describe the haptic feedback system designed to drive the EAP haptic device based on the axial force reading of the FBG needle from Chapter 3.

The haptic feedback system consisted of several communicating components, as shown in Figure 5.14. The optical interrogator (Micron Optics, SM-130) samples the FBGs at $1\,kHz$. The overall latency from when a force is applied to the needle to a commanded change at the
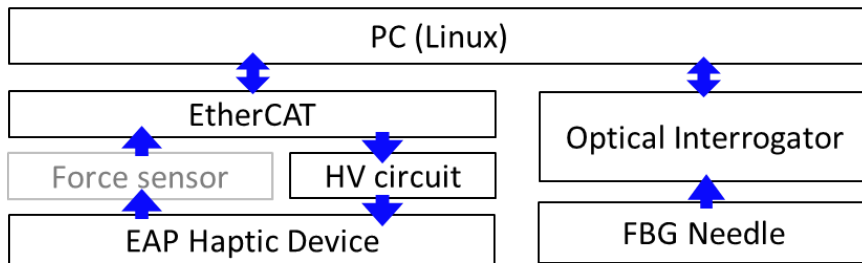
Figure 5.14: System schematic block diagram. The force sensor was used only for characterizing the system.

output of the high voltage supply is approximately 50 ms. The communication and control system used in this chapter is identical to the system described in section 4.3.2 except it is now connected to the high voltage (HV) circuit for driving EAP haptic device instead of the ultrasonic motor drive board.

For portability and ease of integration with EtherCAT, we used a high voltage amplifier (XP-EMCO, AH60) which produces up to 6 kV, linearly proportional to the input voltage of 0.5-5 V.

EAP actuators require voltages higher than standard transistors tolerate, so we built a switching circuit to charge and discharge the EAP actuators as shown in Figure 5.15. A high voltage opto-coupler (Voltage multiplier Inc., OC100G) and a high voltage resistor were used to control charging and discharging of the EAP haptic device and limit the charging current for safety. The maximum current an opto-coupler can discharge is 120 μA, and the current that can be supplied to an EAP from the charging opto-coupler is 60 μA. We grounded all user-contacting parts and limited the maximum supply current for user safety.

A 1000:1 high voltage differential probe (Keysight Technologies Inc., N2891A) was used for testing the circuit.
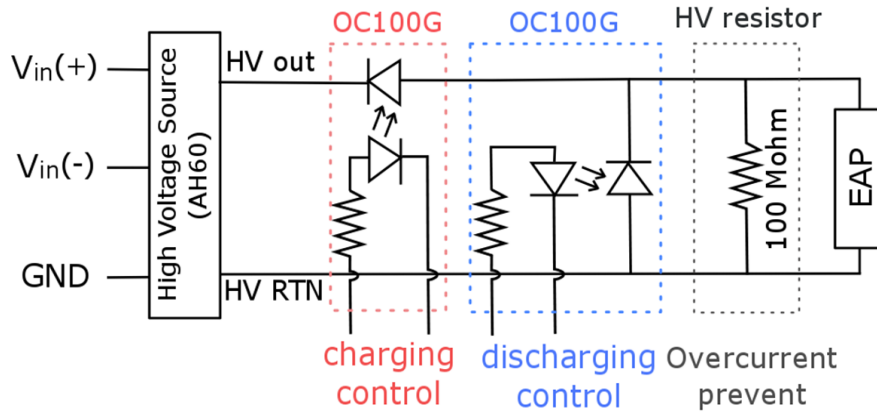
Figure 5.15: The high voltage control circuit for the EAP device. The power resistors in the charging and discharging circuit were 600 Ω and 300 Ω, respectively.

5.5.2 System Testing

The haptic feedback system was tested after integration. First, we compared the input control signal and EAP output force in response to a step function. The EAP actuator was

connected in series with a $1.2\,\mathrm{N/mm}$ spring as in previous tests, and control signals were sent via the charging circuit. The discharging circuit is controlled by switching the opto-coupler. From the test, we noticed that the charging speed is faster than the discharging speed and that there is some viscoelasticity in the VHB material. Thus, the initial response to a step function is considerably faster than the relaxation, as seen in Figure 5.16.

Increasing the discharge rate of the EAP is useful to increase the responsiveness of the system to repeated forces. Combining a $100\,\mathrm{M\Omega}$ resistor in parallel with the EAP (which slightly reduces the maximum force) and an opto-coupler increased the discharge rate (Figure 5.16).
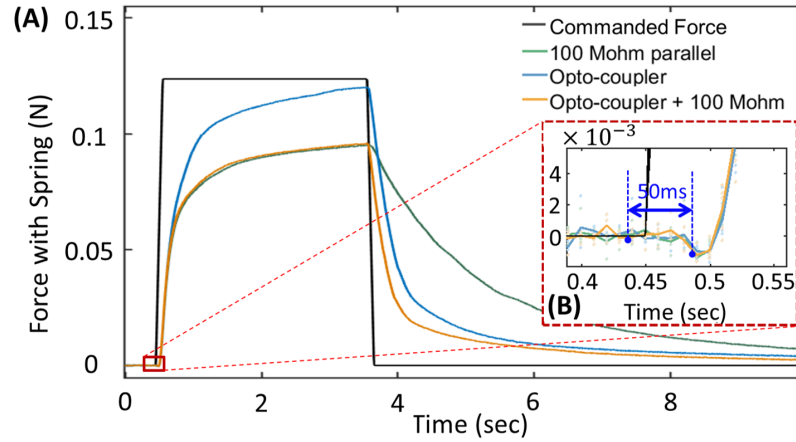
Figure 5.16: (A) EAP (3-stack) force profile for 3 discharging methods with a step voltage command (force command) that rises over $0.1\,\mathrm{s}$, holds for $3\,\mathrm{s}$ and falls over $0.1\,\mathrm{s}$. Solid curves show average values for a group of 5 tests. An enlarged view (B) shows the delay from the start of voltage rise to EAP response.

Second, we checked whether the axial force of the force sensing needle can be displayed effectively through the EAP haptic device.

For an isolated event such as a membrane puncture, the residual force due to slow discharging is not a limitation; however, for rendering continuous dynamic forces, this effect would be problematic. Furthermore, insufficient discharging may cause accumulation of residual charges and result in shifting the baseline force, as seen in needle tapping data in Figure 5.17 (A). So we extended, in software, the discharging period associated with each drop in force, producing the results shown in Figure 5.17. The gray area shows when the discharging opto-coupler is on. The system in Figure 5.17 (B) has a longer discharging period, thus charge does not accumulate. After these modifications to improve discharging,

as shown in Figure 5.18, the displayed force from EAP haptic device tracks the axial force of the force sensing needle.
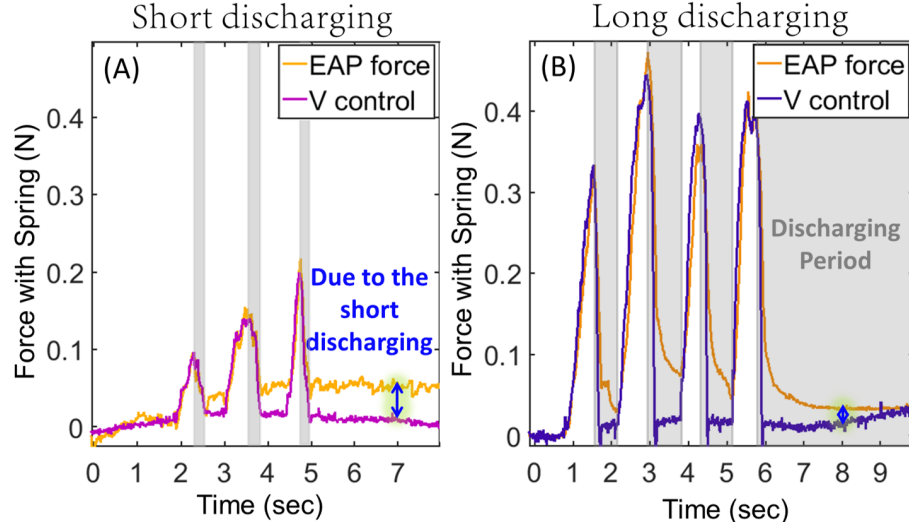
Figure 5.17: Different discharging periods produce different results for a needle tapped on a rubber block in air.
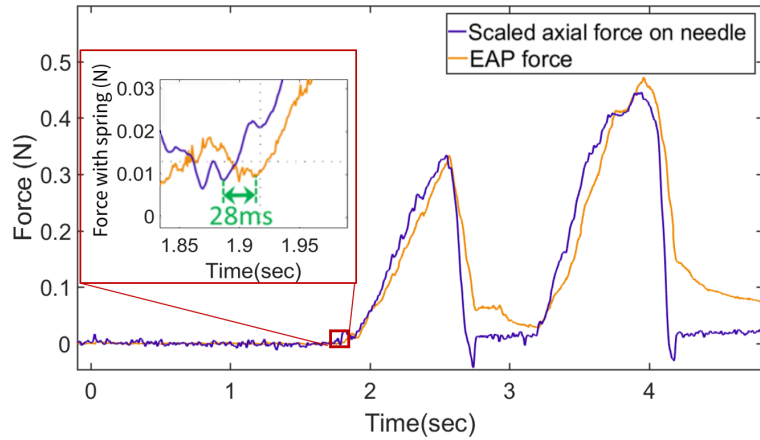
Figure 5.18: The displayed force from EAP haptic device follows the axial force of the force sensing needle (FBG needle) well with a small delay.

5.6 Psychophysics Test

Using the haptic feedback system, we first tested the EAP haptic device from the standpoint of psychophysics. During this test, the haptic feedback was directly driven to create a

consistent force profile for each test.

Twelve test subjects (10 male, 2 female, age range: 23-33 years old; mean: 26.1 years old) were recruited for the experiments. We trained the subjects to have a similar grip force and asked them to maintain a consistent force for the experiments.

5.6.1 Absolute Threshold Test

To test the functionality of the EAP skin stretch device we first checked the absolute threshold and compared it to other skin stretch devices that use small RC servos or DC motors.

Method

A simple up-down staircase method was used to obtain the detection threshold (X_{50}) [111]. Data were collected until the 12th reversal, and analyzed as described in [111]. Stimuli were given at random time intervals to prevent users from predicting the timing. In operation, the skin stretch device's tactors move with pre-defined speed until they reach the target stimulus magnitude, remain for 2 seconds, and then return to the initial position at 1/6 the speed (Figure 5.19). Thresholds were obtained for speeds of 0.194 N/s, 0.439 N/s, and 0.930 N/s. In all cases, the initial stimulus was 0.11 N.
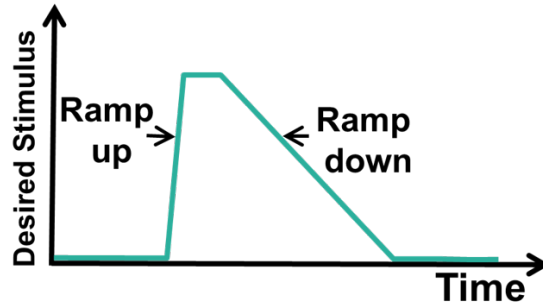
Figure 5.19: The trajectory of the tactors during absolute threshold test.

Results

The results summarized in Table 5.3 are consistent with prior research on skin stretch displays (e.g., [68, 112]), which report the absolute threshold that decreases as the speed of displacement increases.

Table 5.3: Threshold of perceptible force results for 12 subjects

Force	0.25 N/s	0.52 N/s	1.06 N/s
Mean (N)	0.13	0.11	0.07
SD (N)	0.02	0.01	0.01
[39] stretching finger pad	0.5 mm/s	1 mm/s	
	~0.05 mm	less than 0.05 mm	
[40] stretching palm	1 mm/s	2 mm/s	
	0.44 mm	0.26 mm	

5.6.2 Confusion Matrix

To understand how well people can interpret the size of stimuli, we gave users 3 different magnitudes of force (and displacement). Excellent discrimination would give confidence that this device provides a useful representation of the tissue stiffness changes encountered during needle insertion.

Method

We chose the moving speed of stimulus as $0.6\,\text{N/s}$ ($0.5\,\text{mm/s}$, $k = 1.2\,\text{N/mm}$), which approximates the slope of the peaks in the membrane puncture test with a constant insertion speed of $6\,\text{mm/s}$. Three stimulus magnitudes higher than the JND values were chosen from a pilot test: $0.15\,\text{N}$ (small), $0.275\,\text{N}$ (medium), and $0.5\,\text{N}$ (large) (Figure 5.20). Subjects
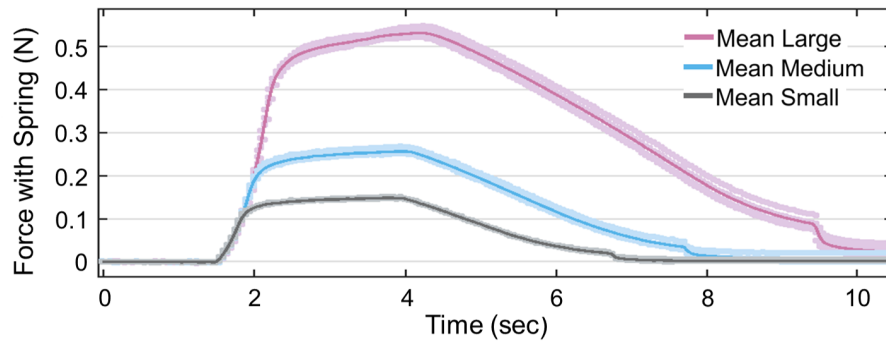
Figure 5.20: EAP force output with a spring ($k = 1.2\,\text{N/mm}$) corresponding to a small, medium and large stimuli. The slight increase in force over time is due to the viscoelasticity of the VHB film.

received training until they were confident in differentiating the magnitudes. Each subject received 10 of each stimulus magnitude (30 total) in randomized order.

Results

Users differentiated small and large magnitudes well but often confused medium stimuli with small ones (23%) and large stimuli with medium ones (22%). Overall, users perceived the different magnitudes correctly with > 70% accuracy (Table 5.4).

Table 5.4: Confusion matrix for 12 subjects and 10 instances of each stimulus magnitude.

		Given		
		Small	**Medium**	**Large**
	Small	**100 (83%)**	27 (23%)	0 (0%)
Answered	**Medium**	19 (16%)	**84 (70%)**	26 (22%)
	Large	1 (1%)	9 (8%)	**94 (78%)**
Total		120	120	120

5.7 Robotic Membrane Detection Test

A total of 10 subjects participated in this test. They are a subset of the users who participated in the previous psychophysics test. All of the participants had no medical experience in manipulating needles.

5.7.1 Experimental System Setup

Robotic system

We approximated a robotic needle insertion system with a single-axis microcontroller driven linear stage (MAXY4009W2-S4-0, Velmex Inc.). The needle was attached to this linear stage (Figure 5.21). The microcontroller controlled the linear stage with a preprogrammed insertion speed. The insertion speed was designed to accelerate with $1\,\mathrm{mm}/s^2$ until it reached $6\,\mathrm{mm/s}$, which was then kept constant. As the stage drove the instrumented needle into a tissue phantom, the user manually tracked the needle motion by pushing the haptic device along a linear slide and felt for a membrane puncture.
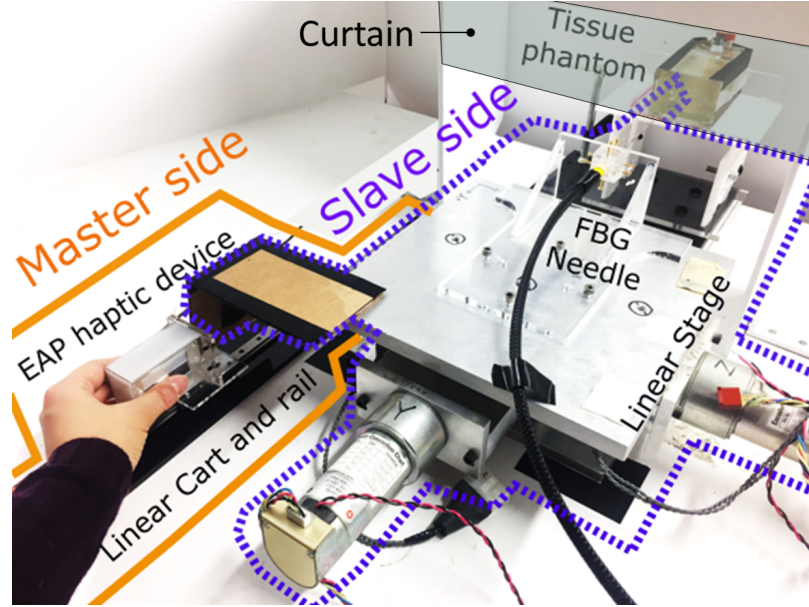
Figure 5.21: System for detecting membrane contact and puncture: the slave side is mounted on a linear stage that drives the FBG-instrumented needle into a tissue phantom. The axial needle tip forces it experiences are relayed to the master side and displayed with the EAP haptic device. The user's job is to manually track the slave side and feel for a membrane puncture.

Tissue Phantom with Embedded Membrane

Tissue phantoms used in the experiment were gelatin (Knox Unflavored Gelatin) with a ratio of gelatin powder to water of 1:4. The stiffness of the gelatin was 8.3 kPa, which is in the range of the Young's modulus for normal and fibrotic liver [113]. Phantoms were 8 cm by 8 cm in cross-section and 7 cm in depth, allowing multiple needle insertions.

The tissue phantoms were gelatin, and the membranes were plastic film, 12.5μm thick. The gelatin stiffness was 8.3 kPa, corresponding to 325.6 N/m for the needle. Average membrane puncture forces were 1.01 N (SD = 0.01 N). For each phantom, a membrane was located at different locations: 3 cm, 6 cm, or 8 cm. The phantoms were used 6 times each in random order, resulting in 18 puncture tests. The phantom was covered with a curtain to prevent participants having visual feedback about the membrane puncture moment.

5.7.2 Experiment Procedure

During the robotic needle insertion paradigm, a motorized linear stage drove the needle at a constant 6 mm/s into a tissue phantom with a membrane at a variable depth.

Users were told to move the EAP device on a rail (Figure 5.21) while holding the tactors, approximately following the predefined motion of the needle. In this scenario, the users are passive observers of the haptic stimuli and are asked to press a button when they feel a stimulus corresponding to membrane contact. The users (N = 10) were the same as in the threshold test in the previous section 5.6.1 and were trained through two example membrane punctures.

Successful membrane detection was defined as the user stopping the linear stage shortly after the needle contacted the membrane. The distance between the membrane and needle tip was measured with an encoder on the linear stage.

5.7.3 Results

Users (N = 10) successfully detected 98.9% of membrane punctures, with the needle stopping an average of 4.5 mm after the membrane (SD = 1.6 mm). Much of this distance is due to various time delays in the system: First, there is at least 50 ms delay between the input control signal and the start of EAP actuation. Next, the user must perceive the change in the EAP haptic display. When the linear stage is moving at 6 mm/s, the force at the needle tip increases at 0.6 N/s due to the membrane stretching. From our JND study, we found that 0.104 N and 0.085 N is required for a constant display speed of 0.44 N/s and 0.93 N/s, respectively. Therefore, it takes between 91 ms (= 0.085 N / 0.93 N/s) and 236 ms (= 0.104 N / 0.44 N/s) to reach the threshold force with the speed of 0.6 N/s. The third step is the reaction time of a user to physically press the switch, which is approximately 367 ms with a standard deviation of 39 ms [114]. The last step is the mechanical time constant of the stage, which requires approximately 333 ms to come to a complete stop. Thus, in total, approximately 890 ms of time delay may occur between membrane puncture and needle stoppage. This time delay corresponds to 5.3 mm - displacement of the linear stage. Since our result 4.5 mm (SD = 1.6 mm) is comparable with the above calculation, we can conclude that the membrane puncture was detected successfully.

5.8 Teleoperated Membrane Detection Test

A second study explored a teleoperated needle insertion scenario with users experienced in needle-based procedures. The subjects were individuals in the Stanford University Department of Radiology with between 1 and 30 years of experience in needle-based procedures. We tested 10 users but excluded one user's data due to a misinterpretation of the study's directions, leaving a total of 9 users.

5.8.1 Experimental System Setup

Master-Slave system

To build a single-axis teleoperation system, the passive linear rail (master side) was instrumented with an encoder to capture motions imparted by the user as shown in Figure 5.22 and Figure 5.23 (A). The EAP haptic device was mounted on the linear carriage of the master side.

The needle is mounted to a powered linear stage (slave side) operated under servo control by a microcontroller (Teensy 3.2) (Figure 5.22). The slave system is a single-axis linear stage (MAXY4009W2-S4-0, Velmex Inc.) that supports the needle as it is driven into a tissue phantom (Figure 5.22). For the previous robotic membrane detection test, the slave side
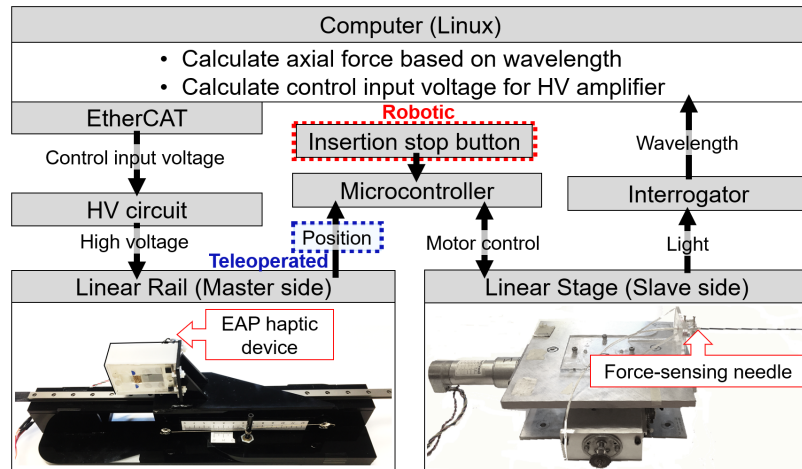
Figure 5.22: System schematic block diagram for both robotic and teleoperated membrane puncture test setups. The robotic insertion case has a button to stop the insertion as the linear stage automatically inserts the needle with constant speed (6mm/s). In the teleoperated case the user manually controls the insertion speed.
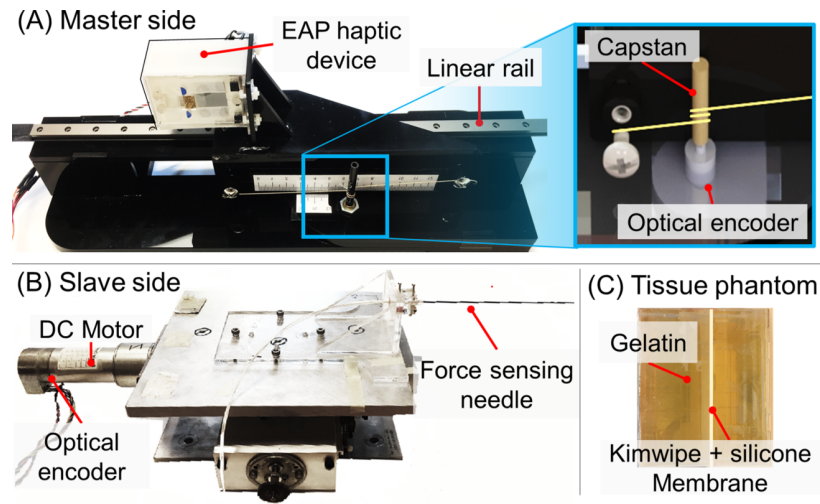
Figure 5.23: Teleoperation system configuration. (A) Master side: The EAP haptic device was mounted on the linear rail's cart. The position of the cart was measured by an optical encoder attached to a capstan. (B) Slave side: A DC motor drives the slave side (linear stage) based on the position of the master. (C) Tissue phantom: A tissue phantom was made with gelatin and kimwipe + silicone membrane.

inserts the needle automatically and users stop the motion by pressing a button. In this teleoperated paradigm, users control the motion of the slave by pushing the haptic device along its linear rail. This was achieved by using a microcontroller that servos the motor of the linear stage based on the motion of the haptic device (master side).

The positioning accuracy of the motor control loop is approximately $60\,\mu$m with speeds of up to $11\,$mm/s. Used for bench-top tests, it is a proxy for an eventual MR-compatible teleoperation system.

Axial Force Feedback Rendering

After the FBG sensors are read and converted to force values and filtered, the corresponding voltage is computed for the high voltage amplifier. The latency from needle sensing to high voltage actuation is approximately $50\,$ms. Several strategies were used to minimize the effects of noise and the breakage of EAP actuators.

Minimum force threshold: The force signals contain some noise due to inertial forces, friction between the needle tip and tissue, and temperature effects. Based on pilot force sensing, a threshold of $0.09\,$N (corresponding to a $1.4\,$V input to the HV supply) is set. When the measured force is below this threshold, the HV amplifier input is fixed at $0.5\,$V,

corresponding to the hardware threshold of the amplifier.

Maximum voltage: To prolong the life of the EAPs, the input voltage to the amplifier was capped at $3.3\,V$, corresponding to a $4.5\,kV$ output and $\approx 0.6\,N$ force produced by the haptic device for a user with a fingertip stiffness of $1.2\,N/mm$.
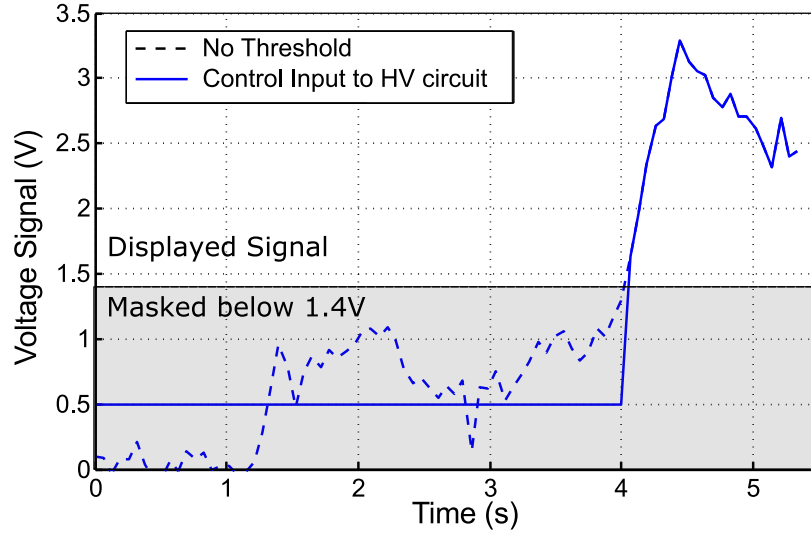
Figure 5.24: Amplifer input voltage with and without threshold. If the commanded input voltage is below $1.4\,V$, it is set to $0.5\,V$ to avoid low-level noise. The input voltage is also capped at $3.3\,V$ to prolong EAP life.

Tissue Phantom with Embedded Membrane

The tissue phantom base material for both the robotic and teleoperated user studies was the same; the membrane was changed to simulate a more realistic testing environment. The membrane consisted of a wipe (Kimwipes) coated with a layer of silicone (Dragon Skin Fx-Pro) with a total thickness of $0.6\,mm$ [15, 24]. The thickness and material were determined empirically, by comparison to the puncture force of an ex-vivo porcine liver capsule, which is approximately $0.17\,N$ (SD $= 0.06\,N$) with a constant insertion speed of $6\,mm/s$.

To measure the puncture force, the ex-vivo porcine liver outer membrane was separated from the rest of the liver tissue using a sharp razor blade and mounted in a rectangular frame (the same frame used to measure the puncture force of the artificial membrane) and punctured using the instrumented needle described in Section 3. Figure 5.25 shows similar peak amplitudes for the two membranes.

The phantoms were $8\,cm$ by $8\,cm$ in cross-section and $7\,cm$ in depth, allowing multiple

needle insertions. Membrane puncture forces measured were similar for multiple punctures across the area as long as the gap between insertions was larger than 5 mm. In each phantom a membrane was embedded at either 2.5 cm or 3.5 cm from the top surface, as seen in Figure 5.23 (C).
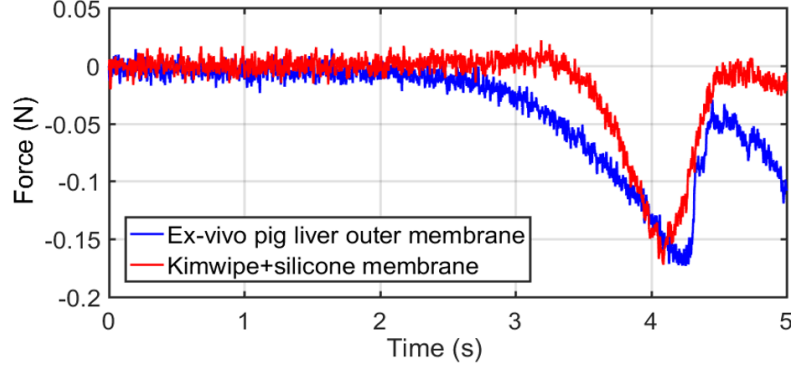
Figure 5.25: Membrane puncture force comparison for phantom and ex-vivo pig liver.

5.8.2 Experiment Procedure

We first familiarized the subjects with the skin stretch stimulus. Users placed their fingers on the two tactors without moving along the linear rail. We then applied signals at random intervals to confirm that they could detect the stimulus.

We trained users as in the robotic paradigm to detect haptic stimuli as the needle was driven at a fixed speed of 2, 4, or 6 mm/s. We asked subjects to approximately follow the motion of the needle by pushing the haptic display along its linear rail (master side) and to respond to the haptic stimulus when they detected a membrane. The motivation for testing at three speeds is that the puncturing force is slightly higher at higher speeds [115], and the sensitivity to skin stretch also increases with speed [69, 112].

After the training session, for the actual membrane detection test, we asked users to insert the needle by pushing the master at a user-determined approximately constant speed (i.e., no sudden acceleration or deceleration) in the range of 2 - 6 mm/s.

Although the membrane location was 25 mm from the top surface, the needle insertion starting location was randomly selected among 5, 10, or 15 mm inside the phantom.

5.8.3   Results

Users (N = 9) were able to detect the membrane successfully in 105 of 107 insertions (98.1% success rate). In 14 out of 105 successful membrane detections, users stopped the needle fast enough not to puncture the membrane. In the remaining 91 insertions, users successfully detected and punctured the membrane while decelerating the haptic device on the linear rail. The needle fully stopped after 2.78 mm (SD = 1.66 mm) from the initial contact of the membrane. This distance includes the stretch of the membrane (2.44 mm, SD = 1.72 mm) and the distance the needle traveled after puncturing the membrane (0.34 mm, SD = 0.46 mm). The results are summarized in Table 5.5.

Table 5.5: Results of membrane detection test

	Insertion Speed (mm/s)	Tip-membrane distance after puncture (mm)	Detect-stop distance (mm)
Mean	5.46	0.34	2.78
SD	2.65	0.46	1.66
Min	0.93	0.00	0.36
Max	11.38	2.89	8.10

	Peak axial Force (N)	Peak EAP force (N)	Peak V control input to HV amplifier (V)	V control input slope (V/s)
Mean	0.19	0.49	2.89	4.14
SD	0.05	0.23	0.87	2.39
Min	0.10	0.10	1.44	0.16
Max	0.33	1.11	5.18	15.50

To interpret the data it is useful to realize that membrane puncture can occur in two different ways. In the first case, illustrated in Figure 5.26 (A), both the stylet and the outer cannula pass through the membrane with a corresponding rapid drop in the force. This produces a strong transient signal for the haptic device. In the second case, shown in Figure 5.26 (B), only the stylet pierces the membrane. The force remains roughly constant after increasing. Note that this sustained force will continue to be rendered by the haptic device and, because skin stretch stimulates slow-acting as well as fast-adapting mechanoreceptors [116, 117], it will continue to provide a sensible stimulus to the user.

Users operated the needle at an average insertion speed of 5.46 mm/s (SD = 2.65 mm/s). The average membrane puncture force of 0.19 N (SD = 0.05 N) is slightly higher than the force measured with a constant insertion speed of 6 mm/s (0.17 N). This average force
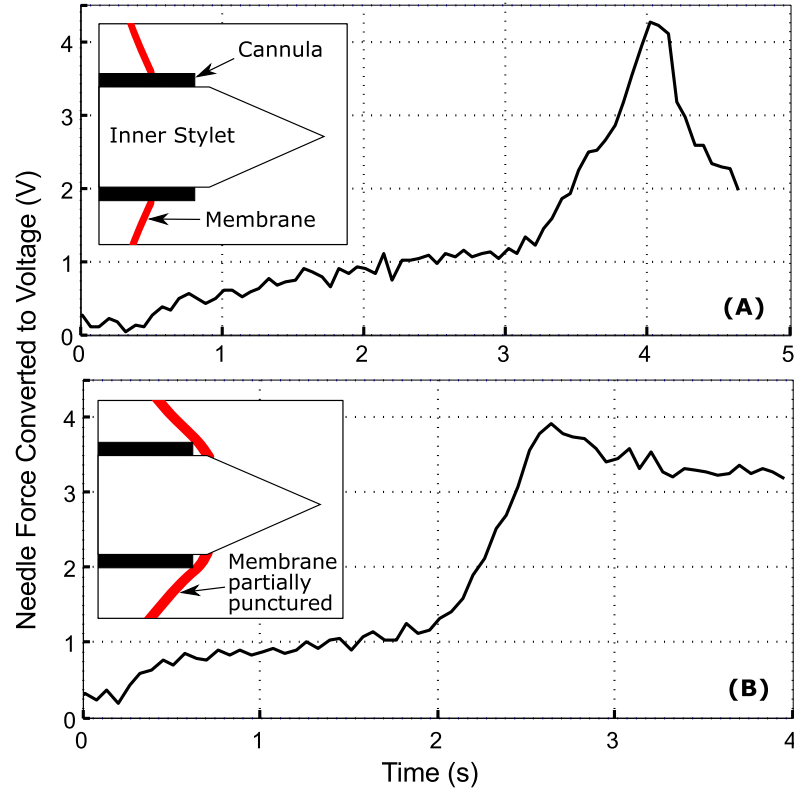
Figure 5.26: Two types of membrane punctures: (A) membrane is thoroughly punctured (B) only the inner stylet punctured the membrane and the membrane is stuck on the outer cannula.

corresponds to $2.9\,\text{V}$ control input voltage to the HV circuit, producing $0.5\,\text{N}$ at the haptic device when actuated against a $1.2\,\text{N/mm}$ spring.

To further interpret the results, we consider that needle insertion speed affects the peak force of a membrane puncture [115]. Accordingly, we are interested in whether the measured peak force increases with the needle insertion speed. In addition, we consider the correlations between insertion speed and the rate of change in the control input voltage of the HV circuit, as well as the distance the needle travels after contacting the membrane.

As seen in Figure 5.27, peak axial force from the needle increases with insertion speed, which is consistent with previously reported results [115]. Perhaps not surprisingly, the stopping distance also increases with insertion speed, although the correlation is less strong. This is despite the fact that the commanded voltage to the haptic display and the haptic stimulus intensity also increase with insertion speed.
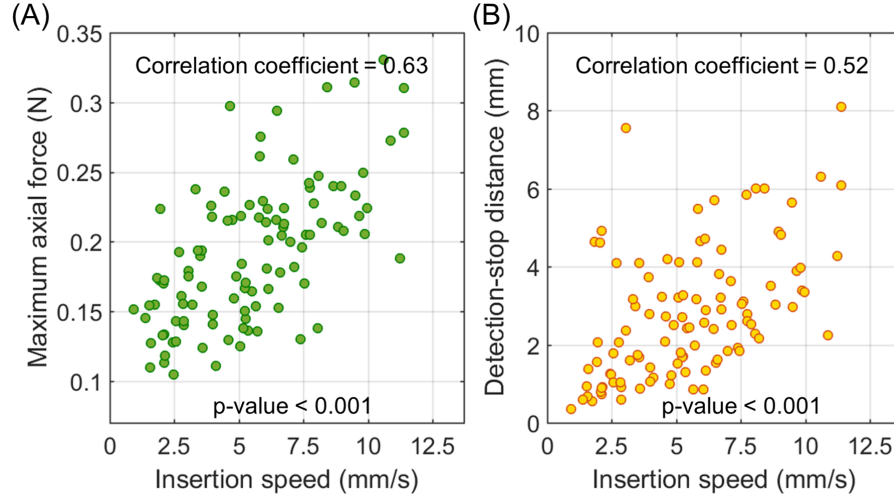
Figure 5.27: (A) Correlation between insertion speed and maximum axial force during membrane puncture. (B) Correlation between insertion speed and the detection distance.

To interpret the data on stopping distance it is again useful to consider the effect of delays in the system. As in the robotic paradigm there is a 50 ms latency between a force measured at the needle tip and a high voltage command to the haptic display. In addition, there may be ≈300 ms human reaction time, although the response may be faster when the stimulus occurs as a direct result of human motion. For an average insertion speed of 5.65 mm/s (SD = 2.65 mm/s), these delays suggest that the needle will stop approximately 2.4 mm past the membrane. Adding the membrane thickness, 0.6 mm to 2.4 mm, we estimate a detection-stop distance of 3 mm. This estimate aligns with our measured detection-stop distance of 2.8 mm.

5.9 Discussion

The results of the first robotic paradigm test with naive users and the second teleoperated test with users experienced in needle procedures are similar. In both cases, the detection rate is very high (≈ 98%), indicating that users had no difficulty in detecting the stimulus.

The stopping distance, after accounting for communication latency and inertia in the system, is also similar (slightly under 3 mm). This result is perhaps less expected given the differences in conditions between the two experiments. In the first experiment, users were responding to an autonomously driven needle, receiving a haptic "event cue" that

was anticipated but after an uncertain interval. They had no difficulty recognizing the cue and pressing a button, with typical human response times. In the second experiment, users received the haptic stimulus as part of an afferent/efferent loop. Moreover, these were users with experience in manipulating needles and detecting the forces associated with contacting membranes. Indeed, a few of the experienced users did produce very low average forces (0.22 N in one case) and were able to detect the membrane without ever piercing it. However, the second group of users were free to chose their own preferred speed to guide the needle via the master device. They also applied more or less side load on the sliding rail, which could produce more friction. Finally, the second group of users stopped the needle by arresting the motion of a (slowly) moving hand, which is not the same as pressing a button. Given that the puncture force and the rate of ramp-up of the displayed force both depend on speed, it is not surprising that there was more subject-to-subject variability. One additional difference is that the phantom and membrane were somewhat different in the second experiment; in particular, the membrane could stretch up to 2.44 mm before puncture.

We also observed two instances in the second test where users failed to detect the membrane contact event. The failure occurred during the corresponding user's first trial. The peak force, insertion speed, and force slope did not differ significantly from successful membrane detections. We speculate that the two cases of detection failure were caused by the initial learning curve associated with using a new device and could be remedied with additional training.

5.10 Conclusion and Future Work

We present a new MR-compatible haptic display that functions by eliciting skin stretch in the proximal/distal direction when a user holds it between the thumb and index finger. The device is intended to display forces sensed at the tip of a tool, such as an instrumented biopsy needle, during MR-guided interventions. Tests in a 3 T MR machine confirm that the device and its high voltage power supply do not significantly affect the signal/noise ratio of the MR image, even located near the head coil in an fMRI application. This shows that EAP can be potentially used for fMRI studies to comprehend brain activities induced by haptic feedback.

We additionally present the results of two sets of user experiments with the device.

In the first case, users were asked to respond to the haptic stimulus they received as an instrumented needle was driven at fixed speed through a tissue phantom and into a plastic membrane. Users were able to respond reliably and accurately, arresting needle motion by pressing a button. In the second test, we recruited users with experience in needle manipulation to perform a single-axis teleoperated needle insertion. Users guided a master along a low-friction rail and received haptic stimuli from the device. A slave axis moved the needle through the phantom. Users were again able to detect membrane contact with very high reliability, although there was somewhat more subject-to-subject variability as users chose different speeds to propel the needle.

The results of these tests suggest that a haptic display that imparts lateral skin stretch using electroactive polymer actuators is a good candidate for MR-guided robotic and tele-operated interventions. It has the potential to provide physicians with an unprecedented capability: the ability to sense remote forces as though one's fingertips were located remotely at the tip of a tool inside the MR machine.

Extensions to the work will include integrating the display into a complete MR-compatible teleoperated system. Interestingly, given that skin stretch (unlike vibrational feedback) is inherently directional and can display static as well as dynamic forces, there is the ability to provide a multi-axis skin stretch feedback, perhaps using mechanisms such as those presented in other work [118].

Chapter 6

Tissue texture sensing

Membrane puncture, tissue cutting and deflection estimation have all been studied by researchers because knowing these quantities can improve the performance of needle interventions and benefit patients and doctors. Tissue texture sensing adds another piece of information that has the potential to enhance needle procedures. Different types of tissue have different textures, and the texture of some tissue changes as it becomes diseased. For example, liver fibrosis and cirrhosis create significant differences in liver tissue texture, varying the roughness or granularity of the tissue and its stiffness [7, 113]. Some physicians note that they can recognize cirrhotic liver by feeling the texture during a biopsy procedure. Fibrotic or cirrhotic livers often have a harder, rougher and more granular feeling due to the excessive extracellular matrix while healthy liver has less extracellular matrix [7, 113] (Figure 6.1). These observations suggest that if the texture of tissue can be sensed during a needle insertion it could help to confirm or expedite the diagnosis of liver fibrosis/cirrhosis or other tissue diseases inducing a texture difference. In this chapter, we explore the possibility of tissue texture sensing using the instrumented needle from Chapter 3. First, we show the result of bench-top tests using gelatin tissue phantoms fabricated with polyurethane foams of varying pore size. Then we present tissue roughness sensing using chemically fixed human liver samples (healthy liver vs. cirrhotic liver).

6.1   Bench-top Test with Tissues Phantoms

As noted in Section 2.5, there have been many robotic surface texture sensing and classification investigations. Force sensors or accelerometers are perhaps the most common sensor
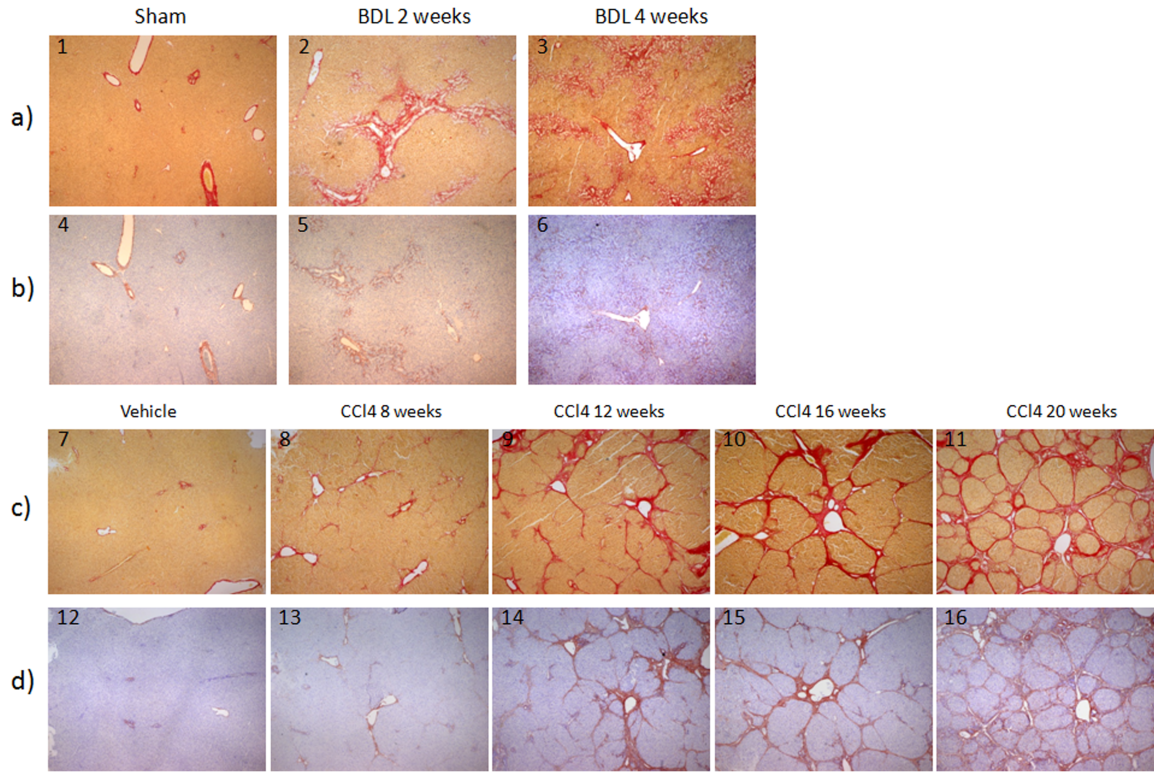
Figure 6.1: The red lines in subfigure (C) are the extracellular matrix (hepatic structure) created in the liver tissue. CCL4(carbon tetrachloride) was treated to induce the fibrosis. As the stage of CCL4 treatment progresses, the amount of extracellular matrix increases. Pictures reprinted from Veidal SS, Karsdal MA, Vassiliadis E, Nawrocki A, Larsen MR, Nguyen QHT, et al. (2011) MMP Mediated Degradation of Type VI Collagen Is Highly Associated with Liver Fibrosis Identification and Validation of a Novel Biochemical Marker Assay. Figure is reprinted from PLoS ONE 6(9): e24753. https://doi.org/10.1371/journal.pone.0024753 [7].

choices for data collection. Various types of signal analysis were used to classify textures including the magnitude and slope of the shear friction force, peak frequency of the power spectral density data, etc. Most approaches to surface roughness sensing have employed spectral analysis of the data. With respect to three dimensional volumetric roughness sensing, relatively few publications exist and it appears that no consensus has been established concerning data analysis methods. Therefore, two different data analysis methods, time domain analysis and frequency domain analysis, were explored and compared for this chapter.

6.1.1 Experimental Setup

We define three-dimensional tissue roughness as a volumetric variation in tissue mechanical properties over a short length scale in comparison to the trajectory of the needle. As a needle passes through heterogeneous tissue, it encounters localized regions of high stiffness and/or high friction interspersed with comparatively soft and low friction regions. These transitions lead to variations in force at the needle tip. To quantify the effect of variations in tissue stiffness and friction on the needle, a bench-top test with a known 3-D spatial variation was first planned.

Through consultation with radiologists, three different gel-filled polyurethane foams created phantom tissues with different roughness. The porosity grades of the polyurethane foams were 10 ppi, 20 ppi and 30 ppi, where ppi stands for pores per inch. The radius of pores in the foam was estimated using the approach in [119] for foam porosity. The radius of a pore varies, and the midpoint of the 30 ppi foam's radius range was approximately 0.8 mm. Using this information, the diameter of 10, 20 and 30 ppi foams were estimated to 1.6 mm, 2.4 mm and 3.6 mm respectively. Three different foams were embedded inside of an acrylic box with dimensions 25.5 mm x 35 mm x 100 mm. Cyanoacrylate glue (Loctite 401) was applied at the bottom surface of the foam and the edge of the top surface to secure it inside of the box.

To create a realistic tissue phantom, a gelatin solution was poured into the box until it
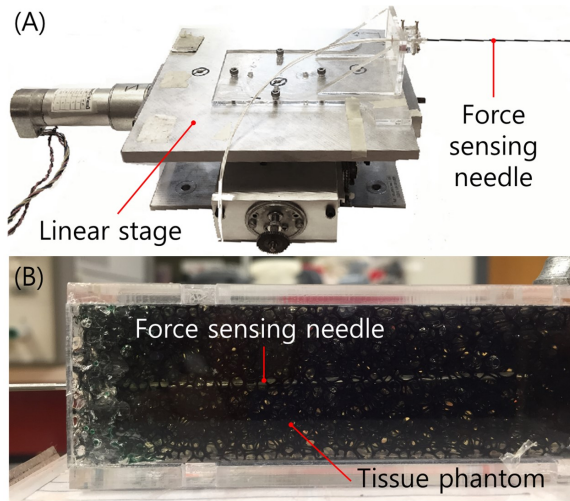
Figure 6.2: (A) The linear stage used to insert the force sensing needle with a constant speed. (B) Tissue phantom is made of gelatin and open-cell polyurethane foam.

filled the pore-spaces in the foam. Filling the pores kept the structure of foam intact as the needle pushed into the phantom. The ratio between gelatin powder and water was 4 to 1 and the possible air trapped inside of foam was minimized by tapping the bottom of the box until no air bubbles appeared at the top surface.

To collect the data for the 3-D roughness sensing, the force sensing needle and a single-axis linear motor stage, as described in previous chapters, were utilized. The force sensing needle was mounted on the linear motor stage and inserted into the tissue phantom with a constant speed.

6.1.2 Hypothesis

When a needle is inserted into the tissue phantom, the needle tip cuts the polyurethane matrix which defines the pores of the foam. As it passes through the gel-filled interstices, forces are lower. As can be seen in Figure 6.3 and Table 6.1, the distance between the polyurethane structures is the diameter of the pore. The varying cutting force will create a feeling of granularity or roughness during needle insertion.

The needle cutting force can be categorized into two phases (Figure 6.4 (A)) [8, 55]. First, the force rises as the deformation of the material being cut increases until it reaches the maximum force that the material can withstand before rupture. Depending on the material's stiffness and the rupture toughness, the maximum axial force will vary because it is a product of the material deformation and the material stiffness. The second phase, cutting, starts just after the rupture, the moment when the crack propagates in the material and the force on the needle suddenly drops. During the cutting phase, the force will stay
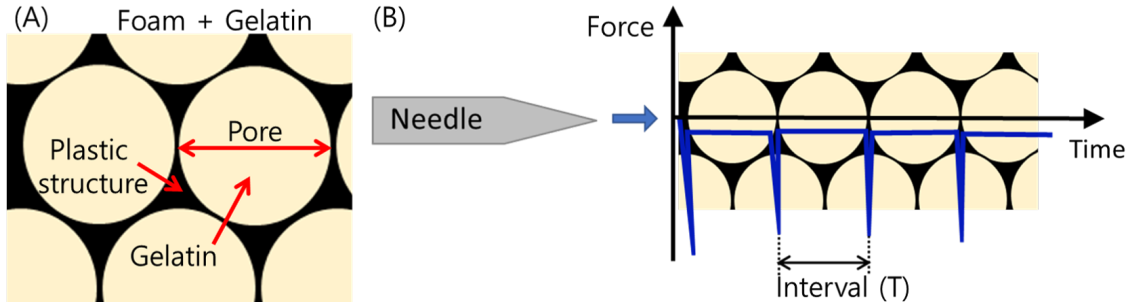
Figure 6.3: (A) When the polyurethane structures create the pores, the distance between the structures will be defined by the diameter of the pore. (B) The expected force profile while the needle tip is cutting through the structure.

at a relatively constant value.

(a)

(b)
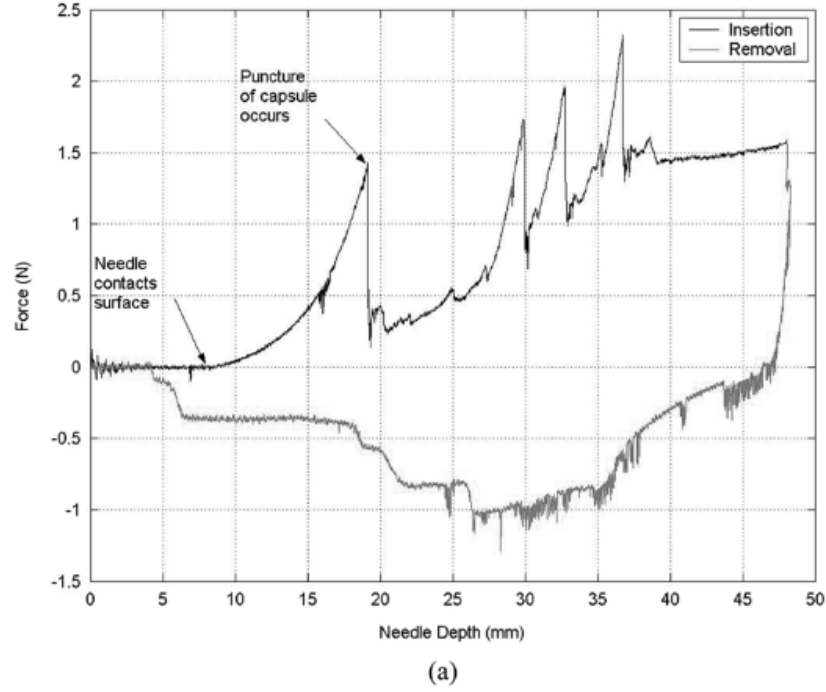
Figure 6.4: Reprinted from ©2004 IEEE [8]. (a)The cutting force increases as the tissue deforms and decreases rapidly after puncture (rupture) occurs. Needle axial forces measured during insertion into and removal from bovine liver. The main puncture event occurs at the capsule. (b) Additional puncture events occur due to collisions with internal structures such as those shown in this cut of liver.

It is expected to see a similar force profile from the axial force data of the bench-top test with polyurethane foams. The magnitude of axial needle force will increase while the
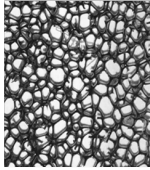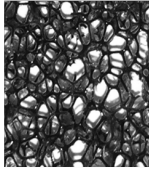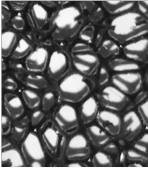
polyurethane structure deforms and it will drop rapidly after it ruptures (Figure 6.3 (B)). Although there will be some axial force due to the gelatin, it will be less noticeable because the polyurethane structure is considerably stiffer and tougher (the minimum polyurethane tensile strength is 8.7 MPa [120]). The fracture toughness of porcine gelatin is ≈ 32 kPa [121]. When the insertion speed is constant and known, the interval between two peak forces from the cutting can be estimated [64]:

$$T = \frac{d_{pore}}{v_{insertion}} \tag{6.1}$$

where T is the interval of the peaks, d_{pore} is the diameter of the pore, and $v_{insertion}$ is the constant insertion speed. The interval of force spikes represents the pore size (roughness) of the tissue phantom. Thus, if we can measure it, we will be able to estimate the tissue roughness.

To confirm this hypothesis, the needle was inserted into the tissue phantom with a constant speed, 6 mm/s. The expected interval was calculated based on the pore diameters and the insertion speed. Table 6.1 presents the expected interval and the frequency [64] of force spikes for each foam.

Table 6.1: The interval and the frequency of each foam

Foam type	Fine (30 ppi)	Middle (20 ppi)	Coarse (10 ppi)
Pore Diameter (d)	1.6 mm	2.4 mm	4.8mm
Expected Interval (T)	0.27 sec	0.4 sec	0.8 sec
Expected Frequency (1/T)	3.7 Hz	2.5 Hz	1.25 Hz

6.1.3 Tip-Force Data

A total of 30 insertion force trials were collected with 3 different tissue phantoms. Ten insertions were made for each phantom and the insertion depth (70 mm) was controlled to

be identical for all insertions. The sampling rate of the force sensing needle was 2 kHz.

The needle tip was located just inside of the phantom (5 mm from the top surface) prior to the beginning of the data collection process. After the data collection was initiated, the linear stage started to insert the needle. Data collection and needle insertion stopped after the linear stage reached the programmed insertion depth (70 mm). A few data points near the beginning and the end of insertion were excluded from analysis to minimize effects of stage acceleration and deceleration. The tip force data were recorded during insertion of the needle for each of the tissue phantoms. Figure 6.5 shows the tip force data of one insertion for each phantom (F_{sum} is the vector sum of F_x, F_y and F_z forces).

In Figure 6.5, we can see that the measured insertion force of the 30 ppi "fine" foam phantom has more frequent force fluctuations, which include small spikes, as compared to the middle (20 ppi) and the coarse (10 ppi) foams. In addition, we can see the small spikes and rapid changes in the radial forces at the same moment that the axial force changes (highlighted by the green boxes in Figure 6.5). The collected needle data were processed to estimate the tissue roughness of each phantoms.

6.2 Data Analysis

6.2.1 Frequency Domain Analysis

First, the data were analyzed in the frequency domain using the power spectral density analysis as in many previous investigations of surface roughness analysis. To avoid possible misinterpretation of frequency data, the insertion force data of pure gelatin was collected as a reference. There are a few components that show up in the power spectral density plot, including the frequency of the polyurethane structures, which we aimed to measure. Vibrations created by the moving linear stage and the sensor noise are also evident in the examples. These frequency noises can hinder differentiating the tissue roughness frequency from the PSD data. However, the PSD data of pure gelatin will include only the noises. By comparing with the gelatin force data, the unique frequency components of each phantom can be detected to estimate its tissue roughness. To obtain the PSD data, the built-in Signal Processing Toolbox of MATLAB (MathWorks, USA) was used. Figure 6.6 presents the PSD force data of different tissue phantoms.

In the previous section 6.1.2, the expected peak frequencies were calculated; 1.7 Hz, 2.5 Hz and 3.7 Hz for the coarse (10 ppi), middle (20 ppi) and fine foams (30 ppi) respectively.
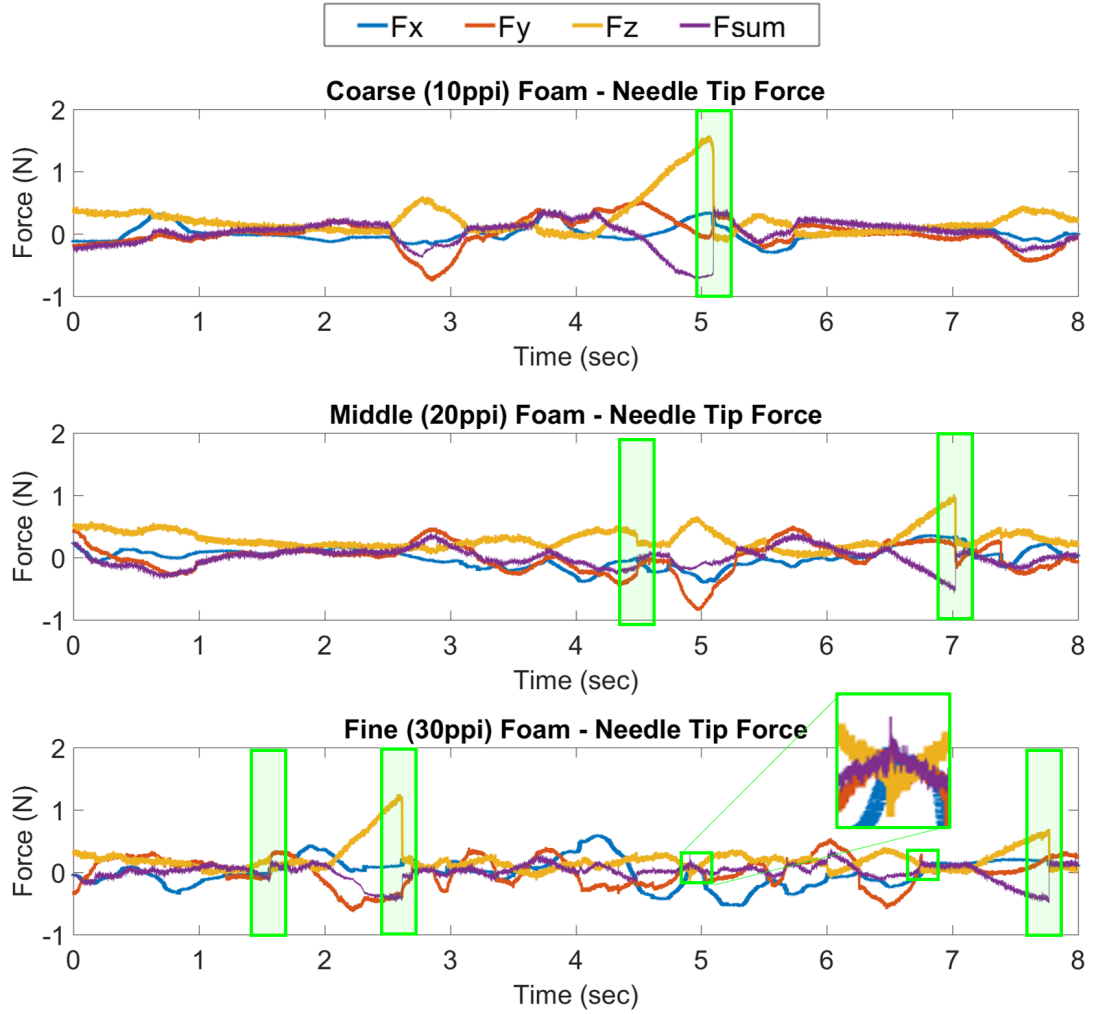
Figure 6.5: Eight seconds of recorded force data for each phantom. Needle insertion speed is 6 mm/s, which corresponds to 48 mm insertion depth. Green boxes highlight a few examples of sudden force changes.

The expected frequency range was 1.7 Hz to 3.7 Hz but a moderately large frequency range, 0 Hz to 20 Hz, was selected to anticipate the possible difference between the calculation and the measured data. However, all the data appear similar regardless of the tissue roughness. Even the pure gelatin data looks almost identical to the other phantoms' data, with the exception of slight differences found in F_x and F_z plots. Moreover, we could not find a distinctive peak in the expected frequency range (0 to 20 Hz). The full frequency range plot

showed a peak around $400\,\mathrm{Hz}$ however it was too large to be the tissue roughness. This result matches the vibration frequency of the insertion system and appears on the pure gelatin data as well as the other phantoms' data.
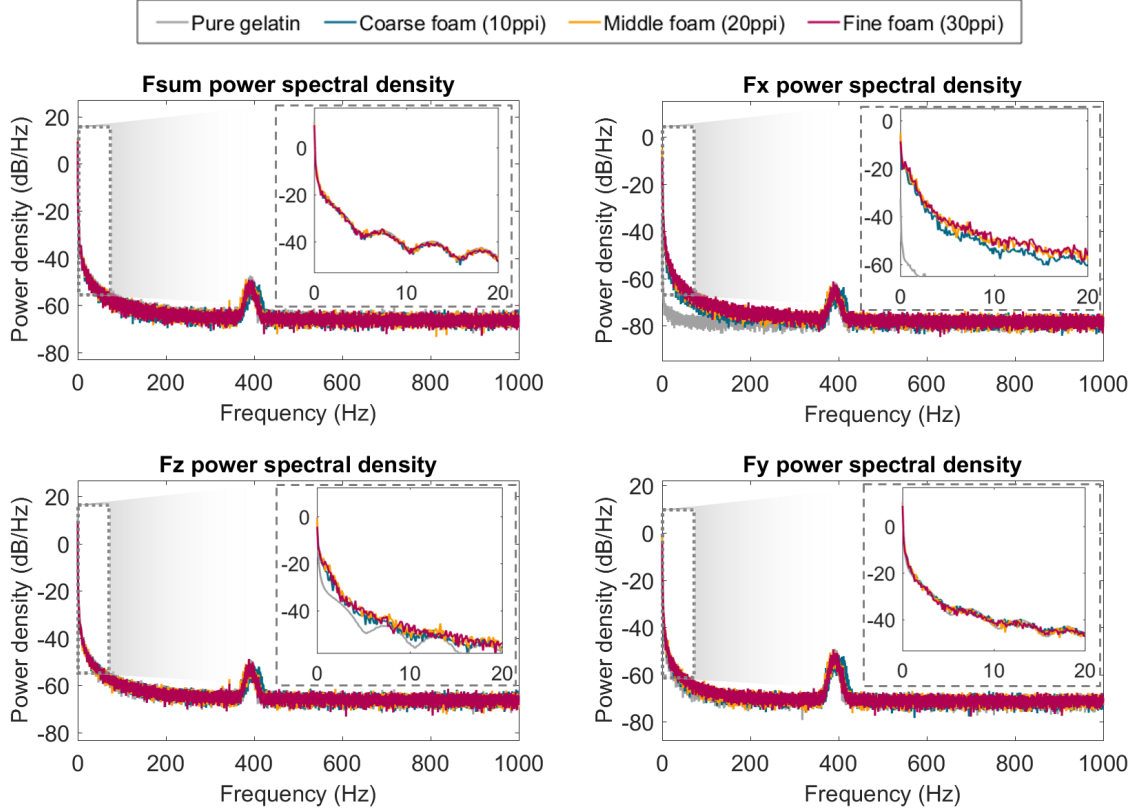
Figure 6.6: Power spectral density plots. Each of the plotted lines shows the average value of 10 insertion data collected with a corresponding tissue phantom.

In previous surface roughness sensing, the frequency domain analysis successfully extracts the roughness information from the force data [58,59,62,63]. However, in the present case it has poor performance. We suspect the main difference is that instead of dragging along a relatively hard surface, the needle is now embedded in a phantom, which remains in contact at all times. The needle only occasionally contacts a polyurethane wall, so that the corresponding events are at a very low frequency. In addition, the cutting (rupture) force varies substantially from cell to cell due to the random location and thickness of the foam. As a result of these observations we are motivated to try a different approach to distinguish the foams.

6.2.2   Result of Time Domain Analysis

Cutting the polyurethane foam structures creates a perceivable rough feeling during insertion. During the cutting process, the force increases before rupture and then suddenly drops. The sudden force changes are evident both in the the axial and radial forces because when the rupture happens, any forces at the tip will relax. Therefore, if we can detect the sudden changes of the forces, we should be able to find the spatial frequency (or period) of the foam structures. Furthermore, detecting rapid force changes will minimize any errors from the temperature because the temperature variation due to evaporation of water from the gel is slower (a few Hz or less).

The force data were processed with the following steps:

1. A zero phase delay high pass filter (cutoff $20\,\mathrm{Hz}$) was applied to remove potential temperature variation effects, and gradual force changes that we were not interested in measuring.

2. The standard deviation of the sensor noise was calculated to set a threshold to eliminate the high frequency sensor noise.

3. MATLAB's peak detection algorithm (findpeaks) was used to find the moments of the sudden force drops in F_x, F_y and F_z (Figure 6.7).

4. The average interval of the force drops was calculated.

The measured intervals for the different foams were close to the expected interval values (Figure 6.8). A Welch's ANOVA test confirmed that each foam was statistically different from others (95% confidence interval).

In conclusion, we found that time domain data analysis performed better than the frequency domain analysis for the tissue roughness estimation.

6.2.3   Effect of the Insertion Speed

To verify the time domain analysis, additional force data were collected at a different insertion speed, $2\,\mathrm{mm/s}$. Using the same foams and processing steps 10 insertion force data per phantom were recorded with $2\,\mathrm{kHz}$ sampling rate. The data for the two insertion speeds are compared in Table 6.2. As expected, the intervals for $2\,\mathrm{mm/s}$ are triple those of the $6\,\mathrm{mm/s}$ data.
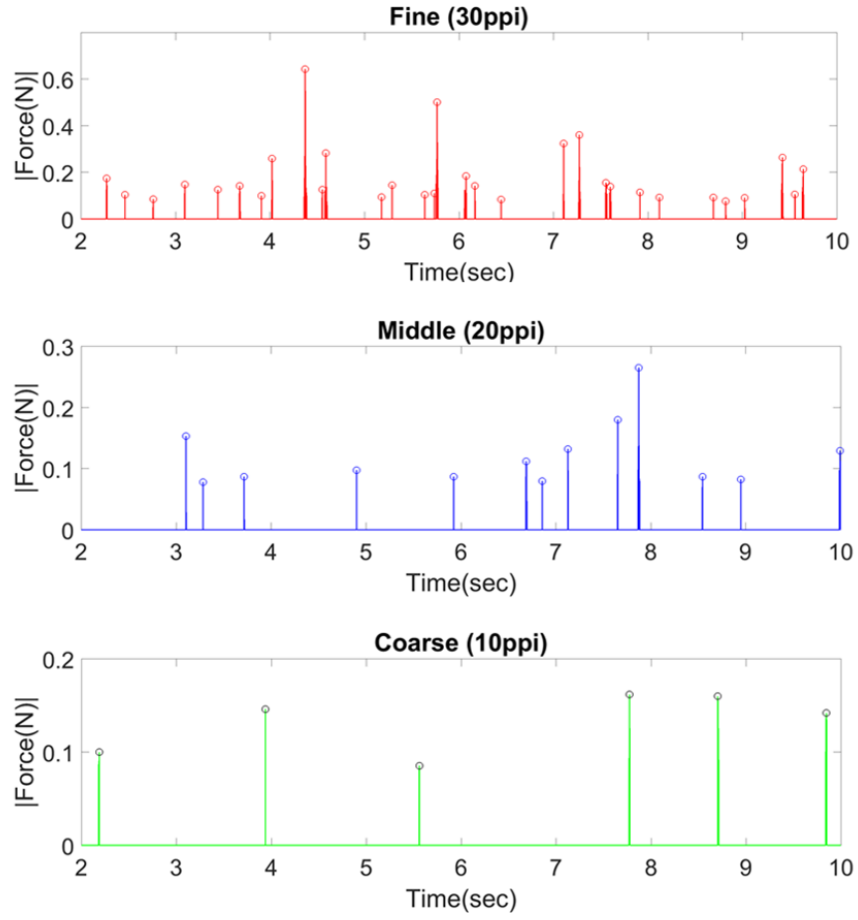
Figure 6.7: Detected peaks which represent sudden force drops.

Table 6.2: The spatial interval of the foam with two different insertion speed (N=10 for every condition).

		Fine (30ppi)	Middle (20ppi)	Coarse (10ppi)
Measured Interval (6 mm/s)	(Mean)	0.30 sec	0.41 sec	1.13 sec
	(SD)	0.07 sec	0.10 sec	0.74 sec
Expected Interval based on 6mm/s		**0.90 sec**	**1.23 sec**	**3.39 sec**
Measured Interval (2 mm/s)	(Mean)	1.13 sec	1.44 sec	3.07 sec
	(SD)	0.31 sec	0.37 sec	1.33 sec

Insertion speed: 6mm/s		Fine (30ppi)	Middle (20ppi)	Coarse (10ppi)
Expected Interval		0.27 sec	0.4 sec	0.8 sec
Measured Interval	(Mean)	0.30 sec	0.41 sec	1.13 sec
	(SD)	0.07 sec	0.10 sec	0.74 sec
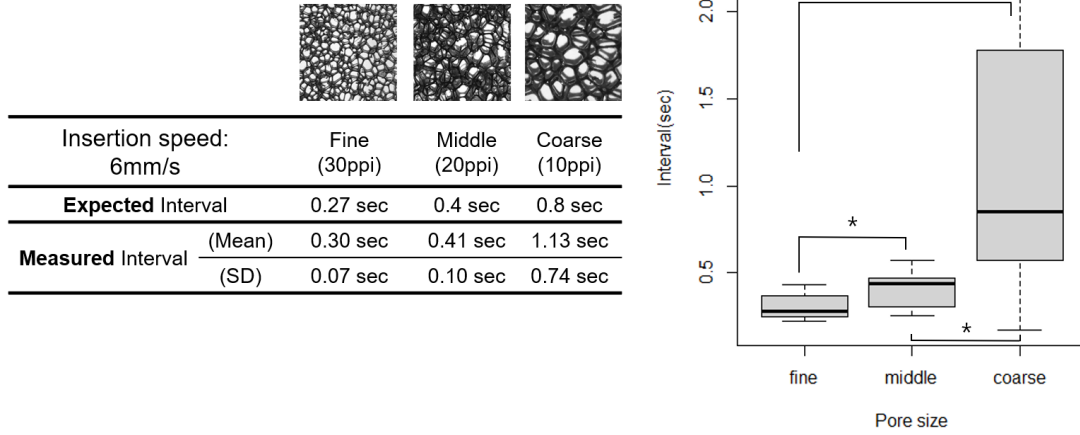
Figure 6.8: Texture classification result (N=10 for each tissue phantom).

6.3 Test with Fixed Liver Tissue Samples

The ultimate goal of tissue roughness sensing is to differentiate fibrotic/cirrhotic liver and healthy liver based on the needle insertion force data during a biopsy for expediting the diagnosis. Therefore, the tissue roughness sensing method was tested with more realistic test specimens, chemically fixed human liver samples.

6.3.1 Experimental Setup

The liver tissue samples were originally extracted for a pathology test following a liver transplant or surgery. The tissue was chemically "fixed" by formaldehyde for the pathological tests. The liver samples had already been tested at the pathology lab and were awaiting disposal. One healthy liver and one cirrhotic liver were used to collect the insertion force data.

As in the previous bench-top test, the linear stage pushed the needle into the liver tissue with a constant speed (1 mm/s). From the cross section of the tissue sample, the structure size of the extracellular matrix was approximated. As seen in Figure 6.9, while the cross section of the healthy liver sample looks smooth and uniform, the cirrhotic liver sample has micro structures that create circular patterns. The predicted force-drop interval of the cirrhotic liver sample was a few seconds for an insertion speed of 1 mm/s.
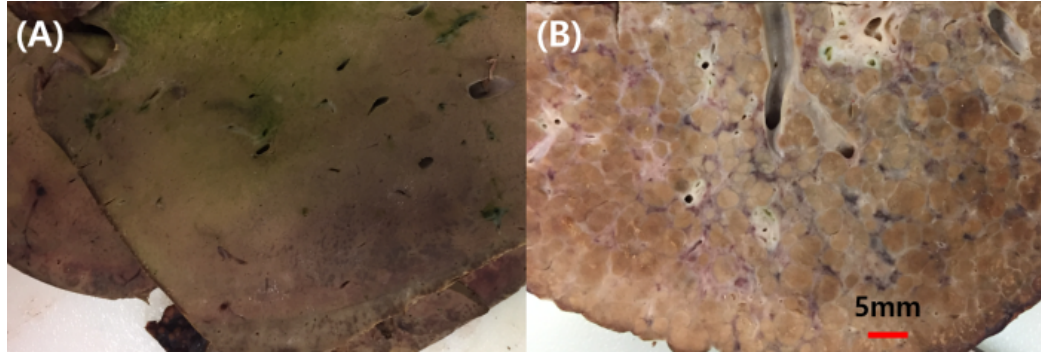
Figure 6.9: Cross section of the liver tissue samples. (A) healthy liver tissue sample, (B) cirrhotic liver tissue sample.

To hold the liver sample, an acrylic plate and a plastic plate with small bumps were used. The bottom plate was attached to a laboratory positioning stage which was clamped to the table as shown in Figure 6.10. Small clamps and the acrylic plate secured the liver tissue to the laboratory stage during the data collection. The insertion forces were recorded at several different locations across the liver sample. After the needle tip was located inside of the liver, the data collection and the insertion began. Total tip displacement inside of the liver was 45 mm. Four insertion data were collected for each tissue sample (healthy and cirrhotic).
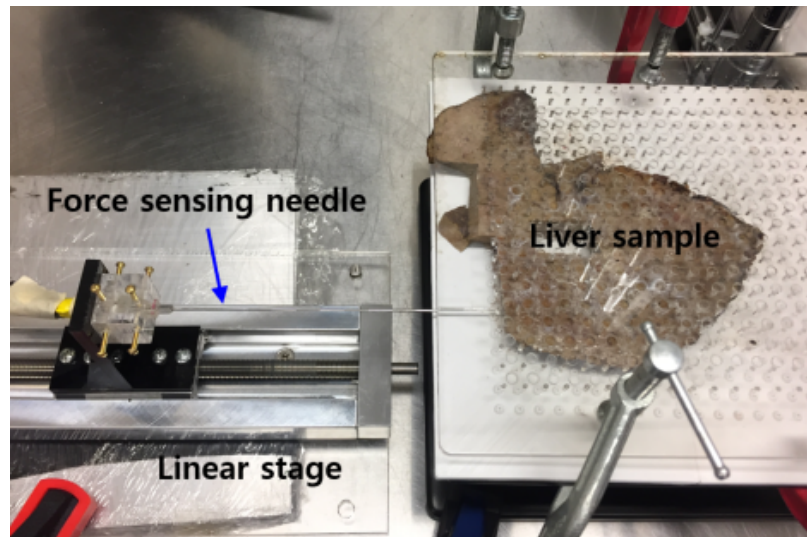
Figure 6.10: Testing setup to collect data with liver tissue samples.

6.3.2   Results

Figure 6.11 shows an example force profile of each liver sample. The forces in the cirrhotic liver sample plotted here change more frequently than in the healthy liver sample.
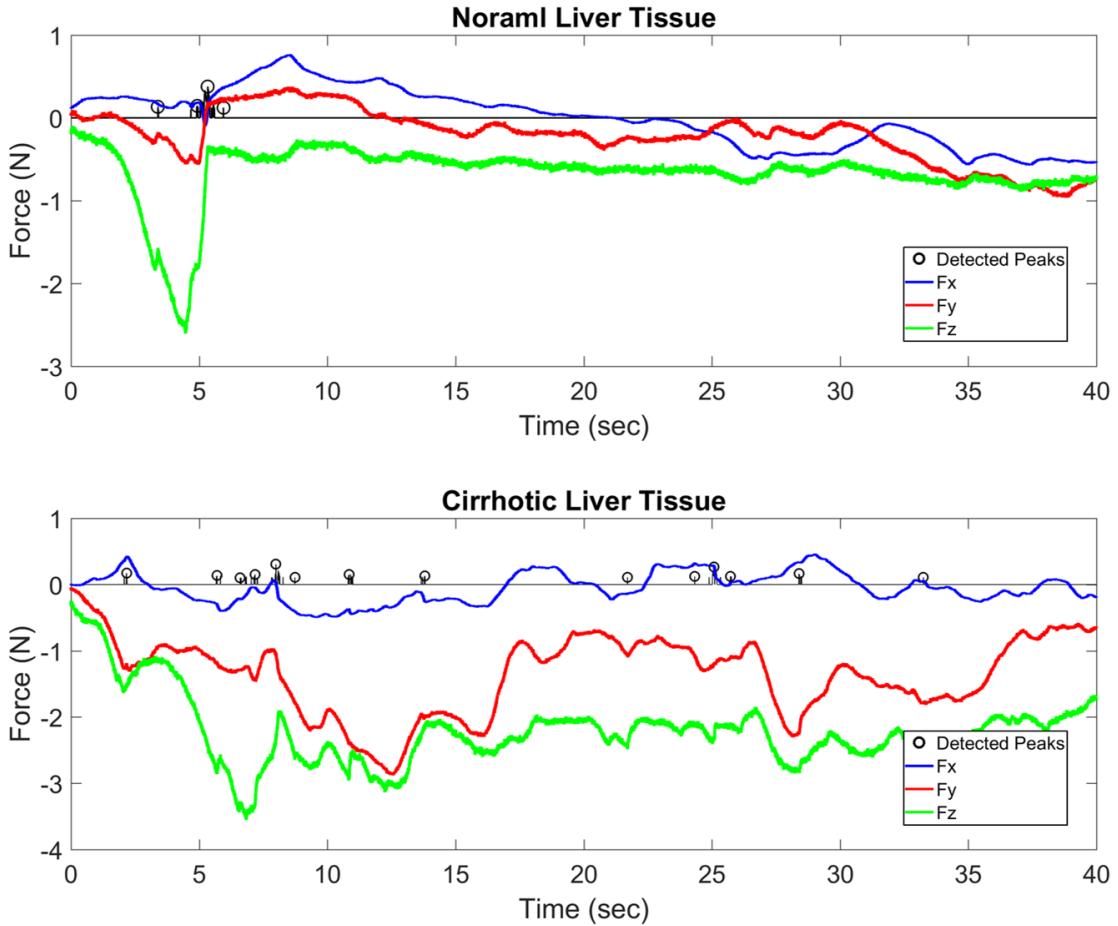
Figure 6.11: Insertion force plots of healthy and cirrhotic liver samples.

The intervals of force drops were measured for each sample and are represented in Figure 6.12. An unpaired t-test on the measured interval shows that the cirrhotic liver and the healthy liver were significantly different (95% interval, p-value was 0.0418).

When the insertion speed was $1\,\text{mm/s}$, the predicted extracellular structure size range was a few millimeters (Figure 6.9 (B)). The average structure size based the measured interval is around $6\,\text{mm}$ and it falls in the predicted range.

Group	Cirrhotic	Healthy
Mean	5.92 sec	20.78 sec
SD	2.01 sec	11.34 sec
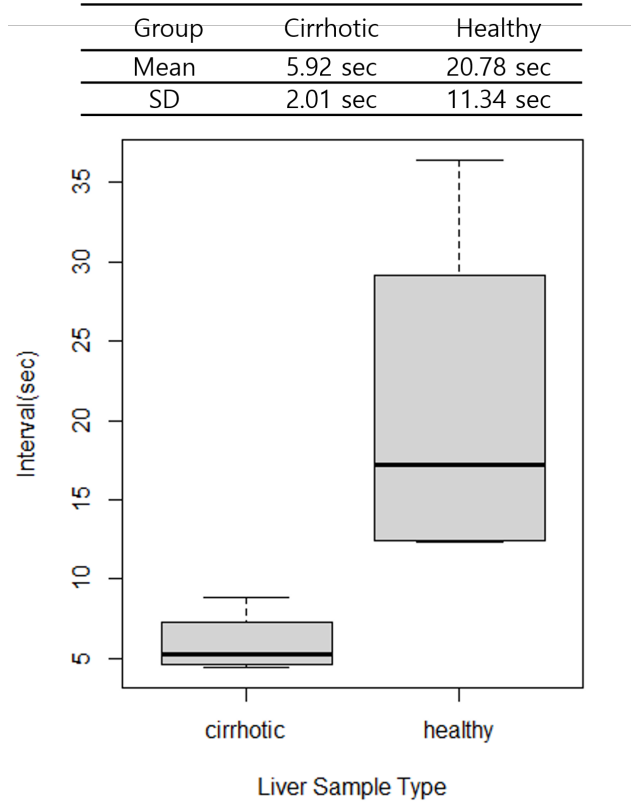
Figure 6.12: Average intervals of healthy and cirrhotic samples.

6.4 Conclusions and Future Work

We demonstrated the tissue roughness sensing is possible with a force sensing needle. Bench-top tests with prepared phantoms of gelatin and open cell polyurethane reveal a sensible difference as a needle is inserted through them. In contrast to much previous work on texture sensing in robotics, a frequency domain analysis of the signal was not effective for distinguishing among fine, medium and coarse foams. This result can in part be explained by the large variance in cutting forces and by the very low frequencies associated with forces ramping up and releasing as the needle encounters a cell wall of the foam. However, a time domain analysis method, which measures the interval of sudden force drops, gave us a good estimation of three different levels of tissue granularity or roughness. A Welch's ANOVA test confirmed that the roughness of the foams (10 ppi, 20 ppi and 30 ppi foams) can be differentiated based on the measured force-drop intervals. Accordingly, the same analysis

method was adopted to compare the roughness of the fixed human liver tissue samples for healthy and cirrhotic liver. The measured needle insertion forces of the cirrhotic liver indicated frequent force changes not found in the healthy liver. Further tests with unfixed liver tissue samples, and an insertion speed tracking system for manual biopsy, will be needed to adapt the tissue roughness sensing method for liver biopsy.

Chapter 7

Conclusions and Future Work

7.1 Summary of results

The objective of the work presented in this thesis is to develop components to permit MR-guided interventions with force sensing at the tool tip and haptic display at the physician's fingertips.

The first part of this system is an instrumented needle that can sense radial and axial forces at the needle tip, as well as bending deflections along the needle shaft. To create a force sensing needle we used optical fibers with Bragg gratings and a specially machined tip geometry to enhance the sensitivity to axial forces. With a commercial optical interrogator it is possible to sample the FBGs in the needle at 2 kHz or more, and to transmit sampled values with low latency, which is important for haptic display. A possible complication arises from the sensitivity of the FBGs to changes in temperature, but this can be addressed by calibration and by recognizing that thermal effects tend to be slow whereas the changes in force that accompany events of interest, such as membrane puncture, are considerably faster. An advantage to sensing forces at the tip of the needle is that the distal mass is low and the forces are not masked by inertia of the needle or friction along the needle shaft. In tests, the needle is capable of measuring forces as small as 8 mN in the axial direction and 4 mN in the radial direction.

For displaying the needle tip forces to a physician there are several options including visual, audio and haptic modalities. In this thesis we examined two kinds of haptic displays for the radial and axial forces, respectively.

The display of radial forces can compensate for the bending of a needle as a physician is

attempting to reach a target. For procedures like transperineal biopsy there is less incentive to transmit axial forces because a passive teleoperator (e.g. [67]) can be relatively stiff in the axial direction. A two DoF skin deformation haptic device was developed to map radial (x, y) forces at the needle tip to small skin deformations at the fingertips. With such a display users were able to target the center of a small movable proxy for a tumor more quickly and consistently than without haptic feedback.

A second haptic feedback device was developed to explore the display of axial needle tip forces. Such forces can be useful for determining when, for example, the needle has contacted or punctured a membrane or entered a region of tissue with noticeably different properties. Initial tests with a non-MR compatible haptic display demonstrated that subjects could detect events such as membrane puncture and that the forces so displayed were unaffected by friction and inertial of the needle and its base. An MR-compatible axial force display was then developed. This device used electroactive polymer actuators (EAPs) to produce small skin deformations at a user's fingertips in a small, hand-held device. Tests were conducted for detecting membrane contact and puncture with an robotic paradigm and a teleoperated paradigm. In the former case, the needle was driven at a fixed speed into tissue and users to indicate when they detected a force displayed by the device. In the second case, users controlled the motion a master device and the needle was servoed to track their commands. In this scenario they were asked to stop forward motion when they detected a skin stretch stimulus consistent with membrane contact or puncture. In both cases, most users had no difficulty detecting and responding to the stimulus, with a success rate of approximately 98%. In the second case there was more subject-to-subject variability as subjects adopted differing insertion speeds. In summary, it appears that axial force display is promising for demanding clinical applications which require puncturing of a small vessel or a tissue (e.g. prostate).

The ability of the needle to measure dynamic forces also suggests that it could provide information about tissue granularity or roughness. Tests were conducted with prepared tissue phantoms and with healthy and cirrhotic liver tissue to evaluate this capability. Although frequency domain analysis of the needle data was not successful, time domain analysis of spikes showed a reliable correlation with the spatial variation of tissue stiffness and rupture events. In future applications, this tissue roughness sensing could help physicians confirm the locations of healthy and diseased tissue while inserting a needle.

7.2 Conclusion

In conclusion, components of a haptic feedback system have been developed in support of teleoperated MR-guided needle interventions. The thesis demonstrates how the performance of interventions under MR-imaging could be improved by having haptic feedback based on forces measured by an optically-instrumented needle. The potential benefits include:

- reducing the duration of procedures and reducing possible tissue damage from repeated needle insertions;

- increasing the performance of targeting task regardless of the user's dexterity and experience level;

- locating the needle tip precisely in small cavities such as a blood vessel or in a tumor;

- confirming locations of diseased tissue with non-homogeneous properties.

Further system validation through animal tests and clinical trials should be conducted. The expected equipment costs are modest, and can be estimated based on those associated with the prototypes used in this thesis. The current cost of an 18 gage force sensing needle is around 1000 USD. The majority of this cost is spent on EDM micro-machining of grooves and holes at the tip. If producing the needle in quantity, the grooves could be made using extrusion and the distal holes could be made by laser machining or EDM at low cost using fixtures to minimize setup time. The optical fibers with FBGs cost approximately 120 USD in small quantities, but this cost too should drop rapidly with manufacturing volume. Ultimately the needle should cost no more than a few hundred dollars at current prices.

The optical interrogator is expensive ($\approx$ 20,000 USD) but this cost is amortized over many procedures and is very low compared to the cost of the MR machine. Advances in optical interrogator technology promise to shrink the size to a few hundred cubic centimeters while shrinking costs as well. Researchers recently developed a small, low-cost optical interrogator whose sampling rate is few kilohertz [122, 123].

The haptic device is expected to cost no more than a few hundred USD. For the radial display, the most expensive component is the ultrasonic motors which cost approximately 200 USD. For the EAP devices, the high voltage supply costs approximately 240 USD. Other parts (e.g. Linux computer) are inexpensive.

7.3 Future Work

7.3.1 Temperature Compensation

The force sensing needle is sensitive to both mechanical strains and temperature. Although the asymmetric tip design helps to distinguish axial strains from temperature, additional compensation is needed. Techniques included subtracting low pass filtered data, which contains slow temperature fluctuations. Additional methods could include using an extra FBG sensor purely for temperature compensation. For example, Figure 7.1 (A) shows a needle prototype with an additional FBG sensor at the center of the needle. Two titanium grade 2 tubes comprised the shaft of the needle. Grooves were machined by wire EDM, and the tip of the needle (MP35N alloy) was machined for assembly with the tubes. The inner tube diameter was $250\,\mu$m and the diameter of the temperature sensing FBG fiber
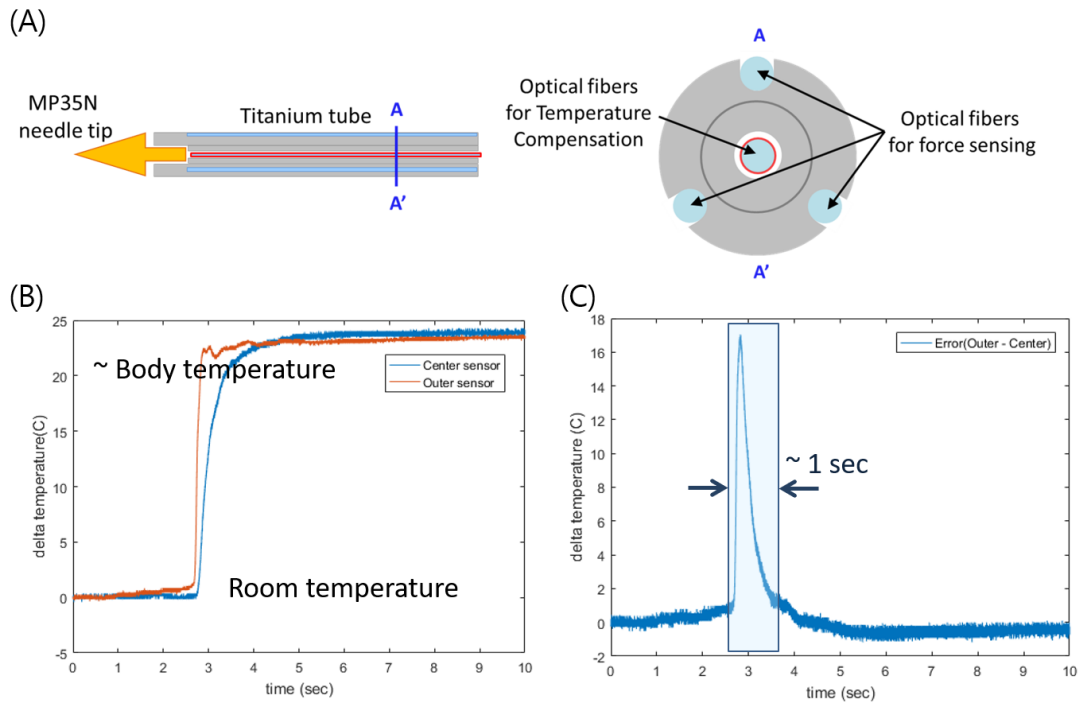
Figure 7.1: (A) Needle design for locating an extra temperature FBG sensor at the center of the needle. (B) The temperature measured by the extra temperature FBG sensor and the FBG sensors located at the grooves. (C) The temperature difference between two locations (the center of the tube and the outer grooves). Due to the delay, a large temperature peak can be seen.

was $180\,\mu$m. The temperature sensing FBG fiber was fixed only to the base of the needle to isolate it from mechanical strain. Assuming the temperature in the interior of the needle and at the periphery is nearly the same, this FBG can provide temperature compensation. However, there is some delay in reaching thermal equilibrium (Figure 7.1 (C)). Several types of filler including water, a silicone Heat Sink Compound, and galinstan (liquid metal) were injected inside the needle to try to reduce the thermal delay. However, unless moving a needle very slowly, it is preferable simply to high-pass filter the needle FBG data to obtain force information.

A second possible compensation method is based on adding a new feature near the needle tip which decouples the axial force response and the temperature response into different sensor variables, namely the width and the center wavelength of peak spectrum. The center wavelength of the peak spectrum shifts when magnitude changes associated with the axial strain are uniform over the FBG sensor length. On the other hand, the width of the peak spectrum changes when the magnitude changes are different [124]. FEA results show that the new design can create different axial strain changes over the length of an FBG sensor to associate the width of the peak spectrum with axial force and the center wavelength with temperature. Figure 7.2 explains the idea. To test this temperature compensation strategy, we will need a new optical interrogator that measures the width of a reflected wavelength peak with a fast sampling rate.

7.3.2 Haptic Feedback devices

Radial force display

To prevent misreading the cues associated with movement of the haptic knob, we adopted the protocol of displaying the direction necessary to reduce error. It is possible that users experienced in needle procedures would interpret the information differently, especially when manipulating the needle in three dimensions instead of a planar setup. Another possibility is to display both axial and radial forces in a new 3-DOF device.

Additional improvements can be made to the haptic guidance algorithm, and the three-dimensional system should be tested on tumors in tissue, instead of pivoting cylindrical phantom.
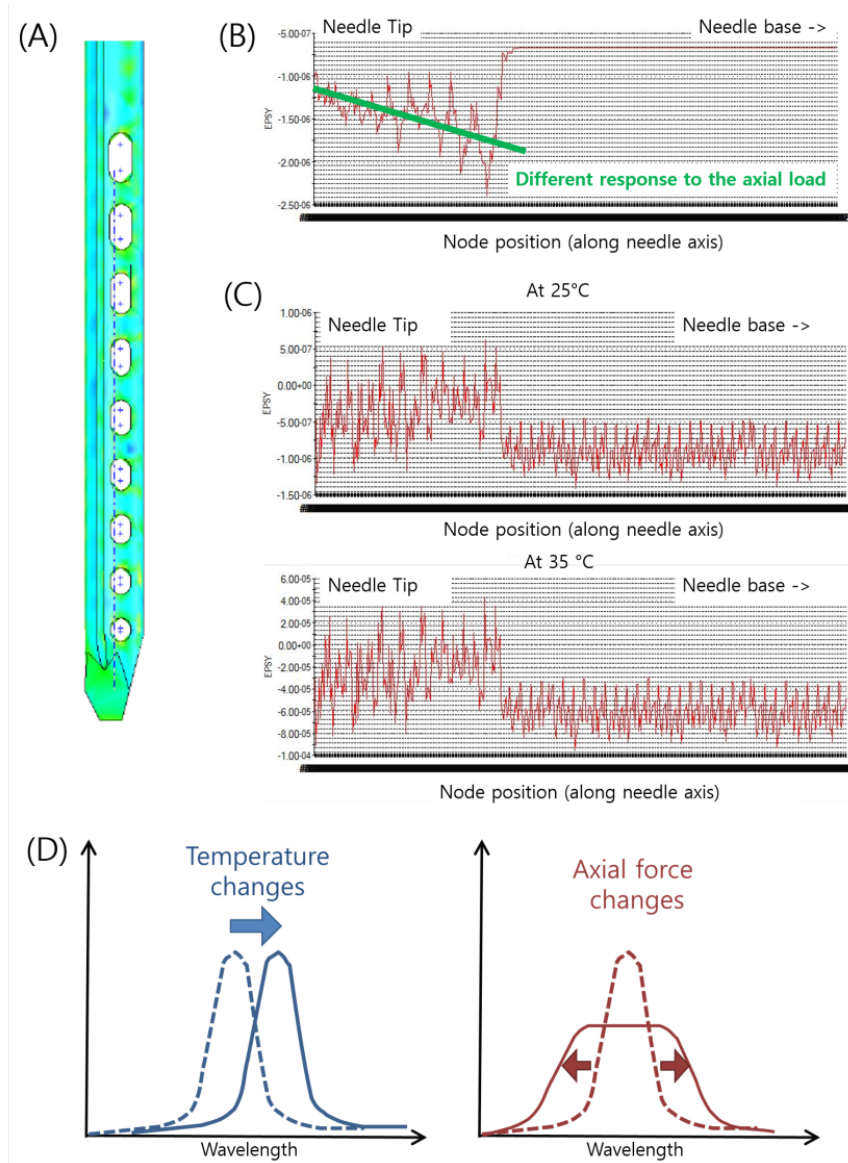
Figure 7.2: (A) Suggested needle design for separating the axial force and the temperature. (B) Axial strain plot when the 0.1N of axial force was applied at the tip. (C) Axial strain plot when the temperature was changed. (D)Expected behaviors of the FBG wavelength spectrum for the temperature changes and the axial force changes.

Axial Force Display

The prestretched amount of the EAP elastomer depends on its thickness and the need to generate adequate Maxwell stresses for deforming fingertips. Because of the original

thickness of the VHB film employed, a large amount of prestretch was required, which makes the film susceptible to tearing. A thinner elastomer, ideally with a higher dielectric constant, would overcome this problem. In addition, a material with less viscoelastic behavior will allow us to display faster force changes. The size of haptic device can also be reduced by developing a multilayer EAP film, instead of stretching several separate films within a frame.

7.3.3 Texture Sensing

Further examination of texture should include tests with liver samples having different levels of fibrosis, for cross-validation with pathology test results. One challenge will be to display the liver texture haptically, as this will require a higher bandwidth than the current EAP actuator achieves or a new actuator that can display faster signal changes. In other work, Culbertson et al. [125] studied the display of realistic surface textures arising from tool/surface interactions; an analogous model could be applied to needle/tissue interactions to provide a realistic feeling of tissue texture as a function of speed, needle tip shape, etc.

Bibliography

[1] Hao Su and Gregory S. Fischer. A 3-axis optical force/torque sensor for prostate needle placement in Magnetic resonance imaging environments. In *IEEE International Conference on Technologies for Practical Robot Applications*, pages 5–9, 2009.

[2] Andy Gijbels, Emmanuel B Vander Poorten, Peter Stalmans, and Dominiek Reynaerts. Development and experimental validation of a force sensing needle for robotically assisted retinal vein cannulations. In *IEEE International Conference on Robotics and Automation (ICRA)*, pages 2270–2276. IEEE, 2015.

[3] Yong-Lae Park, Santhi Elayaperumal, Bruce Daniel, Seok Chang Ryu, Mihye Shin, Joan Savall, Richard J Black, Behzad Moslehi, and Mark R Cutkosky. Real-time estimation of 3-d needle shape and deflection for mri-guided interventions. *IEEE/ASME Transactions On Mechatronics*, 15(6):906–915, 2010.

[4] Brian T Gleeson, Scott K Horschel, and William R Provancher. Perception of direction for applied tangential skin displacement: Effects of speed, displacement, and repetition. *IEEE Transactions on Haptics*, 3(3):177–188, 2010.

[5] Sukanya Basu, Jeremy Tsai, and Ann Majewicz. Evaluation of tactile guidance cue mappings for emergency percutaneous needle insertion. In *IEEE Haptics Symposium (HAPTICS)*, pages 106–112. IEEE, 2016.

[6] Carlos Rossa, Jason Fong, Nawaid Usmani, Ronald Sloboda, and Mahdi Tavakoli. Multiactuator haptic feedback on the wrist for needle steering guidance in brachytherapy. *IEEE Robotics and Automation Letters*, 1(2):852–859, 2016.

[7] Sanne Skovgård Veidal, Morten Asser Karsdal, Efstathios Vassiliadis, Arkadiusz Nawrocki, Martin Røssel Larsen, Quoc Hai Trieu Nguyen, Per Hägglund, Yunyun

Luo, Qinlong Zheng, Ben Vainer, et al. MMP mediated degradation of type VI collagen is highly associated with liver fibrosis–identification and validation of a novel biochemical marker assay. *PLoS One*, 6(9):e24753, 2011.

[8] Allison M Okamura, Christina Simone, and Mark D O'leary. Force modeling for needle insertion into soft tissue. *IEEE Transactions on Biomedical Engineering*, 51(10):1707–1716, 2004.

[9] Wenfeng Xia, Jean Martial Mari, Simeon J West, Yuval Ginsberg, Anna L David, Sebastien Ourselin, and Adrien E Desjardins. In-plane ultrasonic needle tracking using a fiber-optic hydrophone. *Medical Physics*, 42(10):5983–5991, 2015.

[10] Jay Mung, Francois Vignon, and Ameet Jain. A non-disruptive technology for robust 3D tool tracking for ultrasound-guided interventions. In *International Conference on Medical Image Computing and Computer-Assisted Intervention*, pages 153–160. Springer, 2011.

[11] Troy K Adebar and Allison M Okamura. 3D segmentation of curved needles using doppler ultrasound and vibration. In *International Conference on Information Processing in Computer-Assisted Interventions*, pages 61–70. Springer, 2013.

[12] Leonard Marks, Shelena Young, and Shyam Natarajan. MRI–ultrasound fusion for guidance of targeted prostate biopsy. *Current Opinion in Urology*, 23(1):43, 2013.

[13] Brian K Rutt and Donald H Lee. The impact of field strength on image quality in MRI. *Journal of Magnetic Resonance Imaging*, 6(1):57–62, 1996.

[14] Santhi Elayaperumal, Jung Hwa Bae, David Christensen, Mark R Cutkosky, Bruce L Daniel, Richard J Black, and Joannes M Costa. MR-compatible biopsy needle with enhanced tip force sensing. In *IEEE World Haptics Conference (WHC)*, pages 109–114, 2013.

[15] Santhi Elayaperumal, Jung Hwa Bae, Bruce L. Daniel, and Mark R. Cutkosky. Detection of membrane puncture with haptic feedback using a tip-force sensing needle. In *IEEE International Conference on Intelligent Robots and Systems (IROS)*, pages 3975–3981, 2014.

[16] Jung Hwa Bae, Christopher J. Ploch, Michael A. Lin, Bruce L. Daniel, and Mark R. Cutkosky. Display of needle tip contact forces for steering guidance. In *IEEE Haptics Symposium (HAPTICS)*, volume 2016-April, pages 332–337, 2016.

[17] Jung Hwa Bae, Amy Kyungwon Han, Chris J. Ploch, Bruce L. Daniel, and Mark R. Cutkosky. Haptic feedback of membrane puncture with an MR-compatible instrumented needle and electroactive polymer display. In *IEEE World Haptics Conference (WHC)*, pages 54–59, 2017.

[18] Amy K. Han, Jung Hwa Bae, Roser E. Gregoriou Katerina C.and Ploch, Chris J.and Goldman, Bruce L. Glover, Glove H.and Daniel, and Mark R. Cutkosky. MR-Compatible Haptic Display of Membrane Puncture in Robot-Assisted Needle Procedures. *IEEE Transactions on Haptics*, 2018.

[19] Reza Seifabadi, Sang-Eun Song, Axel Krieger, Nathan Bongjoon Cho, Junichi Tokuda, Gabor Fichtinger, and Iulian Iordachita. Robotic system for MRI-guided prostate biopsy: feasibility of teleoperated needle insertion and ex vivo phantom study. *International Journal of Computer Assisted Radiology and Surgery*, 7(2):181–190, 2012.

[20] Santhi Elayaperumal, Juan Camilo Plata, Andrew B. Holbrook, Yong Lae Park, Kim Butts Pauly, Bruce L. Daniel, and Mark R. Cutkosky. Autonomous real-time interventional scan plane control with a 3-d shape-sensing needle. *IEEE Transactions on Medical Imaging*, 33(11):2128–2139, 2014.

[21] G S Fischer, I Iordachita, C Csoma, J Tokuda, S P Dimaio, C M Tempany, N Hata, and G Fichtinger. MRI-Compatible Pneumatic Robot for Transperineal Prostate Needle Placement. *IEEE-ASME T Mech*, 13:295–305, 2008.

[22] Sang Eun Song, Nathan B. Cho, Gregory Fischer, Nobuhito Hata, Clare Tempany, Gabor Fichtinger, and Iulian Iordachita. Development of a pneumatic robot for MRI-guided transperineal prostate biopsy and brachytherapy: New approaches. In *IEEE International Conference on Robotics and Automation (ICRA)*, pages 2580–2585, 2010.

[23] Hao Su, Weijian Shang, Gang Li, Niravkumar Patel, and Gregory S Fischer. An MRI-Guided Telesurgery System Using a Fabry-Perot Interferometry Force Sensor and a Pneumatic Haptic Device. *Annals of Biomedical Engineering*, pages 1–12, 2017.

[24] Natalie Burkhard, Samuel Frishman, Alexander Gruebele, J Peter Whitney, Roger Goldman, Bruce Daniel, and Mark Cutkosky. A rolling-diaphragm hydrostatic transmission for remote mr-guided needle insertion. In *IEEE International Conference on Robotics and Automation (ICRA)*, pages 1148–1153, 2017.

[25] Rebecca Kokes, Kevin Lister, Rao Gullapalli, Bao Zhang, Alan Macmillan, Howard Richard, and Jaydev P Desai. Towards a teleoperated needle driver robot with haptic feedback for RFA of breast tumors under continuous MRI. *Medical Image Analysis*, 13(3):445–455, 2009.

[26] Bo Yang, U-Xuan Tan, Alan B McMillan, Rao Gullapalli, and Jaydev P Desai. Design and control of a 1-DOF MRI-compatible pneumatically actuated robot with long transmission lines. *IEEE/ASME Transactions on Mechatronics*, 16(6):1040–1048, 2011.

[27] Christoforos Keroglou, Nikolaos V Tsekos, Ioannis Seimenis, Eleni Eracleous, Christodoulos G Christodoulou, Constantinos Pitris, and Eftychios G Christoforou. Design of MR-compatible robotic devices: magnetic and geometric compatibility aspects. In *International Conference on Information Technology and Applications in Biomedicine*, pages 1–4, 2009.

[28] Uikyum Kim, Dong-Hyuk Lee, Woon Jong Yoon, Blake Hannaford, and Hyouk Ryeol Choi. Force sensor integrated surgical forceps for minimally invasive robotic surgery. *IEEE Transactions on Robotics*, 31(5):1214–1224, 2015.

[29] J Dargahi, M Parameswaran, and S Payandeh. A micromachined piezoelectric tactile sensor for an endoscopic grasper-theory, fabrication and experiments. *Journal of Microelectromechanical Systems*, 9(3):329–335, 2000.

[30] Jan Peirs, Joeri Clijnen, Dominiek Reynaerts, Hendrik Van Brussel, Paul Herijgers, Brecht Corteville, and Sarah Boone. A micro optical force sensor for force feedback during minimally invasive robotic surgery. *Sensors and Actuators A: Physical*, 115(2-3):447–455, 2004.

[31] Christoph Ledermann, Jan Hergenhan, Oliver Weede, and Heinz Woern. Combining shape sensor and haptic sensors for highly flexible single port system using Fiber

Bragg sensor technology. In *IEEE/ASME International Conference on Mechatronic and Embedded Systems and Applications (MESA)*, pages 196–201, 2012.

[32] Roberto Blanco Sequeiros, Risto Ojala, Juho Kariniemi, Jukka Perälä, Jaakko Niinimäki, Heli Reinikainen, and Osmo Tervonen. MR-guided interventional procedures: a review. *Acta Radiologica*, 46(6):576–586, 2005.

[33] Danilo De Lorenzo, Yoshihiko Koseki, Elena De Momi, Kiyoyuki Chinzei, and Allison M Okamura. Coaxial needle insertion assistant with enhanced force feedback. *IEEE Transactions on Biomedical Engineering*, 60(2):379–389, 2013.

[34] Hao Su, Michael Zervas, Cosme Furlong, and Gregory S Fischer. A miniature mri-compatible fiber-optic force sensor utilizing fabry-perot interferometer. In *MEMS and Nanotechnology, Volume 4*, pages 131–136. Springer, 2011.

[35] Iulian Iordachita, Zhenglong Sun, Marcin Balicki, Jin U Kang, Soo Jay Phee, James Handa, Peter Gehlbach, and Russell Taylor. A sub-millimetric, 0.25 mn resolution fully integrated fiber-optic force-sensing tool for retinal microsurgery. *International Journal of Computer Assisted Radiology and Surgery*, 4(4):383–390, 2009.

[36] KR Henken. *Smart needles for percutaneous interventions*. PhD thesis, TU Delft, 2014.

[37] Ingvars Birznieks. *Tactile sensory control of dexterous manipulation in humans*. PhD thesis, Integrativ medicinsk biologi, 2003.

[38] Roland S. Johansson and J. Randall Flanagan. Coding and use of tactile signals from the fingertips in object manipulation tasks. *Nature Reviews: Neuroscience*, 10(5):345–359, May 2009.

[39] Carol E Reiley, Takintope Akinbiyi, Darius Burschka, David C Chang, Allison M Okamura, and David D Yuh. Effects of visual force feedback on robot-assisted surgical task performance. *The Journal of Thoracic and Cardiovascular Surgery*, 135(1):196–202, 2008.

[40] James C Gwilliam, Mohsen Mahvash, Balazs Vagvolgyi, Alexander Vacharat, David D Yuh, and Allison M Okamura. Effects of haptic and graphical force feedback on tele-operated palpation. In *IEEE International Conference on Robotics and Automation (ICRA)*, pages 677–682, 2009.

[41] Nathan Cutler, Marcin Balicki, Mark Finkelstein, Jiangxia Wang, Peter Gehlbach, John McGready, Iulian Iordachita, Russell Taylor, and James T Handa. Auditory force feedback substitution improves surgical precision during simulated ophthalmic surgery. *Investigative Ophthalmology & Visual Science*, 54(2):1316–1324, 2013.

[42] Roland S Johansson and J Randall Flanagan. Coding and use of tactile signals from the fingertips in object manipulation tasks. *Nature Reviews Neuroscience*, 10(5):345, 2009.

[43] Susan J Lederman and Roberta L Klatzky. Haptic perception: A tutorial. *Attention, Perception, & Psychophysics*, 71(7):1439–1459, 2009.

[44] G Westling and Roland S Johansson. Responses in glabrous skin mechanoreceptors during precision grip in humans. *Experimental Brain Research*, 66(1):128–140, 1987.

[45] Håkan Olausson, Johan Wessberg, and Naoyuki Kakuda. Tactile directional sensibility: peripheral neural mechanisms in man. *Brain Research*, 866(1-2):178–187, 2000.

[46] Karlin Bark, Jason Wheeler, Pete Shull, Joan Savall, and Mark Cutkosky. Rotational skin stretch feedback: A wearable haptic display for motion. *IEEE Transactions on Haptics*, 3(3):166–176, 2010.

[47] Brian T Gleeson, Scott K Horschel, and William R Provancher. Communication of direction through lateral skin stretch at the fingertip. In *IEEE Euro Haptics Conference*, pages 172–177, 2009.

[48] Nathan Medeiros-Ward, Joel M Cooper, Andrew J Doxon, David L Strayer, and William R Provancher. Bypassing the bottleneck: The advantage of fingertip shear feedback for navigational cues. In *Proceedings of the Human Factors and Ergonomics Society Annual Meeting*, volume 54, pages 2042–2047, 2010.

[49] Zhan Fan Quek, Samuel B Schorr, Ilana Nisky, Allison M Okamura, and William R Provancher. Sensory augmentation of stiffness using fingerpad skin stretch. In *IEEE World Haptics Conference (WHC)*, pages 467–472. IEEE, 2013.

[50] Brian T Gleeson, Charles A Stewart, and William R Provancher. Improved tactile shear feedback: Tactor design and an aperture-based restraint. *IEEE Transactions on Haptics*, 4(4):253–262, 2011.

[51] William Provancher. Creating greater vr immersion by emulating force feedback with ungrounded tactile feedback. *IQT Quarterly*, 6(2):18–21, 2014.

[52] Samuel B Schorr, Zhan Fan Quek, Ilana Nisky, William R Provancher, and Allison M Okamura. Tactor-induced skin stretch as a sensory substitution method in teleoperated palpation. *IEEE Transactions on Human-Machine Systems*, 45(6):714–726, 2015.

[53] Mohsen Mahvash and Pierre E Dupont. Fast needle insertion to minimize tissue deformation and damage. In *IEEE International Conference on Robotics and Automation (ICRA)*, pages 3097–3102, 2009.

[54] Shan Jiang, Pan Li, Yan Yu, Jun Liu, and Zhiyong Yang. Experimental study of needle–tissue interaction forces: effect of needle geometries, insertion methods and tissue characteristics. *Journal of Biomechanics*, 47(13):3344–3353, 2014.

[55] Mohsen Mahvash and Pierre E Dupont. Mechanics of dynamic needle insertion into a biological material. *IEEE Transactions on Biomedical Engineering*, 57(4):934–943, 2010.

[56] H Shirado and T Maeno. The relationship between texture and the tactile sense. In *Proc. JSME Robotics and Mechatronics Conference, 1A1-H-33*, 2004.

[57] Susan J Lederman and Roberta L Klatzky. Hand movements: A window into haptic object recognition. *Cognitive Psychology*, 19(3):342–368, 1987.

[58] Yuka Mukaibo, Hirokazu Shirado, Masashi Konyo, and Takashi Maeno. Development of a texture sensor emulating the tissue structure and perceptual mechanism of human fingers. In *IEEE International Conference on Robotics and Automation (ICRA)*, pages 2565–2570, 2005.

[59] Jeremy A Fishel and Gerald E Loeb. Bayesian exploration for intelligent identification of textures. *Frontiers in Neurorobotics*, 6:4, 2012.

[60] Koh Hosoda, Yasunori Tada, and Minoru Asada. Anthropomorphic robotic soft fingertip with randomly distributed receptors. *Robotics and Autonomous Systems*, 54(2):104–109, 2006.

[61] Philippe Giguere and Gregory Dudek. A simple tactile probe for surface identification by mobile robots. *IEEE Transactions on Robotics*, 27(3):534–544, 2011.

[62] Florian De Boissieu, Christelle Godin, Bernard Guilhamat, Dominique David, Christine Serviere, and Daniel Baudois. Tactile texture recognition with a 3-axial force mems integrated artificial finger. In *Robotics: Science and Systems*, pages 49–56, 2009.

[63] Nawid Jamali and Claude Sammut. Majority voting: Material classification by tactile sensing using surface texture. *IEEE Transactions on Robotics*, 27(3):508–521, 2011.

[64] Calogero M Oddo, Marco Controzzi, Lucia Beccai, Christian Cipriani, and Maria Chiara Carrozza. Roughness encoding for discrimination of surfaces in artificial active-touch. *IEEE Transactions on Robotics*, 27(3):522–533, 2011.

[65] Mitsuru Taniwaki, Takanori Hanada, and Naoki Sakurai. Device for acoustic measurement of food texture using a piezoelectric sensor. *Food Research International*, 39(10):1099–1105, 2006.

[66] Roy J Roesthuis, Marco Kemp, John J Van Den Dobbelsteen, and S Misra. Three-Dimensional Needle Shape Reconstruction Using an Array of Fiber Bragg Grating Sensors. *IEEE/ASME Transactions on Mechatronics (TMECH)*, pages 1–12, 2013.

[67] Santhi Elayaperumal, Mark R Cutkosky, Pierre Renaud, and Bruce L Daniel. A passive parallel master–slave mechanism for magnetic resonance imaging-guided interventions. *Journal of Medical Devices*, 9(1):011008, 2015.

[68] Brian Gleeson, Scott Horschel, and William Provancher. Design of a fingertip-mounted tactile display with tangential skin displacement feedback. *IEEE Transactions on Haptics*, 3(4):297–301, 2010.

[69] Brian T Gleeson, Scott K Horschel, and William R Provancher. Design of a fingertip-mounted tactile display with tangential skin displacement feedback. *IEEE Transactions on Haptics*, 3(4):297–301, 2010.

[70] Martin S Judenhofer, Ciprian Catana, Brian K Swann, Stefan B Siegel, Wulf-Ingo Jung, Robert E Nutt, Simon R Cherry, Claus D Claussen, and Bernd J Pichler. PET/MR Images Acquired with a Compact MR-compatible PET Detector in a 7-T Magnet. *Radiology*, 244(3):807–814, 2007.

[71] Haytham Elhawary, Aleksander Zivanovic, Marc Rea, Brian L Davies, Collin Besant, Ian Young, MU Lamperth, et al. A modular approach to MRI-compatible robotics. *IEEE Engineering in Medicine and Biology Magazine*, 27(3):35–41, 2008.

[72] Benjamin Maurin, Bernard Bayle, Jacques Gangloff, Philippe Zanne, Michel de Mathelin, and Olivier Piccin. A robotized positioning platform guided by computed tomography: Practical issues and evaluation. In *IEEE International Conference on Robotics and Automation (ICRA)*, pages 251–256, 2006.

[73] Andrew Erwin, Marcia K O'Malley, David Ress, and Fabrizio Sergi. Development, control, and MRI-compatibility of the MR-SoftWrist. In *IEEE International Conference on Rehabilitation Robotics (ICORR)*, pages 187–192. IEEE, 2015.

[74] Shin-ichi Furuya, Toru Maruhashi, Yuji Izuno, and Mutsuo Nakaoka. Load-adaptive frequency tracking control implementation of two-phase resonant inverter for ultrasonic motor. *IEEE Transactions on Power Electronics*, 7(3):542–550, 1992.

[75] Jörg Wallaschek. Contact mechanics of piezoelectric ultrasonic motors. *Smart Materials and Structures*, 7(3):369, 1998.

[76] Christopher M Esser, Chembian Parthiban, and Michael R Zinn. Development of a parallel actuation approach for MR-compatible robotics. *IEEE/ASME Transactions on Mechatronics*, 19(3):904–915, 2014.

[77] Tomonobu Senjyu, Tomohiro Yoshida, Katsumi Uezato, and Toshihisa Funabashi. Position control of ultrasonic motors using adaptive backstepping control and dead-zone compensation with fuzzy inference. In *IEEE International Conference on Industrial Technology (ICIT)*, volume 1, pages 560–565, 2002.

[78] Tomonobu Senjyu, Hiroshi Miyazato, Satoru Yokoda, and Katsumi Uezato. Speed control of ultrasonic motors using neural network. *IEEE Transactions on Power Electronics*, 13(3):381–387, 1998.

[79] Robert D Howe. Tactile sensing and control of robotic manipulation. *Advanced Robotics*, 8(3):245–261, 1993.

[80] Karlin Bark, William McMahan, Austin Remington, Jamie Gewirtz, Alexei Wedmid, David I Lee, and Katherine J Kuchenbecker. In vivo validation of a system for haptic feedback of tool vibrations in robotic surgery. *Surgical Endoscopy*, 27(2):656–664, 2013.

[81] Ingrid MLC Vogels. Detection of temporal delays in visual-haptic interfaces. *Human factors: The Journal of the Human Factors and Ergonomics Society*, 46(1):118–134, 2004.

[82] Andrew J Doxon, David E Johnson, Hong Z Tan, and William Provancher. Human detection and discrimination of tactile repeatability, mechanical backlash, and temporal delay in a combined tactile-kinesthetic haptic display system. *IEEE Transactions on Haptics*, 6(4):453–463, 2013.

[83] Vera Lagerburg, Marinus A Moerland, Jan JW Lagendijk, and Jan J Battermann. Measurement of prostate rotation during insertion of needles for brachytherapy. *Radiotherapy and Oncology*, 77(3):318–323, 2005.

[84] Nelson N Stone, Jiten Roy, Suzanne Hong, Yeh-Chi Lo, and Richard G Stock. Prostate gland motion and deformation caused by needle placement during brachytherapy. *Brachytherapy*, 1(3):154–160, 2002.

[85] Junru Wu. Tofu as a tissue-mimicking material. *Ultrasound in Medicine & Biology*, 27(9):1297–1300, 2001.

[86] Katherine J Kuchenbecker, Jamie Gewirtz, William McMahan, Dorsey Standish, Paul Martin, Jonathan Bohren, Pierre J Mendoza, and David I Lee. Verrotouch: high-frequency acceleration feedback for telerobotic surgery. In *Haptics: Generating and perceiving tangible sensations*, pages 189–196. Springer, 2010.

[87] Niki Abolhassani, Rajni Patel, and Mehrdad Moallem. Needle insertion into soft tissue: a survey. *Medical Engineering & Physics*, 29(4):413–31, May 2007.

[88] Tarun Podder, Douglas Clark, Jason Sherman, Dave Fuller, Edward Messing, Deborah Rubens, John Strang, Ralph Brasacchio, Lydia Liao, Wan-Sing Ng, and Yan Yu. In vivo motion and force measurement of surgical needle intervention during prostate brachytherapy. *Medical Physics*, 33(8):2915, 2006.

[89] Susan J Lederman and Roberta L Klatzky. Extracting object properties through haptic exploration. *Acta Psychologica*, 84(1):29–40, 1993.

[90] Weigang Zhang, Xiaoyi Dong, Qida Zhao, G. Kai, and Shuzhong Yuan. FBG-type sensor for simultaneous measurement of force (or displacement) and temperature based on bilateral cantilever beam. *IEEE Photonics Technology Letters*, 13(12):1340–1342, December 2001.

[91] S. T. Oh, W. T. Han, U. C. Paek, and Y. Chung. Discrimination of temperature and strain with a single FBG based on the birefringence effect. *OPTICS EXPRESS*, 12(4):724–729, 2004.

[92] Xuewen Shu, Yu Liu, Donghui Zhao, Bashir Gwandu, Filip Floreani, Lin Zhang, and Ian Bennion. Dependence of temperature and strain coefficients on fiber grating type and its application to simultaneous temperature and strain measurement. *Optics Letters*, 27(9):701, May 2002.

[93] Zion Tsz Ho Tse, Haytham Elhawary, Marc Rea, Brian Davies, Ian Young, and Michael Lamperth. Haptic needle unit for MR-guided biopsy and its control. *IEEE/ASME Transactions on Mechatronics*, 17(1):183–187, 2012.

[94] Mehmet Alper Ergin, Markus Kuhne, Axel Thielscher, and Angelika Peer. Design of a new MR-compatible haptic interface with six actuated degrees of freedom. *5th IEEE RAS/EMBS International Conference on Biomedical Robotics and Biomechatronics*, pages 293–300, 2014.

[95] Andrew Erwin, Marcia O'Malley, David Ress, and Fabrizio Sergi. Kinesthetic Feedback during 2DOF Wrist Movements via a Novel MR-Compatible Robot. *IEEE Transactions on Neural Systems and Rehabilitation Engineering*, pages 1489–1499, 2016.

[96] Masayuki Hara, Gatan Matthey, and Akio Yamamoto. Development of a 2-DOF Electrostatic Haptic Joystick for MRI/fMRI Applications. In *IEEE International Conference on Robotics and Automation (ICRA)*, pages 1479–1484, 2009.

[97] Ningbo Yu, Christoph Hollnagel, Armin Blickenstorfer, Spyros S Kollias, and Robert Riener. Comparison of MRI-Compatible Mechatronic Systems With Hydrodynamic and Pneumatic Actuation. *IEEE/ASME Transactions on Mechatronics*, 13(3):268–277, 2008.

[98] Roger Gassert, Roland Moser, Etienne Burdet, and Hannes Bleuler. MRI/fMRI-compatible robotic system with force feedback for interaction with human motion. *IEEE/ASME Transactions on Mechatronics*, 11(2):216–224, 2006.

[99] Weijian Shang, Hao Su, Gang Li, and Gregory S. Fischer. Teleoperation system with hybrid pneumatic-piezoelectric actuation for MRI-guided needle insertion with haptic feedback. In *IEEE International Conference on Intelligent Robots and Systems (IROS)*, pages 4092–4098, 2013.

[100] Bogdan Vigaru, James Sulzer, and Roger Gassert. Design and Evaluation of a Cable-Driven fMRI-Compatible Haptic Interface to Investigate Precision Grip Control. *IEEE Transactions on Haptics*, 9(1):20–32, 2016.

[101] Roger Gassert, Akio Yamamoto, Dominique Chapuis, Ludovic Dovat, Hannes Bleuler, and Etienne Burdet. Actuation methods for applications in MR environments. *Concepts in Magnetic Resonance Part B: Magnetic Resonance Engineering*, 29B(4):191–209, 2006.

[102] Nikolaos V. Tsekos, Azadeh Khanicheh, Eftychios Christoforou, and Constantinos Mavroidis. Magnetic resonance-compatible robotic and mechatronics systems for image-guided interventions and rehabilitation: a review study. *Annual Review of Biomedical Engineering*, 9(1):351–387, 2007.

[103] P. Chakraborti, H. A Karahan Toprakci, P. Yang, N. Di Spigna, P. Franzon, and T. Ghosh. A compact dielectric elastomer tubular actuator for refreshable Braille displays. *Sensors and Actuators, A: Physical*, 179:151–157, 2012.

[104] Andrea Mazzone, Rui Zhang, and Andreas Kunz. Novel actuators for haptic displays based on electroactive polymers. In *Proceedings of the ACM Symposium on Virtual Reality Software and Technology*, pages 196–204, 2003.

[105] John Vogan, Andreas Wingert, Steven Dubowsky, and Moustapha Hafez. Manipulation in M wises using Electrostrictive Polymer Actuators : ith an Application to Reconfig aging CO. In *IEEE International Conference on Robotics and Automation (ICRA)*, pages 2498–2504, 2004.

[106] J.-S. Plante, K. Tadakuma, L.M. DeVita, D.F. Kacher, J.R. Roebuck, S.P. DiMaio, F.A. Jolesz, and S. Dubowsky. An MRI-compatible needle manipulator concept based on elastically averaged dielectric elastomer actuators for prostate cancer treatment: an accuracy and MR-compatibility evaluation in phantoms. *Journal of Medical Devices*, 3(3):031005 (10 pp.), 2009.

[107] Federico Carpi, Azadeh Khanicheh, Constantinos Mavroidis, and Danilo De Rossi. Silicone made contractile dielectric elastomer actuators inside 3-Tesla MRI environment. In *IEEE International Conference on Intelligent Robots and Systems (IROS)*, pages 137–142, 2008.

[108] Ron Pelrine, Roy Kornbluh, Jose Joseph, Richard Heydt, Qibing Pei, and Seiki Chiba. High-field deformation of elastomeric dielectrics for actuators. *Materials Science and Engineering C*, 11(2):89–100, 2000.

[109] Atsuo Orita and Mark R Cutkosky. Scalable electroactive polymer for variable stiffness suspensions. *IEEE/ASME Transactions on Mechatronics*, 21(6):2836–2846, 2016.

[110] N Nakazawa, R Ikeura, and H Inooka. Characteristics of human fingertips in the shearing direction. *Biological Cybernetics*, 82(3):207–14, 2000.

[111] H Levitt. Transformed up- down methods in psychoacoustics, 1971.

[112] Christopher J Ploch, Jung Hwa Bae, Wendy Ju, and Mark Cutkosky. Haptic skin stretch on a steering wheel for displaying preview information in autonomous cars. In *IEEE International Conference on Intelligent Robots and Systems (IROS)*, pages 60–65, 2016.

[113] Sebastian Mueller and Laurent Sandrin. Liver stiffness: a novel parameter for the diagnosis of liver disease. *Hepatic Medicine: Evidence and Research*, 2:49, 2010.

[114] Nadine Hauthal, Stefan Debener, Stefan Rach, Pascale Sandmann, and Jeremy D Thorne. Visuo-tactile interactions in the congenitally deaf: a behavioral and event-related potential study. *Frontiers in Integrative Neuroscience*, 8(January):98, 2014.

[115] Matt Heverly, Pierre Dupont, and John Triedman. Trajectory optimization for dynamic needle insertion. In *IEEE International Conference on Robotics and Automation (ICRA)*, pages 1646–1651, 2005.

[116] Roland S Johansson. Skin mechanoreceptors in the human hand: receptive field characteristics. *Sensory Functions of the Skin in Primates*, 27, 1976.

[117] Karlin Bark, Jason W. Wheeler, Sunthar Premakumar, and Mark R. Cutkosky. Comparison of skin stretch and vibrotactile stimulation for feedback of proprioceptive information. *Symposium on Haptics Interfaces for Virtual Environment and Teleoperator Systems*, pages 71–78, 2008.

[118] Zhan Fan Quek, Samuel B Schorr, Ilana Nisky, William R Provancher, and Allison M Okamura. Sensory substitution and augmentation using 3-degree-of-freedom skin deformation feedback. *IEEE Transactions on Haptics*, 8(2):209–221, 2015.

[119] AC Moreira, CR Appoloni, WRD Rocha, LF Oliveira, CP Fernandes, and RT Lopes. Determination of the porosity and pore size distribution of sic ceramic foams by nuclear methodologies. *Advances in Applied Ceramics*, 109(7):416–420, 2010.

[120] Ul, Polyurethane Mechanical Properties. https://plastics.ulprospector.com/generics/45/c/t/polyurethane-pur-properties-processing. Accessed: 2018-03-11.

[121] Marina Czerner, Josefa Fabiana Martucci, Laura Alejandra Fasce, Roxana Alejandra Ruseckaite, and Patricia Maria Frontini. Mechanical and fracture behavior of gelatin gels, 2013.

[122] Daniele Tosi, Massimo Olivero, and Guido Perrone. Low-cost fiber bragg grating vibroacoustic sensor for voice and heartbeat detection. *Applied Optics*, 47(28):5123–5129, 2008.

[123] Camilo AR Díaz, Cátia Leitão, Carlos A Marques, M Fátima Domingues, Nélia Alberto, Maria José Pontes, Anselmo Frizera, Moisés Ribeiro, Paulo SB André, and Paulo FC Antunes. Low-Cost Interrogation Technique for Dynamic Measurements with FBG-Based Devices. *Sensors*, 17(10):2414, 2017.

[124] Long Jin, Weigang Zhang, Hao Zhang, Bo Liu, Jian Zhao, Qinchang Tu, Guiyun Kai, and Xiaoyi Dong. An embedded FBG sensor for simultaneous measurement of stress and temperature. *IEEE Photonics Technology Letters*, 18(1):154–156, 2006.

[125] Heather Culbertson, Juliette Unwin, Benjamin E Goodman, and Katherine J Kuchenbecker. Generating haptic texture models from unconstrained tool-surface interactions. In *IEEE World Haptics Conference (WHC)*, pages 295–300, 2013.